Dipl.-Ing. Charles-Alix Manier

Slip-rolling resistance of novel Zr(C,N) thin film coatings under high Hertzian contact pressures

BAM-Dissertationsreihe • Band 60
Berlin 2010

Die vorliegende Arbeit entstand an der BAM Bundesanstalt für Materialforschung und -prüfung.

Impressum

Slip-rolling resistance
of novel Zr(C,N) thin film coatings
under high Hertzian contact pressures

2010

Herausgeber:
BAM Bundesanstalt für Materialforschung und -prüfung
Unter den Eichen 87
12205 Berlin
Telefon: +49 30 8104-0
Telefax: +49 30 8112029
E-Mail: info@bam.de
Internet: www.bam.de

Layout: BAM-Arbeitsgruppe Z.64

ISSN 1613-4249
ISBN 978-3-9813550-3-1

Slip-rolling resistance of novel Zr(C,N) thin film coatings under high Hertzian contact pressures

vorgelegt von
Diplom-Ingenieur
Charles-Alix Manier
aus Saint-Etienne, Frankreich

von der Fakultät III – Prozesswissenschaften
der Technischen Universität Berlin
zur Erlangung des akademischen Grades

Doktor der Ingenieurwissenschaften
- Dr.-Ing. -

Genehmigte Dissertation

Promotionsausschuss:

Vorsitzende:	Prof. Dr.-Ing. C. Fleck
Gutachter:	Prof. Dr. rer. nat. W. Reimers
Gutachter:	Dr.-Ing. M. Woydt

Tag der wissenschaftlichen Aussprache: 11.02.2010

Berlin 2010
D83

Acknowledgements

The present work was carried out within the framework of my four years activities as a scientific co-worker in the Working Group Tribological Optimization; Failure Analysis; Extreme Exposure in the division Tribology and Wear protection (VI.2) of the BAM Federal Institute for Materials Research and testing in Berlin, Germany and generously funded by the German Research Foundation (DFG WO521/6-1).

First of all, I would like to express my sincere thanks to my supervisor Dr.-Ing. Mathias Woydt, head of the aforementioned working group, who gave me the opportunity to start my professional development, initiated and intensively supported this PhD work as well as accepted to take part in thesis committee. Prof. Dr. rer. nat. Walter Reimers, Chairman of the Institute for Materials Science and Technology of the Technical University of Berlin (TU Berlin), is also gratefully thanked for his interest in the thesis subject, for helpful comments and suggestions as well as for agreeing to participate in the referee of this work.

I would like to thank also Prof. Dr.-Ing. Claudia Fleck, Chairman of the Material Engineering Department (Fachgebiet Werkstofftechnik) of the Technical University Berlin (TU Berlin), for assuming the chairmanship of the thesis committee.

All the staff of the tribology division is also greatly acknowledged for bringing a pleasant working environment. Dr. Dirk Spaltmann is particularly thanked for the helpful discussions as well as for his assistance in English formulation. Dipl.-Ing. Manuel Reichelt and my bureau colleague Dr.-Ing. Géraldine Theiler will find here my many thanks for promoting constantly a good working atmosphere. Sigrid Binkowski and Dipl.-Ing. Norbert Kelling are also gratefully acknowledged for their constant and helpful technical support. André Otto is also thanked for his substantial administrative support.

My sincere thanks go to Dr. rer. nat. (and “by the way” world and olympic champion in eights rowing) Ilona Dörfel (BAM V.1, Composition and Microstructure of Engineering Materials) for performing the highly relevant TEM investigations as also Heidemarie Rooch, and Ing. Wolfgang Gesatzke for the specific preparation of the samples.

Furthermore, I greatly appreciate the contributions of Dr.-Ing. Vasile-Dan Hodoroaba, Birgid Strauß, Sigrid Benemann and Dipl.-Phys. Thomas Wirth (BAM VI.4) for their valuable contributions in microscopy analysis and to Dr.-Ing. Eric Wild (TU Berlin) for the substantial residual stress analysis of the coatings. Acknowledgement is also due to Dr. Thomas Chudoba from ASMEC GmbH for performing hardness measurements with his QCSM module. Thanks are surely extended to Fundación Tekniker, specifically Josu Goikoetxea and Dr. Javier Barriga for the manufacturing of the coatings in industrial deposition chambers and to the machining shop BAM Z.5 for the specimens preparation.

Last, but by no means the least, I would like to thank all my friends for their support and to all the people who helped me directly or indirectly in my doctoral work and/or for my pleasant German adaptation. My very special thanks (du fond du coeur) go to my beloved parents Marie-Hélène (What is Tribology?) and Gérard (I miss you so much) and “of course” to my bright (and sometimes nerve-racking) sister Sophie, for everlasting encouragement and plenty of good advices in a wide range of domains. Ania, especially for your contribution in the decision of pursuing my “German experiment”.

Zusammenfassung

Heutzutage sind Beschichtungen in breiten technologischen Anwendungsfeldern von Dekorierungszwecken bis zur Verbesserung der Leistung von Werkzeugen in der Massenfertigung, von medizinischen Werkzeugen oder noch von Computer Bestandteilen und vielen Anderen verbreitet. Besonders rechnet die Automobilindustrie mit einem Leistungsgewinn bei der Verwendung von Dünnschichten in mechanischen Bauteilen des Antriebstranges und des Getriebes. Das auf einer kostengünstigen Alternative basierte Konzept ist die Leistungssteigerung durch Erhöhung der Tragfähigkeit durch Aufbringung von Dünnschichten, die zu zusätzlichen Eigenschaften beitragen könnten, ohne das Design der Bauteile grundlegend zu verändern. Es würde auch einen Weg in Richtung Downsizing darstellen.

In der vorliegenden Arbeit ist eine kurz gefasste Literaturübersicht bezüglich der Wälzbeständigkeit von verschiedenen Dünnschichten zusammengestellt. Bei der Durchführung von Wälzversuchen sind kristalline Zr(C,N) Dünnschichten als wälzbeständig nachgewiesen worden und zwar bis zu einer mittleren Hertzschen Kontaktpressung von $P_{0mitteln}$ = 1,94 GPa (P_{0max} = 2,91 GPa) bei 120°C in Erstbefüllungsmotoröl bis zu zehn Millionen Zyklen. Grundsätzlich stellt dieses Ergebnis hier eine Verdoppelung der auf die Oberfläche wirkenden Normalkraft gegenüber unbeschichteter Kontaktkonfiguration dar, die herkömmlich mit gebrauchsfertig formulierten Ölen (d.h. mit hohem Anteil an Additiven) geschmiert sind. Typischerweise bestehen die zu beschichtenden Substrate aus vergütetem Lagerstahl Cronidur 30. Die Zr(C,N) Dünnschichten sind mittels verschiedenen Untersuchungsmethoden charakterisiert worden, um die Ursachen festgestellter Ergebnisunterschiede bezüglich der Wälzbeständigkeit unter diesen hohen tribologischen Beanspruchungen zu klären.

Die Wälzbeständigkeit verschiedener Beschichtungschargen ist mittels eines festgelegten, leistungsfähigen Prüfverfahrens evaluiert worden. Verschiedene Standzeitergebnisse sind zwischen den einzelnen Chargen erreicht worden, ohne wesentliche Änderungen bei den Abscheidungsprozessen vorzunehmen. Die durchgeführte Charakterisierung stellt mikrostrukturelle Unterschiede fest, die die Wälzbeständigkeit beeinflussen und als Ursache der Wälzverhaltensunterschiede der Zr(C,N) Dünnschichten sein können. Außerdem ist die Leistung der Zr(C,N) Dünnschicht nicht nur im Bezug auf die Steigerung der Wälzbeständigkeit sondern auch hinsichtlich des tribologischen Einflusses (u. a. Nachwirkungen auf den Verschleiß und die Reibung) bewertet worden. Darum wurden die tribologischen Ergebnisse mit den entsprechenden gemessenen Größen von unlängst entwickelten DLC-Dünnschichten (DLC, Diamond Like Carbon) verglichen, die auch bei der gleichen Prüfprozedur getestet worden sind und gleiche Überrollungszahlen erwiesen hatten.

Abstract

Today, coatings are used in many applications ranging from the decoration purposes to the improvement of efficiency such as in machining tools, medical tools, computer devices (hard disks) and many more. Especially the automotive industry anticipates a benefit in using coatings for example in powertrains and gears where the mechanical components are stressed under slip-rolling motion. A cost effective option to increase efficiency is based on the increase of the load carrying capacity by thin film coatings. It would also represent a way towards downsizing.

In the work presented here, a small review concerning rolling contact fatigue of coatings was performed. Experimentally it is then shown, that crystalline Zr(C,N) coatings can be slip-rolling resistant at 120 °C in factory fill engine oil up to ten million cycles under average Hertzian contact pressures up to $P_{0mean} = 1.94$ GPa ($P_{0max} = 2.91$ GPa). Basically, it represents here the doubling of the normal force acting on the surface compared to uncoated steel traditionally lubricated with fully formulated oil. Typically, the coated substrates are made of the quenched and tempered bearing steel Cronidur 30. The Zr(C,N) coatings were fully characterized using different characterisation techniques in order to understand the difference in slip-rolling resistance under those high tribological demands.

Effectively, the slip-rolling resistance of different batches of the Zr(C,N) coatings is evaluated using a defined and powerful testing procedure. Different results of lifetime were achieved without fundamental changes of the deposition procedure. The characterisation achieved permits the identification of microstructural disparities which should affect the load carrying capacity of the coating. Moreover, the efficiency of the high slip-rolling resistant Zr(C,N) coating was considered not only with respect to the improvement of the load carrying capacity of the substrate but also in terms of tribological performances in respect of wear and friction induced. Tribological results are also compared with those of newly developed DLC coatings (Diamond-Like Carbon) principally known for their “chameleon” tribological properties enabling the singular combination of low friction and low wear, i.e. those having shown the best performances until now under the same slip-rolling testing procedure.

Table of contents

Nomenclature

Symbols

α	[GPa]	Pressure-viscosity coefficient
γ	[-]	Parameter describing the surface pattern of the roughness
η	[-]	Corrective factor of asymmetry for calculation of Hertzian contact pressures
η_0	[Pa.s]	Oil dynamic viscosity at operating temperature
λ	[-]	Tallian parameter, lubricant film thickness to roughness ratio,
$\lambda_{0.5x}$	[m]	Correlation length in the x direction
$\lambda_{0.5y}$	[m]	Correlation length in the y direction
μ	[-]	Friction coefficient (equivalent to COF)
ν	[-]	Poisson’s ratio
ξ	[-]	Corrective factor of asymmetry for calculation of Hertzian contact pressures
σ_{vmax}	[MPa]	maximum Von Mises stress
ω	[-]	Rotation speed

a	[m]	Semi major axis
a^*	[-]	Position between red/magenta and green in CIE 1976 L*, a*, b* colour space
b	[m]	Semi minor axis
b^*	[-]	Position between yellow and blue in CIE 1976 L*, a*, b* colour space
B10 life	[-]	Life at 10% failure probability
B50 life	[-]	Life at 50% failure probability
COF	[-]	Coefficient of friction (equivalent to μ)
C_r	[-]	Surface roughness correction factor
d	[nm]	Interplanar spacing
E	[GPa]	Modulus of elasticity
E'	[GPa]	Effective modulus of elasticity
F_N	[N]	Normal load
F_R	[N]	Friction force
G	[-]	Material parameter
H_{min}	[-]	Adimensional EHD minimal film thickness
h_{min}	[m]	Minimal lubricant film thicknesses
H_{plast}	[MPa]	Plastic hardness
k	[-]	Elliptical form parameter
k_{BP}	[m]	Curvature
K_{iso}	[-]	Parameter of isotropy, defined as the ratio between the transverse and the circumferential residual stresses
L	[m]	Distance run under sliding
L^*	[-]	Lightness in CIE 1976 L*, a*, b* colour space
L10 life	[-]	Life at 10% failure probability (equivalent to B10)
L_{C1}	[N]	Critical load in scratch test
p	[Pa]	Pressure applied on lubricant
p_0	[Pa]	Reference pressure
P_{0max}	[GPa]	Initial average Hertzian contact pressure
P_{0mean}	[GPa]	Initial maximum Hertzian contact pressure
P_{max}	[GPa]	Maximum Hertzian contact pressure
R_a	[µm]	Arithmetical mean roughness
$R_{p0,2}$	[MPa]	Yield strength at 0.2% plastic strain
R_{pK}	[µm]	Reduced peak height
R_q	[µm]	RMS roughness
R_x	[-]	Reduced curvature radius in x direction
R_z	[µm]	Average maximum height
s	[%]	Slip-to-roll ratio
U	[-]	Speed parameter
v	[m/s]	Surface velocity
V	[µm³]	Volume
W	[-]	Load Parameter

W_e	[nJ]	Elastic work
Wq	[µm²]	Average worn surface in cross section
W_r	[nJ]	Plastic work
W_{total}	[nJ]	Total work

Abbreviations

a-C	Hydrogen free amorphous carbon
a-C:H:X	Doped amorphous carbon containing hydrogen
pcnl	Process-controlled nanolayering
ta-C	Tetrahedral hydrogen free amorphous carbon
ta-C:H	Tetrahedral amorphous carbon containing hydrogen

AES	Auger electron spectroscopy
AFM	Atomic Force Microscopy
AISI	American Iron and Steel Institute
AMS	Aerospace Material Standards
APS	Air plasma spray
ATF	Automatic Transmission Fluid
AW	Anti wear
BAM	Bundesanstalt für Materialforschung und -prüfung (Institute for Materials Research and Testing)
CADP	Cathodic arc plasma deposition
CIE	Commission Internationale de l'éclairage
CVA	Cathodic Vacuum Arc deposition
CVD	Chemical vapour deposition
CVM	Consumable-electrode vacuum arc melting
DESU	Druck-Elektro-Schlacke-Umschmelzverfahren (=PESR)
D-Gun	Detonation gun
DIN	Deutsches Institut für Normung
DLC	Diamond-Like Carbon
EDX	Energy Dispersive X-ray spectroscopy
EFTEM	Energy-filtered transmission electron microscopy
EHL	Elastohydrodynamic
EP	Extreme pressure
FCC	Face centered cubic
FCVA	Filtered Cathodic Vacuum Arc
FEG	Field emission gun
FF	Factory fill
FIB	Focused Ion Beam
FWHM	Full width at half maximum
FZG	Forschungsstelle fur Zahnrader und Getriebebau (Institute for Machine Elements Gear research Center)
GD	Glow Discharge
GIXRD	Grazing Incidence XRD
HAADF	High Angle Annular Dark Field
HC	Hydrocarbons
HRC	Hardness Rockwell C
HREM	High Resolution Electron Microscopy
HTHS	High-Temperature High-Shear
HV	Hardness Vickers
HVOF	High Velocity Oxygen Fuel (Thermal Spray Process)
ISO	International Organization for Standardization
JCPDS	Joint Committee on Powder Diffraction Standards / (now, International Centre for Diffraction Data)
JIS	Japanese Industrial Standards
MOCVD	Metal-organic chemical vapour deposition

MW-ECR	Microwave electron cyclotron resonance
NASA	National Aeronautics and Space Administration
NBD	Nano-Beam Diffraction
NOACK	ASTM D-5800 volatility test
OCABS	Overbased calcium alkyl benzene sulfonate
OEM	Original equipment manufacturer
PACVD	Plasma Activated Chemical vapour deposition
PCB	Printed circuit board
PCW	Percentage of coating worn
PESR	Pressurized electroslag remelting
PEG	Polyethylene glycol
PF	Powder forged
PVD	Physical vapour deposition
QBSD	Quadrant Back Scattering Detector
QCSM	Quasi Continuous Stiffness Measurement
RCF	Rolling Contact Fatigue
RT	Room temperature
RWTH	Rheinisch-Westfaelische Technische Hochschule
SAD	Selected Area Electron Diffaction
SAE	Society of Automotive Engineers
SAP	Sulphur, Ash and Phosphate
SEM	Scanning Electron Microscopy
SFS	Suomen Standardisoimisliitto SFS ry (Finnish standards association)
TAN	Total Acid Number
TBN	Total Basic Number
TEM	Transmission electron microscopy
VAR	Vacuum Arc Remelting
VG	Viscosity Grade
VIM	Vacuum induction melting
WDX	Wavelength Dispersive X-ray Spectrometry
XEC	X-ray elastic constants
XRD	X-ray diffraction
ZDDP	Zinc dialkyldithiophosphates

1 Introduction and aim of this work

Reduction in system costs is one of the major objectives in mechanical applications accompanied parallel increase of power output. Other drivers worldwide are new environmental standards and laws related to “carbon-taxes”. Carbon taxes mainly stimulate light-weight design and reduction in friction. This leads in turn to the question, if material based concepts can substitute harmful EP/AW-additives in lubricants and improve the performance of nowadays applications.

Effectively most of today’s oil formulations are based on hydrocarbons (HC). The functionality of these hydrocarbons is improved by highly developed additives in perfectly balanced additive packages. The actual and future requirements for wear resistance and extreme pressure-behaviour (EP) in highly loaded applications subjected to rolling and slip-rolling call for new lubrication concepts or metallurgies, especially when they have to fulfil bio-no-tox requirements. On one side additives provide to hydrocarbons their full functionality but on the other side are mostly responsible for their higher eco-toxicity. In a certain way, they govern the ecological impact of hydrocarbon based formulations. Moreover, they define the loading of the particulate filters with oil ash.

For these reasons, substitution of toxic additives by other concepts represents an interesting and future-proof alternative. Two ways are possible. The first one is the replacement of HC based lubricants by other base oils type with better intrinsic properties (for instance esters, polyglycols), thus substituting the whole additives package. Instead of substituting or ameliorating the lubricants, another way is to work on the contacting/mating materials. During the last decades, the quality of steel increased due to more refined production facilities and great technological improvements in processing, for example with the development of electric arc furnaces, degassing systems, Vacuum Induction Melting (VIM) and Vacuum Arc Remelting (VAR) methods, leading to almost “clean” steels. Surely, parallel to the lubrication evolution, it has improved the lifetime (L_{10} – life) and safety factors of steel based products like ball/roller bearings or gears. However one outcome was the shift of volume problems with defects in the material bulk to the surface. Nowadays damages are mostly initiated near and by the surface itself. Defects on surfaces are prejudicial for the well functioning of systems [VIL98]. Therefore the solution of better bulk purity is still insufficient to achieve the step to more efficiency, i.e. power output increase through improvement in load carrying capacity.

It is widely believed, that coatings can increase the functional performances of tribosystems. Development of hard thin film coatings was undertaken mainly to improve the wear resistance and enhance efficiency of machine components such as tools working under normal and extreme operating conditions. It is proved they offer:

a. an increase of the energy efficiency, i.e. friction reduction,

b. an increase in load carrying ability or

c. an extension of the components lifetime

or even better, a combination of these three main demands, which contribute to a better control of the operation and maintenance costs. For example, since many years WC-Co based tools for drilling, cutting or milling operations have been successfully coated to diminish wear of cutting edges or lubricant use and to enhance quality of the additional machined surfaces, extending lifetimes and replacement intervals, thus making production more efficient. This efficiency increase can be mainly extended towards applications working under sliding motion.

However coating of rolling/slip-rolling parts subjected to cyclic fatigue and furthermore under deficient lubricant is rarely reported and remains nowadays an attractive challenge. A potential exists if coatings provide higher performance as conventional uncoated rolling bearings and gears, which are the most commonly used mechanical parts. A contribution towards downsizing and higher load carrying capacity could then be achieved, opening up interesting possible technical impacts for fuel economy and higher efficiency through reduction of proliferations of mechanical designs.

Effectively, coatings will present a functional benefit for concentrated, lubricated tribosystems, if they succeed in increasing the load carrying ability of steels under slip-rolling much above load stage 12 of the FZG tests [SEI72], preferentially up to the stage 13 or 14. This load stage represents today the most demanding test procedure for lubricated gears as described in the international standard ISO 14635-1. The FZG 12 stage corresponds to a maximal Hertzian stress P_{max} of 1,861 MPa and FZG 14 to 2,140 MPa.

Therefore an effective thin film coating should combine different base functions. Firstly an increase of the acceptable Hertzian stress up to P_{max} = 3,000 MPa should be achievable. Secondly this coating should remain slip-rolling resistant at oil temperature above 120°C, representing a typical operating temperature of engines. Also required are lower coating wear rates and a decrease in the friction in comparison to steel/steel couples lubricated with state-of-the-art lubricants, and all of this preferentially in a lubricant with a low additive content.

This work presents the slip-rolling resistance (with a definite slip rate of 10%) of a novel crystalline Zr(C,N) thin film coating on a stainless, nitrogen alloyed steel substrate (AMS 5898) with high annealing temperature. Steel was chosen as substrate because it remains the main construction material used for lubricated applications and for machine concepts subjected to pure rolling motion, such as bearings, or with a certain slip amount, like gears and cams. For instance, in 2004 the world production of crude steel amounted to 1,069 Mt (and in 2007 it was 1,344 Mt) (World Steel Association). At the beginning of the 2000s, each day 300 t of steel were dedicated to bearing manufacturing, in France alone. This represents per year 90,000 t, absorbing 0.01% of the annual world production of steel.

The Zr(C,N) coatings were synthesised by arc-PVD technology and then tribologically tested. The slip-rolling resistance was evaluated under very high initial average Hertzian contact pressures ranging between P_{0mean} = 1.5 GPa and 2 GPa. The tests were carried out under the most severe lubrication regime, aside from “dry lubrication”, the so-called mixed/boundary lubrication. Two lubricants, unadditivated paraffinic oil (pure hydrocarbon) and factory fill SAE 0W-30 engine oil (High-Temperature High-Shear, HTHS = 3.0 mPa.s) were used. The best coating presented here could achieve 10 million cycles without any damage under an initial maximal Hertzian contact pressure P_{0max} well over 2.75 GPa. For comparison, this exceeds largely the well-known and standardized stage FZG 12 for gear applications based on uncoated steel construction lubricated with fully additivated oils, that means containing high amounts of harmful EP/AW (Extreme Pressure / Antiwear) additives, based for example on sulphur, ash and phosphate (SAP). Microstuctural characterisations were carried out on the slip-rolling resistant coating and compared with worser coatings to evaluate the critical characteristics ensuring the slip-rolling resistance. Moreover, the tribological performances were compared with the best DLC (Diamond-Like Carbon) coatings developed by OEMs (Original Equipment Manufacturer) in the frame of a benchmark.

2 State of the art

2.1 Relevance of slip in technical systems subjected to rolling

For roller and ball bearings as well as for gear mechanisms, the rolling contact combined with slip represents the essential loading mode for the fulfilment of the constitutive function of the assembly. These both fields of application – bearing and gearing – differ slightly in their slip ratio encountered during operating. In bearings (ball or roller), microslip takes place due to the geometry of the contact (Reynolds and Heathcote microslip). Whereas for bearing the slide-to-roll ratio does not exceed 3%, it can reach values from 20% to 30% in gears at the contact point depending on the construction design (number of teeth, diameters…). Moreover the value varies along the pitch line (see *Fig. 2.1*).

Table 2.1: Occurrence and relevance of sliding during rolling motion in different, widespread construction elements.

Mechanical systems	**Base body**	**Counterpart**	**Lubricant**	**Environ-ment**	**System mode**	**Slip ratio**
Gearing	Driving gear	Pinion gear	Gearbox oil (transmission oil), ATF	Air	Closed	20-30%
Rolling-element Bearing	Ring raceway, flange	Ball, cylinder, taper	No / grease / oil	Air	Closed	< 3%
Cam	Camshaft (cam lobe)	Tappet, cam follower, lifter	Motor oil	Air	Closed	0-13%
Railway	Wheel	Track	No / grease	Air	Open	Depends

In order to understand the rolling motion occurring in gears, the dimensionless distribution of normal force (F_N/F_{Nmax}), Hertzian maximum line pressure (P/P_{max}), surface velocities (V/V_{max}) and combined radius of curvature (ρ/ρ_{max}) along the line of action for a gear pair type SFS 3390 (Finland) are pointed out. The teeth engagement starts at the left of *Figure 2.1* and the two sharp changes in load and pressure take place as the two tooth engagement changes to the single tooth engagement and reverse. The Hertzian pressure reaches its highest value in the slip range from -30% to +30%. Pure rolling takes place only briefly at the pitch point.

Cylindrical spur gears and helical gears are the most commonly used gear wheels. The differences in performance are mainly higher power throughput with the helical gear, due to a higher contact ratio. The drawbacks of using helical gear wheels are slightly higher losses and a demand for more advanced manufacturing equipment. Therefore an increase in power transmission above the actual limitations could be obtained only by achieving higher torques, i.e. Hertzian contact pressures.

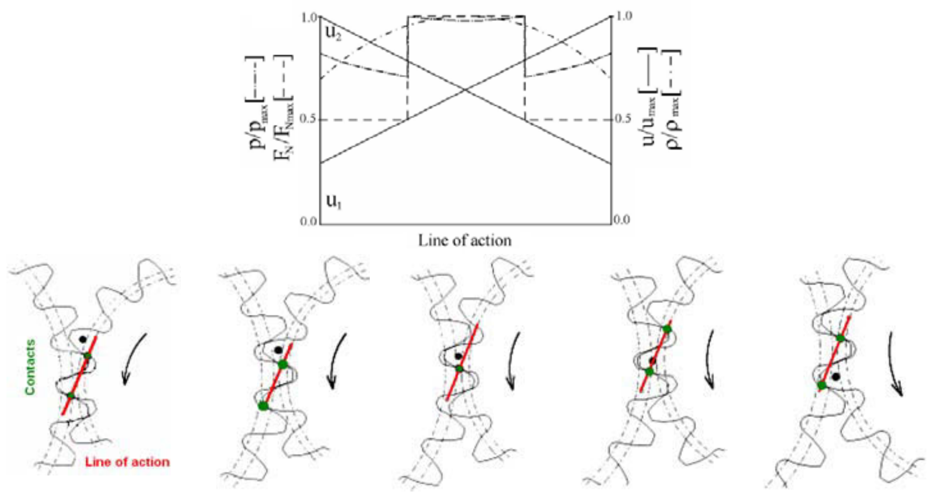

Figure 2.1: Kinematics of the point contact in gears [KLE08]

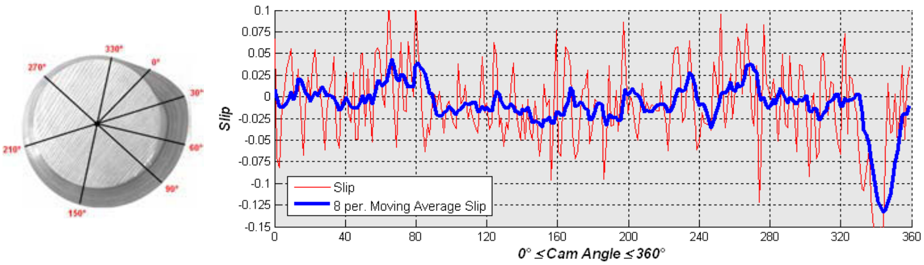

Figure 2.2.: Slip evolution between roller and camshaft in function of the outline of the camshaft for an engine speed of 1800 rpm (i.e. 900 rpm for the camshaft) under maximal injection force [MAL06], (the maximal Hertzian pressure can temporarily reach values in the range of 1,800 MPa).

2.2 Development of surface damages of uncoated steel

Figure 2.3 is a good example for the tribological problematic of uncoated steel components brought in contact and subjected to high Hertzian stresses and rolling motion. The arrow symbolizes the improvement of the load carrying capacity through surface changes equivalent to a smaller slope and/or a y-shift of the dotted lines. The results of the lifetime in function of the maximal Hertzian contact pressure reported in this diagram were achieved on a twin disc apparatus. Tests were conducted in a similar way as in the present work (see *Fig. 3.6* and *Tab. 3.5*), however at higher rotational speeds, without slip, with a more viscous oil at a lower temperature and with a softer failure criterion, i.e. the formation of macropitting. In addition it induces milder tribological conditions as lubrication takes place in the domain of the mixed/hydrodynamic with λ (see 2.6 for definition) values ranging from 1.6 to 6, which depend on the roughness of the contacting surfaces. Effectively, samples with polished surfaces last longer than those having higher roughness values under the same working conditions [WIN09]. It is then evident that the surface “dictates” the lifetime (or load carrying capacity) of the assembly and not the bulk of the material.

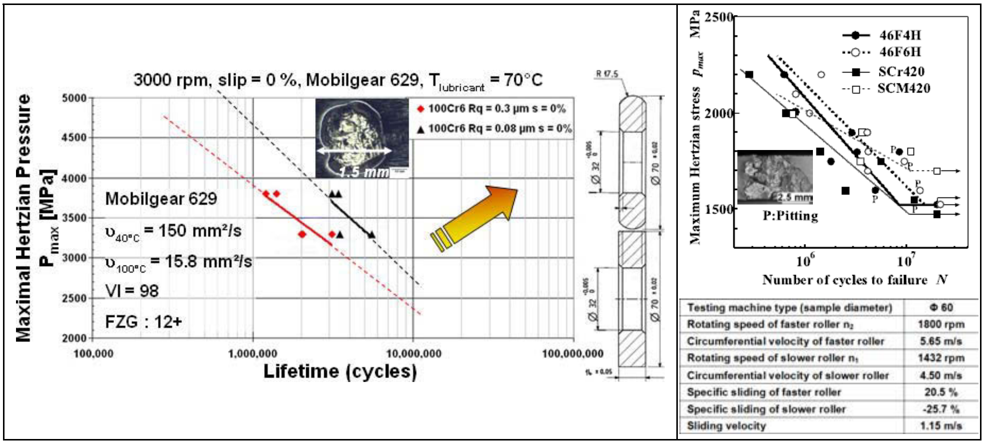

Testing machine type (sample diameter)	Φ 60
Rotating speed of faster roller n_2	1800 rpm
Circumferential velocity of faster roller	5.65 m/s
Rotating speed of slower roller n_1	1432 rpm
Circumferential velocity of slower roller	4.50 m/s
Specific sliding of faster roller	20.5 %
Specific sliding of slower roller	-25.7 %
Sliding velocity	1.15 m/s

Figure 2.3: Rolling contact fatigue results and contact configuration for uncoated 100Cr6 steel (hardness 760 HV) and for PF 46F, JIS SCr420 and JIS SCM420 (experimental results from [THO04] and [ZHA04]).

Indeed polishing represents a technical response for the improvement of the load carrying capacity, but it is a disadvantageous and “bounded” solution: the polishing takes time, is not easy for complicated geometries, technologically limited by the quality that can be reached and polishing is the ultimate step of surface refinement, the roughness cannot be further reduced.

In a similar way, powder forged steels (PF 46F-X) and chromium (JIS SCr420) and chromium molybdenum (JIS SCM420) steels, both being traditionally used for case-hardened gears of automobiles in Japan (surface 800 HV, R_a ~ 0.25 µm), do not withstand very high Hertzian pressures even if lubricated with EP gear oils (results from [ZHA04]).

Though, thin coatings constitute a possible solution, in the way that the surface is totally changed through the build-up of a new one with other properties. Coatings could decrease the sensibility of the surface towards damage initiation and propagation, involving an increase of the slip-rolling resistance.

Surface-initiated and subsurface-initiated damaging is mostly responsible for rolling contact fatigue. A competition between these both initiation types takes constantly place during the fatigue phenomenon. A lot of parameters play a role, such as residual stresses distribution, residual stresses induced during working operations, lubrication regime (speed, oil viscosity, temperature), friction intensity, pollution of oil (wear debris, oil oxidation and aging, environmental particles), roughness of the contacting surfaces, surface defects, subsurface inclusions or heterogeneity, orientation and localisation of pre-cracks contained in the material, wear of the surface… For example *Figure 2.4* depicts the influence of the roughness and loading on the competition between volume and surface initiated cracks. However with today’s technological progress in material elaboration, it appears that the surface initiation damaging becomes the predominant origin of rolling contact fatigue [NEL98]. Pitting and micro-pitting are both phenomena occurring at the surface of the rolling elements leading in the long run to damaging of rolling systems (vibrations and favouring crack propagation).

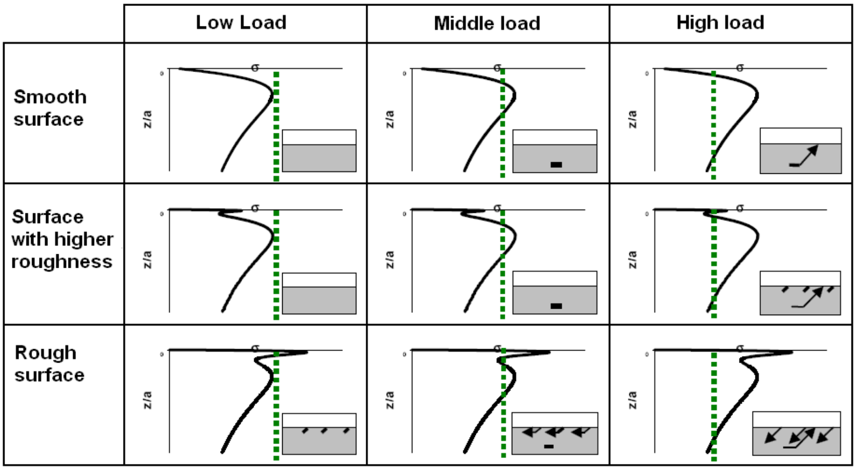

Figure 2.4: Hypotheses of damaging developments with competition between surface and bulk-initiated cracks (dot line represents the load limit of the material) [NEL99]

Oila and Bull [OIL05] tried to assess experimentally the factors influencing micropitting in rolling/sliding contacts by using a twin disc tribometer and a fractional factorial design $2^{(7-4)}$ plan, i.e. seven parameters, each having two values. The following parameters were taken in account: steel grade, roughness, load, lubricant type, temperature, speed, slide-to-roll ratio. They conclude, in their study and with the parameters used (SAE 8620 and EN36 steels), that the interactions can be high between parameters.

The most important factor in micro pitting initiation is the load, since the highest load value (P_{max} = 2.2 GPa) seems to be independent from all the factors considered (except for roughness and steel grade). At high contact pressures the means to avoid micropitting are then limited and, under the experimental conditions used in their study, the proposed way to retard micropitting initiation is the improvement of surface finishing. Effectively superfinishing of gears permits higher lifetime [WIN09]. Sliding appears to be meaningful only at low rotation speeds.

About micropitting progression, motion speed is the relevant factor. High speed coupled with high slide-to-roll ratio aggravates pitting. Furthermore they observed that micropitting develops faster, if martensite decay (appearing of Dark Etching Region and White Etching Bands) is more pronounced. The choice of the ground material and related properties are of prime order. Growth of micropits depends on the frictional power dissipation by sliding of surface asperities, which result in plastic deformation and heating of the surfaces. The increased temperature also reduces the lubricant viscosity and load carrying capacity, which also contributes to poor micropitting performance.

Therefore, adding a coating on the surface should ameliorate the performance of high loaded elements by enhancing load carrying capacity at low speed which would reduce the trend of micropitting initiation, and if possible avoiding martensite decay by acting as thermal barrier.

Ahlroos et al. used an Amsler twin disc machine (sample configuration: barrel on cylinder) to evaluate the micropitting sensibility of case hardening steel 20MnCr5 subjected previously to different surface treatments (carburizing, 0.5 µm ta-C coating, carbonitriding) with smooth (R_a = 0.04 µm) and rough surfaces (R_a = 0.4 - 0.7 µm) in three lubricants at 65°C (mineral oil, ester oil, and tall oil based ester) [AHL08]. The tests however were performed at (very) high speeds (4.05 m/s and 3.13 m/s, slide-to-roll ratio 30%) with stepwise Hertzian pressures increasing from 1.0 GPa to 2.0 GPa. They reported that roughness was found as the major affecting factor in micropitting development under high speed. The coated configuration succeeded very well in all cases, showing no micropitting after test i.e. 7 testing days or 17 millions cycles. Moreover they suggested that the lower friction encountered with the ester oil reduced the micropitting sensitivity, since the surface is less submitted to shear stresses.

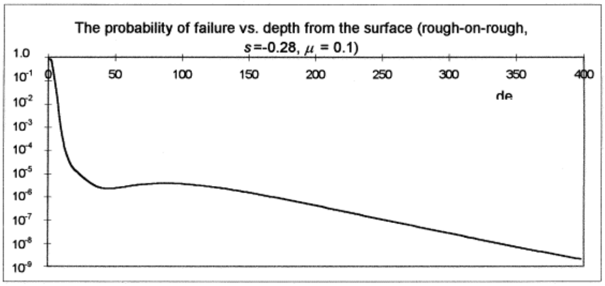

Figure 2.5: Fatigue risk (or probability of failure) vs. depth after 100 million cycles [KIM98]

Anyway in the long run, the surface is the most critical location for dramatic fatigue rupture. *Figure 2.5* illustrates clearly this fact. It depicts the prediction of the probability of failure with depth from the surface of a rough-on-rough case (ground finished of 0.18 µm rms) at a maximum Hertzian pressure of 0.83 GPa and a slide roll ratio of 28% (E = 207 GPa, ν = 0.3).

2.3 Definition of the slip-rolling motion

A tribological system under rolling motion and simultaneously solicited with sliding can be denominated as slip-rolling motioned. Sliding occurs when the speeds of the two contacting bodies differ, i.e. the speed vectors at the contacting point are not equal (direction, value). Two different equations exist to express the slip-to-roll ratio:

$$s = \frac{\overrightarrow{v_1} - \overrightarrow{v_2}}{\overrightarrow{v_1}} \cdot 100\% \tag{2.1}$$

$$s = 2 \cdot \frac{\overrightarrow{v_1} - \overrightarrow{v_2}}{\overrightarrow{v_1} + \overrightarrow{v_2}} \cdot 100\% \tag{2.2}$$

where v_i are the speeds of the contacting bodies. The first expression (Eq. 2.1) is the widely used and facilitates the understanding of the movement. The main specimen, the one of interest, is noted one, and the sign of its speed is always positive. The counter body (or counterpart) is indexed as two, and the sign of its speed is also positive to fulfil the basics of rolling. If this sign is positive then the counter body rolls in the opposite direction as the main body. And the speed vectors point in the same direction at the contacting point. The condition of rolling motion is satisfied. The slip amount or slide-to-roll ratio then depends on the value of the speed of the counter body. Explicitly, for a higher speed of the counterbody ($v_2>v_1$), the slip ratio will be negative and in the case of a lower speed ($v_2<v_1$), it will be positive. With a positive slip ratio, the resulting friction force F_R acts on the main specimen opposite to the rolling direction (*Fig. 2.6*).

For a negative sign of the counterbody, it has the same motion of the main body and the resulting speed vector has an opposite direction at the contact point. However in this case, the slip is so high that it does not meet the fundamentals of rolling.

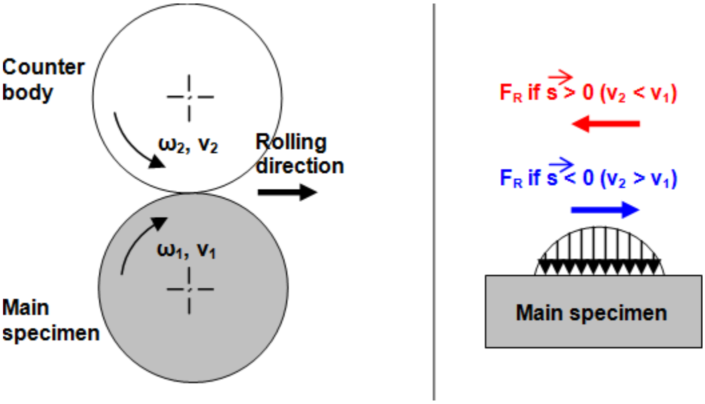

Figure 2.6: Slip-rolling motion

2.4 Rolling friction

In principle, any rolling device suffers under rolling friction mainly due to deformations and to a smaller extend, to micro-slip at the interface if the rolling bodies have dissimilar elastic constants [JOH87]. This “mechanical” friction is characterized by the formation of a bead in front of the contact and opposite to the direction of motion. The bead is formed due to deformation of the contacting surfaces as shown in the *Figure 2.7.* It can be regarded as if the rolling bodies would climb an infinite slope and the resulting reaction force is not directly aligned with the normal load, since it is distributed over the actual contact area rather than a point contact aligned with the rotation centre. Therefore the distribution of the reaction force on this asymmetric surface involves an asymmetry of the pressure distribution, which is higher on the front half of the contact than at the rear [JOH87] engendering an opposite torque.

Therefore the rolling friction depends not only on the contacting materials but also on the contacting geometry. Speed, slip, presence of lubrication and surface adhesion affect rolling friction too. For the bead formation, the rolling parts are deformed elastically or plastically. In the first case, the materials recover their original geometry and in the second one a sort of wheel track is left.

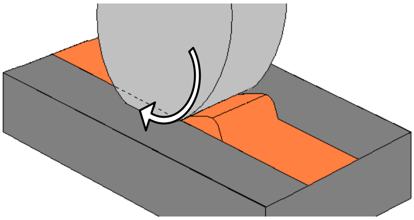

Figure 2.7: Scheme for understanding slip- rolling friction.

Protecting the contacting surfaces with a coating harder than the substrate could then restrain the formation of the bead and in turn reduce the rolling friction compared to an uncoated configuration. Moreover, a harder surface limiting the deformation could improve the lifetime, i.e. rolling resistance, of the tribosystem. The replacement of the steel surface by another surfacing material, having a lower susceptibility towards fatigue, represents a technical challenge. A hard coating material does not represent the only way. A soft surface material could better “adapt” to the load and reduce the corresponding Hertzian contact pressure by engendering a bigger contact surface. But the friction could be larger. A plastic flow on the sides of the contact could be advantageous, reducing the bead formation and the contact stress.

2.5 Hertzian contacts

Principally, rolling contacts have to enable the transfer of loads between two different bodies which are put together in relative motion. Therefore, one or both of the parts are curved to optimize their mutual movement. This geometrical constraint then involves smaller contact surfaces as plane-to-plane geometry. The load is not distributed on a wide plane but concentrated mostly on a local surface, which can be circular or elliptic depending on the construction and on the contact geometry. Consequently, for the contacting surface being smaller, an increase in the stresses is unavoidable. Under static consideration, i.e. without motion, these stresses are commonly known as Hertzian contact pressures (or stresses). Hertz was the first to describe [HER81] and resolve analytically the contact between two elastic bodies with curved geometry. It still remains nowadays the only problem resolved analytically. The length of the semi major axis *a* and semi minor axis *b* forming the elliptical contact surface are determined by the following equations:

$$a = \xi \cdot \sqrt[3]{\frac{3 \cdot F_N}{\sum k} \frac{(1-\nu^2)}{E}} \tag{2.3}$$

$$b = \eta \cdot \sqrt[3]{\frac{3 \cdot F_N}{\sum k} \frac{(1-\nu^2)}{E}} \tag{2.4}$$

where

$$\frac{(1-\nu^2)}{E} = \frac{1}{2} \cdot \left(\frac{(1-\nu_1^2)}{E_1} + \frac{(1-\nu_2^2)}{E_2} \right) \tag{2.5}$$

with E_1, E_2 the elastic modulus,1 and 2 referring the two contacting bodies

ν_1, ν_2 the Poisson’s ratio, 1 and 2 referring the two contacting bodies

F_N the normal force

The coefficients ξ and η are corrective factors which can be interpreted as factors describing the deviation from the symmetrical ball-on-ball geometry. They are tabulated according to the value of *cos* τ which refers to the contacting curvatures (*Fig. 2.8*). The length of the semi major axis *a* and semi minor axis *b* allow the calculation of the maximum and average Hertzian contact pressures according to the equations:

$$P_{max} = \frac{1}{\xi \cdot \eta} \cdot \sqrt[3]{\frac{3 \cdot F_N \cdot}{8\pi^3 \left(\sum k\right)^2} \frac{\cdot \left(1-\nu^2\right)^2}{E^2}} \qquad (2.6)$$

$$P_{mean} = \frac{2}{3} \cdot P_{max} = \frac{F_N}{\pi \cdot a \cdot b} \qquad (2.7)$$

The maximum shear stress occurs at a point beneath the surface on the z-axis. The depth depends upon the eccentricity of the ellipse as given in *Table 2.2* and *Figure 2.9* [JOH87].

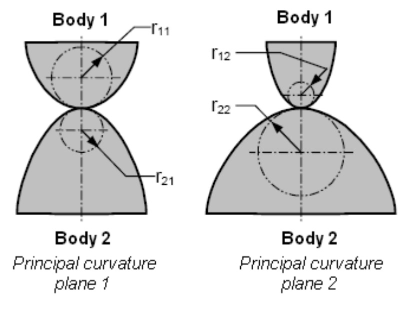

Curvature k_{BP}:

$$k_{BP} = 1/r_{BP}$$

$k_{BP} > 0$ if convex, $k_{BP} < 0$ if concave
(index B: Body ; index P: plane)

$$\sum k_{BP} = k_{11} + k_{12} + k_{21} + k_{22}$$

$$\cos\tau = \frac{k_{11} - k_{12} + k_{21} - k_{22}}{\sum k}$$

Fig. 2.8: Definition of the curvature and calculation of cos τ *for the lecture of* ξ *and* η *in abacus*

Table 2.2: Depth, maximum shear and contact stresses for different elliptical parameters k [SHI03]

k = b/a	0	0.2	0.4	0.6	0.8	1
z/b	0.785	0.745	0.665	0.590	0.530	0.480
τ_{max}/P_{max}	0.300	0.322	0.325	0.323	0.317	0.310

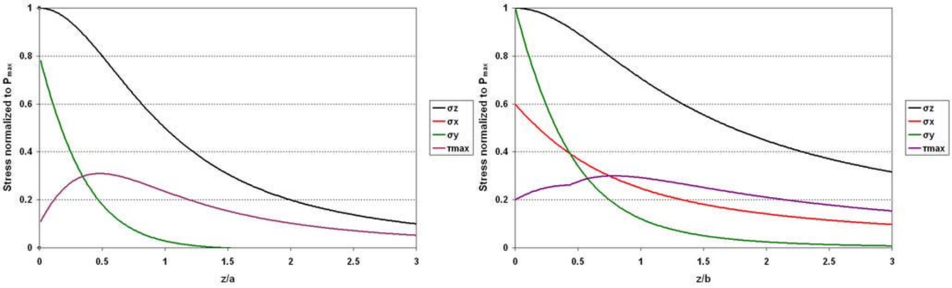

Figure 2.9: Variation of stress components beneath the surface of contacting spheres (left, $\sigma_x = \sigma_y$*) and cylinders (right, Diameter<<Length) made of steel (*ν *= 0.3). Stresses are normalized by the maximum Hertzian pressure.*

2.6 Lubrication regimes

Different lubrication types can be encountered. Their distinction is based on different domains of the Stribeck curve describing the evolution of the coefficient of friction with speed or sometimes the Sommerfeld number defined as “oil viscosity x sliding velocity / normal load”. The Stribeck curve can also be represented by the evolution of the friction with the ratio λ of lubricant film thickness to roughness ratio, sometimes simply called lambda ratio or also known as Tallian parameter.

It is commonly accepted that three main lubrication regimes exist and are presented in the *Figure 2.10* as follow:

- fully fluid or hydrodynamic, for $\lambda > 3$
- mixed also called in some cases partial-EHL, (elastohydrodynamic (EHD) lubrication) characterized by $1 < \lambda < 3$,
- and boundary lubrication with $\lambda < 1$,

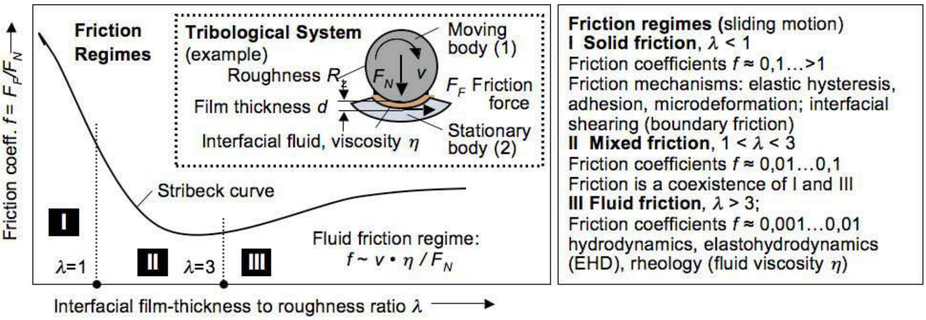

Figure 2.10: Characterisation of friction regimes according to the Stribeck curve [CZI03]

However another phenomenon affects the film thickness: the surface topography or “surface texture”, which refers to the arrangement or orientation of the roughness. For fully fluid or elastohydrodynamic lubrication, this is not a problem, as the facing surfaces are totally separated. The surface texture has no influence as the lambda ratio is high. But, as the facing surfaces are getting closer, the roughness texturing may play a role as the lubricant has a certain relaxation constant: the lubricant will not flow in the same way if the texture is oriented in the motion direction or if it is transversal. Typical contact area patterns for oriented rough surfaces are shown in *Fig. 2.11*. The parameter γ can be used to describe the surface pattern of the roughness. It is the ratio between the correlation lengths $\lambda_{0.5x}$ in the x and $\lambda_{0.5y}$ in the y direction at which the autocorrelation function of the profile is 50% of the value at the origin.

$$\gamma = \lambda_{0.5x} / \lambda_{0.5y} \tag{2.8}$$

The autocorrelation function is a measure of the wave length structure of a surface profile, defined as follows:

$$R_x(\lambda) = \frac{1}{l}\int_0^l \delta(x)\cdot\delta(x+\lambda)dx \tag{2.9}$$

Where here λ is the correlation length; δ is the height function along the x direction; and $R_x(\lambda)$ is the autocorrelation function in the x direction.

The surface roughness correction factor is established as

$$C_r = h_{rough} / h_{smooth} \tag{2.10}$$

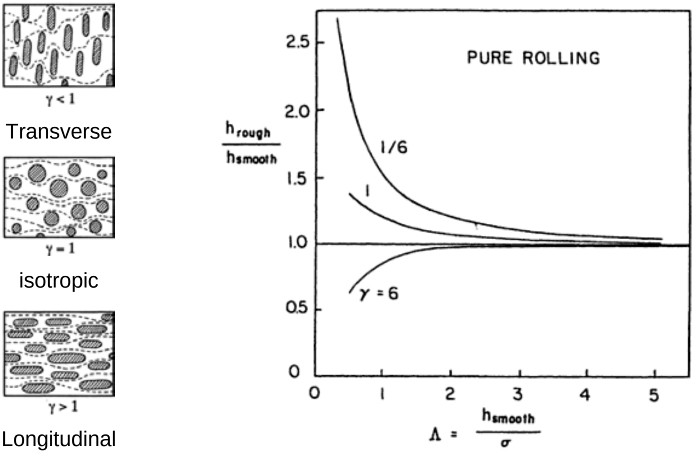

Figure 2.11: Effect of surface roughness on film thickness (for p_H/E = 0.003, pure rolling, G = 3333, $\sigma/R = 1.8 \times 10^{-5}$) [BOO97].

An example of the effect of surface roughness on the average film thickness of EHL contacts under pure rolling condition is shown in *Fig. 2.10* where here Λ is film parameter, $\Lambda = h_{smooth}/\sigma$. As it becomes clear from the diagram and as already mentioned, no significant influence of the orientation of the surface roughness is revealed in the EHL regime. But concerning the mixed/boundary lubrication, the correction factor is dramatically influenced by the parameter γ. It is above 1 for γ values under or equal to 1 and decreases under 1 for high values of the parameter γ, i.e. with a surface roughness oriented in the direction of motion. So, for the mixed/boundary domain, transverse orientation favours the lubrication as the correction factor is above 1. But a highly oriented longitudinal roughness degrades lubrication and actually makes the contact more severe.

The development of the calculations for the minimal lubrication film thickness started with Martin in 1916 and a lot of scientists tried to find out the governing parameters and their influence on the film thickness and friction. The EHD calculations are principally based on the works of Reynolds on fluid dynamics and Hertz on the resolution of the point contact between two elastics bodies. It is clear that only the viscosity cannot be sufficient to describe the film thickness. It is also determined by the materials in contact, the speed and the geometry of the moving parts, as well as the lubricant properties, such as its viscosity, but also its density, the coefficient of compressibility and the force applied are the main parameters to determine it. To take into account the compressibility and the piezoviscous state of lubricant, the models of Barus and later Roelands have to be incorporated in the calculation. Moreover, thermal effects should actually be taken in consideration for a better description. The most known and in-use model was developed by Dowson and Higginson [DOW77] at the end of the 1960 for the linear contacts, and then by Hamrock and Dowson at the end of the 1970 for point or elliptic contacts (1977). Cheng then introduced a correction factor to this work for the thermal contribution.

The adimensional EHD minimal film thickness H_{min} for elliptical contact is expressed by the equation (2.11) developed by Hamrock and Dowson [HAM81]. The assumptions made in their model are the following: an isothermal flow, a Newtonian, piezoviscous and incompressible lubricant, a fully flooded lubrication, an hard elastic material. (Exponents taken from [CZI03])

$$H_{\min} = \frac{h_{\min}}{R_x} = 3.63 \cdot U^{0.68} \cdot G^{0.49} \cdot W^{-0.073} \cdot (1 - e^{-0.68 \cdot k}) \tag{2.11}$$

With:

Speed parameter	Material parameter	Load parameter	Elliptical form parameter
$U = \frac{\eta_0 \cdot (v_1 + v_2)/2}{E' \cdot R_x}$	$G = \alpha \cdot E'$	$W = \frac{F_N}{E' \cdot R_x^2}$	$k = 1.0339 \cdot \left(\frac{R_y}{R_x}\right)^{0.636}$

In these parameters, η_0 is the oil dynamic viscosity at operating temperature, v the surface velocity, R_x is the reduced curvature radius in x direction, E' effective modulus of elasticity, α Pressure-viscosity coefficient at operating temperature and F_N the normal load.

The effective modulus of elasticity E’ and pressure-viscosity coefficient α are defined as:

$$\frac{1}{E'} = 2 \cdot \left(\frac{1 - \nu_1^2}{E_1} + \frac{1 - \nu_2^2}{E_2} \right) \tag{2.12}$$

$$\eta(p) = \eta(p_0) \cdot e^{\alpha(p - p_0)} \tag{2.13}$$

E_i and ν_i respectively are the modulus of elasticity of the material and Poisson’s ratio of the material in contact; p is the pressure applied, mostly p_0 is the atmospheric pressure.

2.7 Testing rolling contact fatigue with tribometers

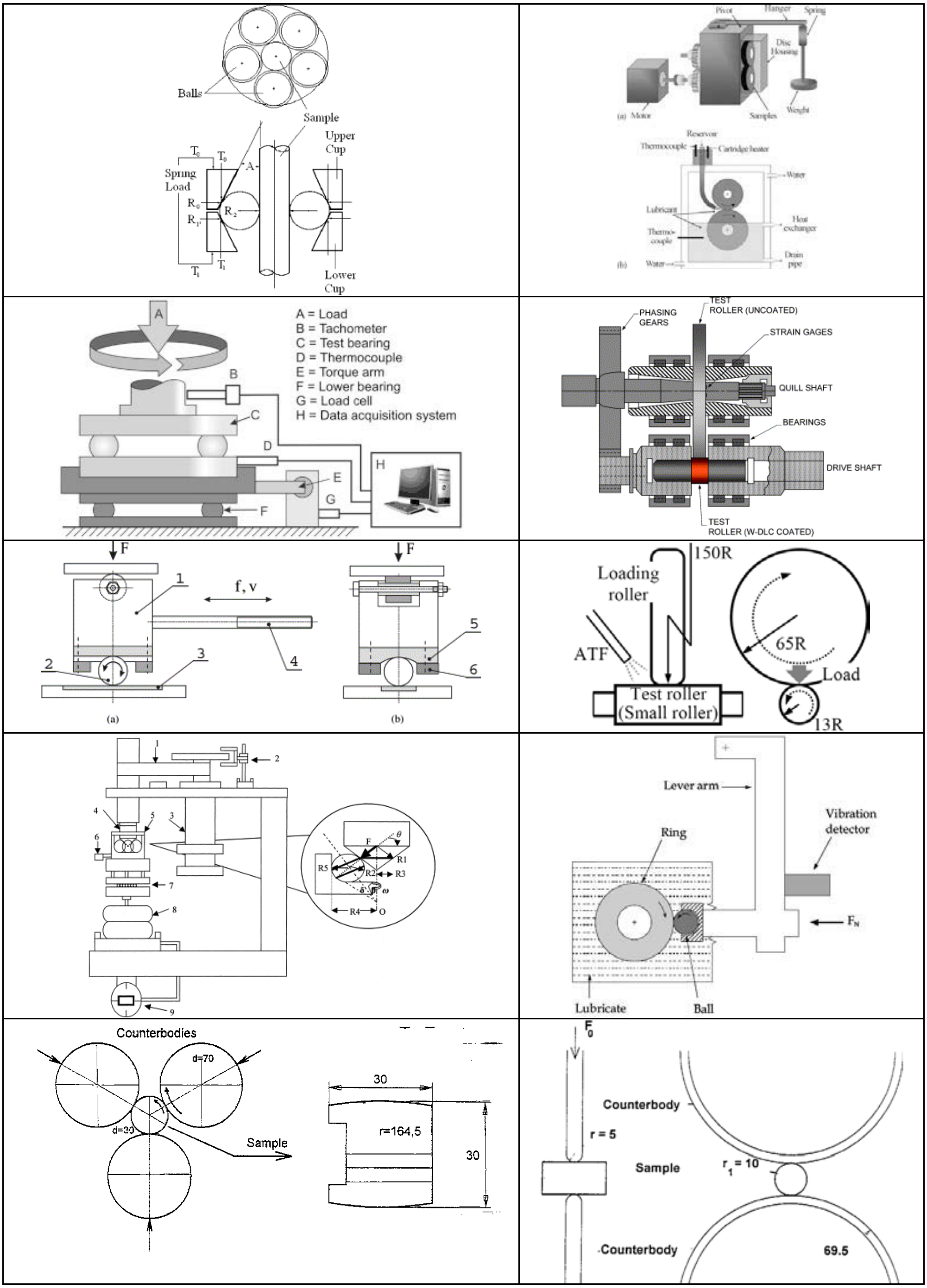

Figure 2.12: Some testing configurations used in rolling contact fatigue experiments: "ball-based" devises (left) and "cylinder-based" devises (right).

Figure 2.12 compiles most of the machines/arrangements used for testing in rolling contact fatigue. This is a non-exhaustive listing but illustrates the multiplicity of techniques, principles and samples geometries, principally based on ball configurations and disc configurations. Moreover, here no differentiation is made following lubrication principles. In the examples shown, lubrication systems are not taken into account as the lubricant can be dripped down or guided by the samples motion into the contact area. The samples can even be totally submerged in the lubricant itself or the lubricants can be only sprayed over a sample. So each testing machine can only offer its own testing conditions. Therefore, this does not ease the comparison of performances between coatings as each result depends on the testing conditions and consequently on the testing devise.

For comparison, the location beneath the surface of the maximal stress is depicted in *Figure 2.13* in the case of ZF-roll test rig and a twindisc testing device. It is obvious that the geometry of the sample and thence the testing devise influence the stress profile distribution. In consequence, the results of rolling contact fatigue depend on the sample geometry, i.e. contact geometry and cannot be compared.

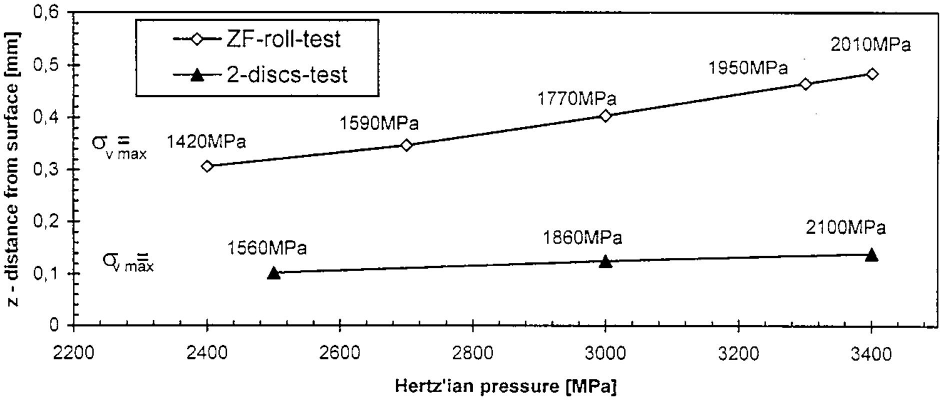

Figure 2.13: location of the stress maximum σ_{vmax} as a function of Hertzian pressure for ball-based and cylinder-based testing devises (pictures at the bottom of Fig. 2.12) [BAD98].

2.8 Overview of highly loadable coatings under rolling in literature

2.8.1 Crystalline coatings

The research in the domain of rolling contact fatigue of PVD coatings really started at the end of the 80's and at the beginning of the 90's in the USA [ERD88]. Erdemir appears as one of the first (after D. Scott in Great Britain in 1978 [SCO78]) to have published results on coatings tested under rolling contact fatigue. In the USA at this time, they used to test the coatings with three-ball-on-rod testing machines and lubricated with synthetic jet turbine lubricants, the rod being coated.

In the former USSR, at the end of the 80's, contact fatigue tests were also performed on a MKV-K machine (contact fatigue testing machine designed by the All-Union Scientific-Research Institute of the Polygraphic Industry) in running water and for comparison in Industrial-50 oil with a loading frequency of 250 Hz. The deposition method is not mentioned but it must be said that arc evaporation was firstly developed in Russia. It was observed (*Fig. 2.14*) that 5-7 µm thick titanium nitride coating increases the contact fatigue resistance of the specimens in running water 2-4 times in comparison to the uncoated specimens. During testing in oil the titanium coating did not fail at a base of 100 million cycles under a load of up to 4 GPa, and at a load of 5 GPa their lifetime was eight times longer than of the uncoated specimens. It was suggested that in general, the addition of the coating does not change the character of failure of specimens of hardened steel but does lead to a decrease in deformation and wear of the contact surface.

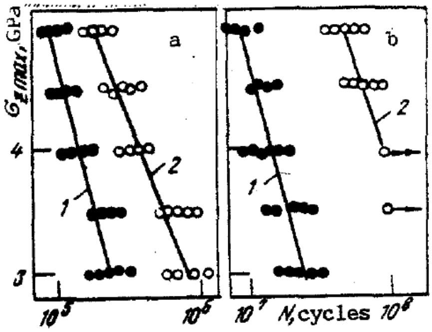

Figure 2.14: Contact fatigue of R6M5 steel specimens without a coating (1) and with a titanium nitride-based coating (2) in running water (a) and in industrial oil (b) [KAT86]

Closer to the work presented here, Erdemir [ERD92] mentioned that Cheng et *al.* [CHEN90] and Chang *et al.* [CHA90, CHA91] investigated the RCF behaviour of TiN-coated rollers using a twin-disk rolling contact machine at a maximum Hertzian contact pressure of P_{max} = 2.3 GPa. Coatings were deposited by high-rate reactive sputtering at temperatures below 200°C. In these studies, particular emphasis was placed on ascertaining the effect of TiN film thickness on RCF life of rollers. Fatigue test results were combined with electron microscopy observations to reveal the fundamental mechanism of fatigue failure initiation in the TiN-coated bearing steels. It was anticipated that by understanding the failure mechanism of coated bearings, analytical models enabling RCF life predictions can eventually be developed. In general, their test results were consistent with the earlier findings of Erdemir and Hochman [ERD88, ERD88-2] TiN coatings of 0.25 to 1 µm have substantially improved the RCF life of bearing-steel substrates and remained largely intact. TiN coatings of 0.25 µm lasted more than 60 million cycles and gave the best fatigue life improvement. Thicker coatings (2.5 to 5 µm), however, peeled off rather quickly and shortened the fatigue life of the steel substrates. For example, a roller coated with 2.5 µm thick TiN developed a large spall after 4.2 million stress cycles. The RCF life of uncoated specimens was about 10 million cycles.

Concerning ZrN coating on 440C steel produced by unbalanced reactive magnetron sputtering, it was reported that at high Hertzian pressure (5.4 GPa, three-ball-on-rod, 1.8 m/s, synthetic lube MIL-L-7808) its Weibayes (Weibull analysis when the slope parameter is selected beforehand, relating to Bayesian assumption, *one-parameter Weibull*, since one of the two standard Weibull parameters is already selected) B10 life increases gradually with the thickness of the coating (0.25, 0.50, 0.75 and 1 µm) (*Fig. 2.15*) and the 1 µm version was one of the best.

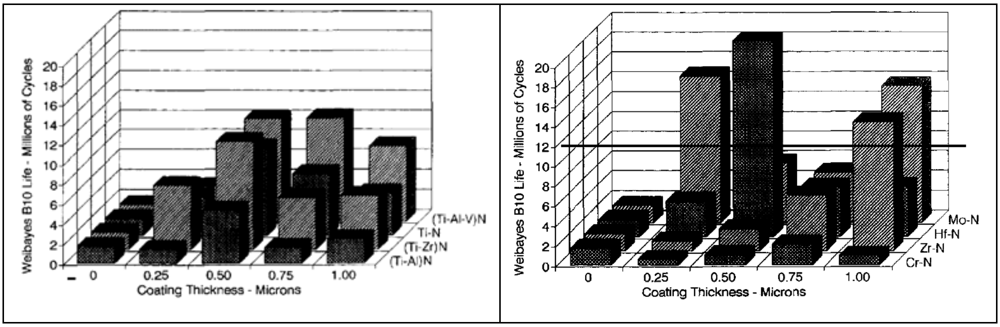

Figure 2.15: Weibayes B10 RCF life for magnetron sputtered nitrides coatings on 440C steel as a function of their thickness at a stress of 5.4 GPa [THO93].

In order to provide an overview of the scientific work on RCF with coatings, S. Stewart and R. Ahmed [STE02] carried out a review concerning the rolling contact fatigue of coated surfaces in 2002. The aim of the study was to establish the influence of design parameters such as the deposition process type, coating material and its thickness on the RCF performance. Data of coatings were compiled, which were deposited by thermal spray (HVOF, APS, D-Gun), PVD (ion platting, reactive sputtering, magnetron sputtering, Ion beam) and CVD methods (PACVD, PCVD, CVD) and tested under rolling fatigue. *Table 2.3* (from [STE02]) summarizes their general observations. Regarding to the values reported in this table, coatings produced by PVD techniques appear to be far superior to the ones deposited by CVD or even by thermal spray in terms of fatigue life and contact stresses.

Table 2.3: review of rolling contact fatigue of coatings from [STE02]

Coating process	PVD	CVD	Thermal spray
Thickness (µm)	0.25 → 5	2.5 → 5	20 → 450
Substrate hardness (HRC)	60	65	20 → 60
Coating hardness (HV)	810 → 1525	2000 → 2500	491 → 1300
Contact stress (GPa)	0.4 → 5.5	0.2 → 7	0.41 → 5.8
Surface roughness	0.03 → 0.1	0.02 → 0.6	0.02 → 0.35
Fatigue life (million cycles)	100 → 300[a]	0.5 → 25[b]	3.3 → 70[c]

a Maximum value at contact stress of 5.5 GPa for TiN or DLC coating of approximate thickness 0.5 µm [POL98,WEI92].

b Maximum value at contact stress of 5.5 GPa for SiC–30%TiC coating of thickness 190 µm [DIL84].

c Maximum value at contact stress of 2.7 GPa for WC–12%Co coating of thickness 250 µm [AHM01].

Stewart and Ahmed pointed out that it is generally difficult to synthesize all of the RCF results to gain a comprehensive understanding of the parameters which can have a significant effect on a coating's resistance to rolling contact fatigue. Effectively the testing methods and conditions differ extremely from experimenter to experimenter and therefore are not directly comparable as it was earlier described for bulk silicon nitrides tested under different rolling procedures [HAD95]. Presently there not exists a standardized method to qualify the rolling resistance of coated parts. This is quietly accepted as each tribological problem functions under its own operating parameters (rolling speed, slip amount, lubricant properties, working temperature, roughnesses of the contacting parts…), but precisely it does not allow a direct comparison of the results.

Table 2.4: Published findings for RCF performance of PVD coatings from [STE02]

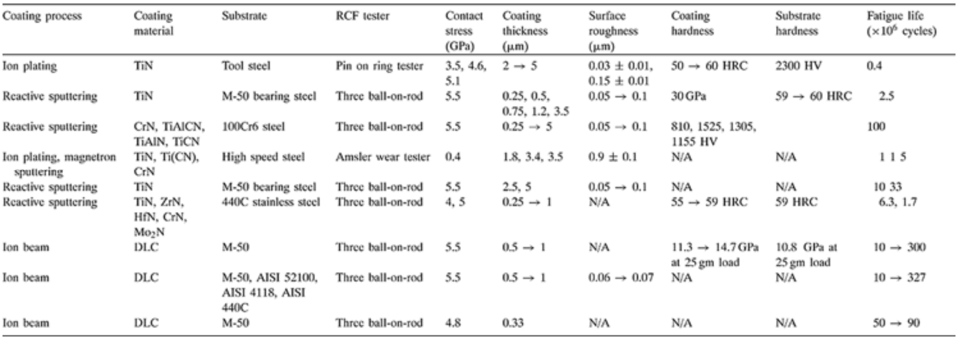

Coating process	Coating material	Substrate	RCF tester	Contact stress (GPa)	Coating thickness (µm)	Surface roughness (µm)	Coating hardness	Substrate hardness	Fatigue life ($\times 10^6$ cycles)
Ion plating	TiN	Tool steel	Pin on ring tester	3.5, 4.6, 5.1	2 → 5	0.03 ± 0.01, 0.15 ± 0.01	50 → 60 HRC	2300 HV	0.4
Reactive sputtering	TiN	M-50 bearing steel	Three ball-on-rod	5.5	0.25, 0.5, 0.75, 1.2, 3.5	0.05 → 0.1	30 GPa	59 → 60 HRC	2.5
Reactive sputtering	CrN, TiAlCN, TiAlN, TiCN	100Cr6 steel	Three ball-on-rod	5.5	0.25 → 5	0.05 → 0.1	810, 1525, 1305, 1155 HV		100
Ion plating, magnetron sputtering	TiN, Ti(CN), CrN	High speed steel	Amsler wear tester	0.4	1.8, 3.4, 3.5	0.9 ± 0.1	N/A	N/A	1 1 5
Reactive sputtering	TiN	M-50 bearing steel	Three ball-on-rod	5.5	2.5, 5	0.05 → 0.1	N/A	N/A	10 33
Reactive sputtering	TiN, ZrN, HfN, CrN, Mo_2N	440C stainless steel	Three ball-on-rod	4, 5	0.25 → 1	N/A	55 → 59 HRC	59 HRC	6.3, 1.7
Ion beam	DLC	M-50	Three ball-on-rod	5.5	0.5 → 1	N/A	11.3 → 14.7 GPa at 25 gm load	10.8 GPa at 25 gm load	10 → 300
Ion beam	DLC	M-50, AISI 52100, AISI 4118, AISI 440C	Three ball-on-rod	5.5	0.5 → 1	0.06 → 0.07	N/A	N/A	10 → 327
Ion beam	DLC	M-50	Three ball-on-rod	4.8	0.33	N/A	N/A	N/A	50 → 90

Furthermore, as previously evocated for uncoated steels submitted to rolling, substrate nature, substrate elaboration way, substrate surface states, deposition method, parameters for deposition of the coating, coating chemistry, coating structure, and derived mechanical properties, are further factors jeopardizing any comparison and interacting between themselves. Trends can be seen but there are too many conditions to permit any assessment between coatings.

Additionally, in their study, Stewart and Ahmed mentioned [STE02] only vaguely the lubrication conditions, that is why some coatings appeared effective under very high Hertzian pressures, for example the PVD TiN with 0.5 µm thickness under 5.5 GPa. According to the reference cited, it was achieved under very high rotation speed, i.e. probably not in mixed boundary lubrication regime and actually with lubricant MiL-L-23699D (synthetic turbine oil, most likely highly additivated).

Some years before this review, in 1999 Erdemir carried out the same kind of work but principally focused on hard coatings deposited on bearing steels [ERD99]. Results of nitrides, carbides and DLC coatings are mainly reported. He concludes that the first and most important requirement is that the coating must remain intact on the rolling contact surfaces. Thinner hard coatings, 0.2 to 1 µm thick, seem to provide the best overall performance under high-stress RCF situations. Hard coatings thicker than 2 µm undergo severe delamination and/or fracture and, in most cases, reduce the RCF life of the base steels, especially under high contact stresses (5.42 GPa).

Nevertheless a model imagined by Polonski et al. [POL97] mentions that the efficiency of hard coating against rolling contact fatigue would be optimized with a coating thickness in the range of 3 µm or more. In order to achieve this potentially better performance with thicker coatings, the thicker coating should have a fine structure and resistance to cohesive failure to achieve an improvement over thinner ones. To assess this model, RCF tests were carried out with TiN coatings of different thicknesses, namely 0.25, 0.5, 0.75, 1, 2, 3 µm. Experimentally the most effective coating had an optimal thickness of 0.75 µm. The authors agreed that microstructure for optimal 3 µm thick PVD TiN coatings needs improvement.

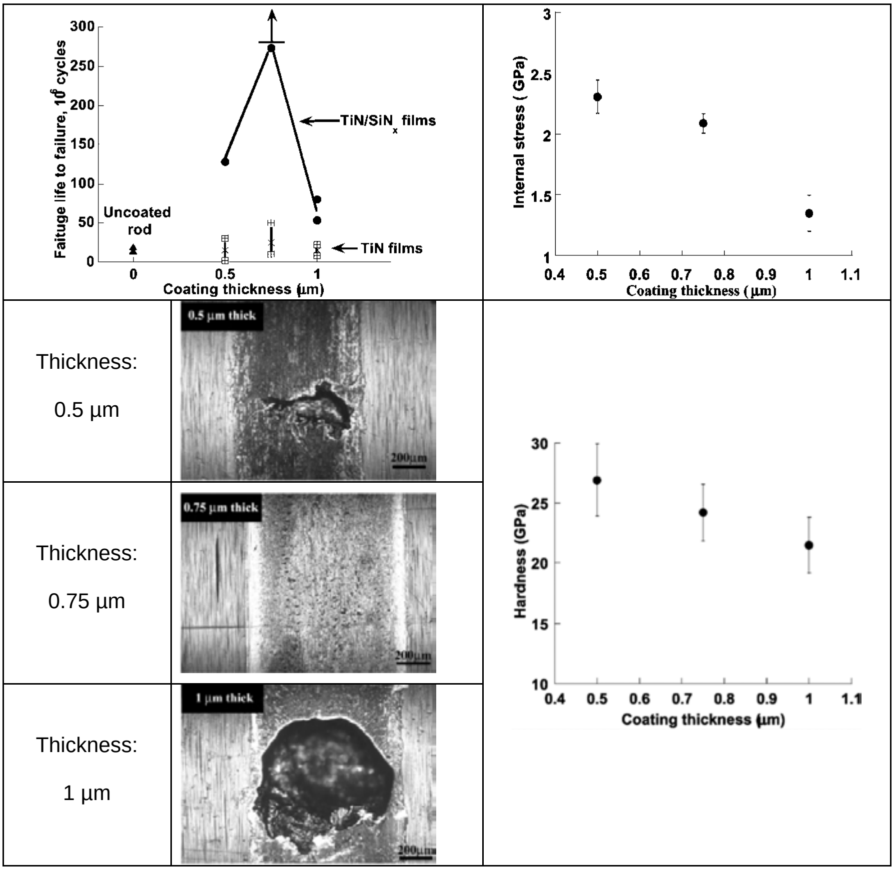

Figure 2.16: RCF results of TiN/SiN$_x$ multilayer coatings and corresponding optical micrographs compared to uncoated state and to TiN coatings as a function of the whole coating thickness; hardness and internal stresses (measured by substrate curvature) are also given. From [CHE02]

For this purpose, a few years later TiN/SiN$_x$ multilayer coatings were produced with dual-cathode unbalanced reactive magnetron sputtering and tested under sliding [CHE02]. The architecture of the coating was composed of TiN layers of 2 nm separated by SiN$_x$ single layers with thicknesses from 0.3 to 1.0 nm. The 0.5 nm SiN$_x$ version displayed the best nanoscratch wear resistance; the higher wear resistance under sliding was obtained with the lowest substrate bias, i.e. here –60 V. Therefore they produced also “2 nm TiN + 0.5 nm SiN$_x$” multilayer coatings (with a 80 nm TiN buffer layer) of different total thicknesses (0.5, 0.75 and 1 µm) on M2 steel at a pulsed substrate bias voltage of -40 V and tested them under RCF (three-ball-on-rod at 1083 N, i.e. P_{max} = 5.5 GPa, 3600 rpm, MiL-L-23699D, stop by vibration detection). The most successful coating was again the 0.75 µm thick one (see *Fig. 2.16*). This figure summarizes the major characteristics of these coatings.

According to this TiN/SiN$_x$ coating system, Veprek et al. also worked on ncTiN/a-Si_3N_4 coating systems (nc = nanocrystalline, a = amorph), but with a slightly different concept: TiN nanocrystallites are not organised in layer but embedded in an amorphous matrix to ensure what they called super-strengthening. This 3D-nanocomposite originates from selforganization processes, including segregation effects during growth and spinodal decomposition. However no rolling fatigue results are nowadays published for such systems. Regarding this coating concept, it should be mentioned, that toughness and low friction coefficient are important requirements for wear resistance coatings in [ABA08].

2.8.2 Amorphous coatings

Beginning of the 90’s, the research teams from Evanston and Argonne (IL, USA) of Polonski first tested rolling resistance fatigue by applying 33 nm thick DLC coatings on steel, in addition to research on RCF of TiN coated M50 steel (~ 80MoCrV42-16, DIN EN 1.3551). At the same time, Wei et al. tested fatigue hard carbon coatings on M50 steel under rolling contact with a three-ball-on-rod testing machine at 5.5 GPa and 3600 rpm (coated rod), with an estimated lubricant film thickness parameter λ of about 0.7. Following the Weibull plot, the hard carbon coated rods behave more effective than uncoated rods towards rolling contact fatigue, since the Weibull slope was found to be much lower (0.6 for coated < 3.5 for uncoated). Nevertheless, the B50 life is enhanced but the B10 life is degraded with coated rods. It was supposed by the authors that the nature of the fatigue process changes at about 2 million cycles.

So, more recently (i.e. not in reported [STE02]) thrust bearing discs made of 100Cr6H coated with different Cr/W-C:H coatings produced by PVD (unbalanced magnetron sputtering and reactive ion plating) were tested and validated under lubricated rolling motion at P_{max} of 1.6 GPa (corresponding to FZG = 10-11) [YON05]. With a SAE 10W-40 oil as lubricant (HTHS= 3.93 mPa·s) and an estimated slide amount of 10%, they reached between 0.5 and 2 billion cycles, the tests being interrupted when vibrations due to pit formation or coating delamination was detected.

Also application oriented, with a similar coating on consumable-electrode vacuum-melted (CVM) and case-carburized AISI 9310 steel (Hardness of the surface = 60 HRC), an improvement of the surface fatigue live of coated spur gears were reported in [KRA03]. The tests were performed in the NASA Glenn Research Center’s gear test apparatus. A six-fold increase of the Weibull L_{10} and L_{50} lifes (with Weibull slopes assumed as equal) was found out at a pitch-line maximum Hertzian pressure P_{max} = 1.7 GPa at a rotation speed of 10,000 rpm (pitch-line velocity of 46.5 m/s) in paraffinic oil with 5% Lubrizol 5002 (extreme pressure additive), mixture similar to 5-centistoke oils used for helicopter main gearboxes. Some tests were suspended due to the high longevity of the coatings.

Shorter lifecycles were reported for a PACVD coating [LIU07] with the following structure Cr/Cr-WC/WC-C/a:C-H. Its thickness was 3 µm on SAE 4122 steel (0.97% Cr, 0.42%Mo, 0.22% C). It was tested on a two-disc machine with 21% slip at a speed of 2.68 m/s under a maximum Hertzian pressure of 2.8 GPa. This proprietary development and coatings from other industrial sources could not achieve a test time of more than 72 hours. The test duration of the same coatings were limited to 120 hours during a FZG test at 82°C in SAE 50 oil.

With Plasma-CVD-DLC and -DLC-Si coating on a carburized steel, SCr420H (Fe-0.2C, 1.0Cr, 0.25Mo, deposition at 230°C) the rolling resistance of the coated steel increased by two orders of magnitude to twenty millions cycles in comparison to the same uncoated steel [KUM06] (*Fig. 2.17a*). This performance was accomplished on a two disc testing machine with an ATF (Automatic Transmission Fluid) oil at 90°C under a maximum Hertzian pressure P_{max} = 3.0 GPa with 60% slip created via a difference in diameter of the contacting discs, both rotating at a high speed of 1,500 rpm.

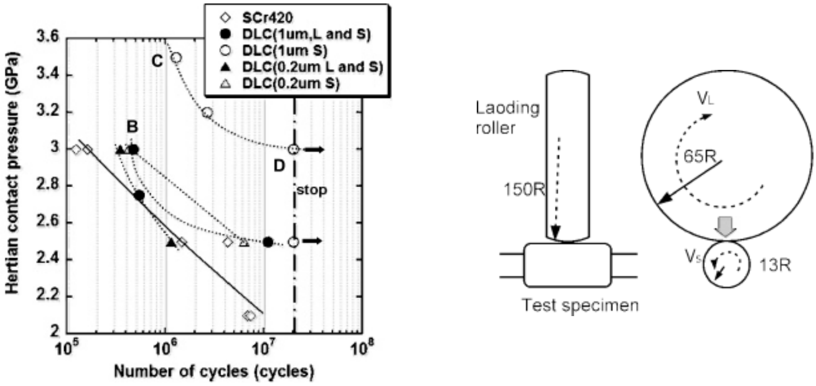

Figure 2.17a: Relationship between number of cycles and Hertzian contact pressure for SCr420H steel with DLC coatings obtained with the sample arrangement shown on the left in MKV device [KUM06]

Table 2.5: Different coatings tested on steel SCr420H [KUM07]

Example	**Film forming process**	**Coefficient of friction**	**Film**	**Thickness of film [µm]**	**Film forming temperature [°C]**	**Hard-ness [HV]**
1	Plasma CVD	0.2	DLC	0.68	230	2400
2	Plasma CVD	0.2	DLC	0.2	220	2000
3	Plasma CVD	0.2	DLC	1.1	220	2000
4	Plasma CVD	0.2	DLC	1.1	210	1500
5	PVD	0.2	DLC	1.2	200	3000
Comp. 1	-	-	None	-	-	-
Comp. 2	PVD	0.6	TiN	2.5	450	1800

The performances of the DLC coatings were also compared with a TiN coating with the same testing method (*Tab. 2.5* and *Fig. 2.17b*). Higher slip-rolling resistance was reported for all the DLC than for the TiN coating, but it must be mentioned that this titanium nitride thin film was deposited at a far higher temperature of 450°C that the substrate could not sustain, which led to the reduction in surface strength of the substrate.

Moreover, a complex MoS_2/Ti coating was tested on a DIN 20MnCr5 steel of hardness 59 HRC with different slip rates (6.8%, 19.6%, 28.4% und 40.9%) at a rotating speed of 3,000 rpm (11 m/s) under a P_{max} of 1.5 GPa [AMA05]. The tests were carried out up to 1 million cycles with an unadditivated ISO VG 22 oil at 90°C and samples with a surface roughness of R_a between 0.33 µm and 0.48 µm. The damage was evaluated with microscopic observations and expressed by means of PCW (Percentage of coating wear). The best result achieved was 18% PCW. However, in FZG tests (C gears, R_a uncoated: 2.4 µm; R_a coated: 0.4 µm) with an ISO VG 100 mineral oil as lubricant, this complex coating allowed to increase FZG load stage by a factor two at 1,500 rpm and by five at 3,000 rpm compared to the uncoated steel [MARt08].

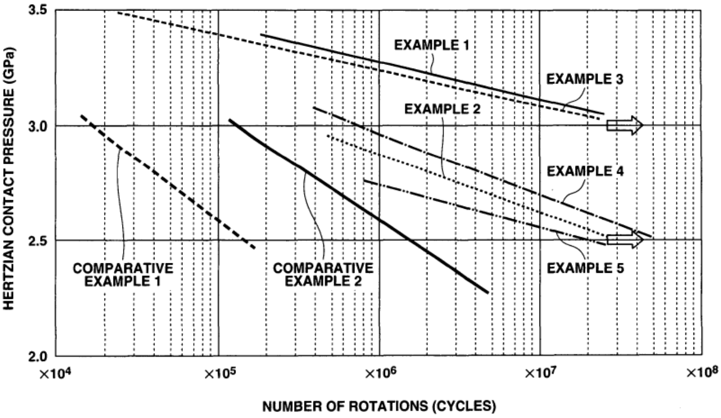

Figure 2.17b: Maximal Hertzian pressure P_{max} vs. numbers of cycles from the experimental data of the coatings described in table 2.5 [KUM07]

Recently, in Sheffield (UK), a range of coatings and surface treatments were evaluated under slip-rolling contact with a slip level of 0.5%. Tests were run lubricated in grease and dry at a rotational speed of 400 rpm and at P_{max} = 3.65 GPa (1500 N) [GAL09]. In dry conditions, the vibro-polishing surface treatment showed excellent wear resistance during 50,000 cycles. In lubricated conditions, all treatments and coatings tested during 10,000 to 50,000 cycles resulted in low friction and wear, particularly the tungsten carbide coating, a solid lubricant coating with graphitic microcrystalline structure and a DLC (ta-C:H) on top of plasma nitrided substrate made in a nitrogen martensitic stainless bearing steel.

Many years ago, the BAM (Institute for Materials Research and Testing, Berlin, Germany) started the development and testing of coatings in order to improve their rolling contact resistance under high demanding conditions [SPA04, SPA08, MAN08]. In the early stages, relative unsatisfactory results were achieved since the best coatings could only resist an average Hertzian pressure P_{0mean} in the range of 1.0 - 1.25 GPa at room temperature RT, which is far from the requested FZG load stage 13, and in addition the lubrication regime in the TwinDisc was near to hydrodynamic. Gradually the carrying capacity was improved to Hertzian contact pressures approximately corresponding to FZG load stage 14 (P_{0max} = 2,170 MPa). Technologically considered coatings become henceforward meaningful and functionally advantageous. This stage threshold marks the beginning of profitableness of applying coatings.

With respect to the literature found, a trend towards a better rolling resistance of PVD coatings could be perceived. However, in all the literature found, the testing conditions correspond almost always to the EHL or mixed regime, as the rotation speeds (and metric speeds related to the geometry) are relatively high. They permit to achieve plenty of cycles and tests in reduced time, but do not refer to the most severe lubrication mode, the mixed/boundary regime, which always takes place in any case at the start and the stop of mechanical parts or working under slow motion and/or high lubricant temperature.

ZrC based coatings are principally studied at the RWTH Aachen (Germany), mainly on FE8 test rig (cylindrical roller thrust bearings) [GOL07] in different configurations (*Fig. 2.18*). So far, no literature seems to be available concerning the performance of Zr(C,N) coatings at the moment.

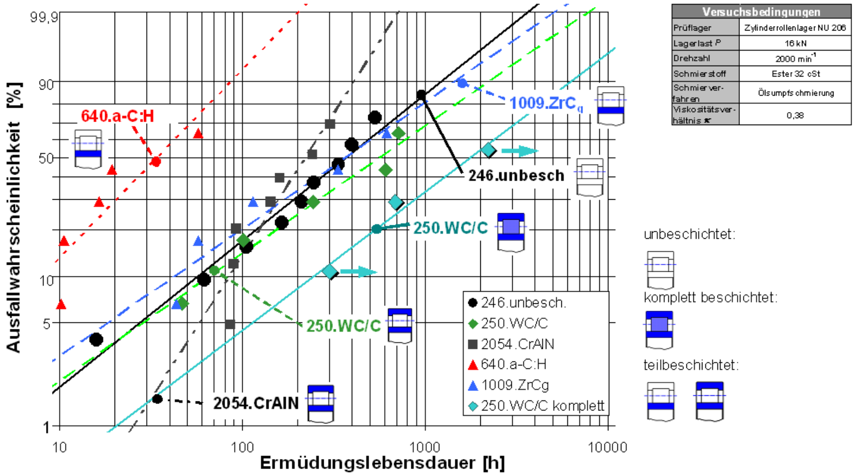

Versuchsbedingungen	
Prüflager	Zylinderrollenlager NU 206
Lagerlast P	16 kN
Drehzahl	2000 min^{-1}
Schmierstoff	Ester 32 cSt
Schmierverfahren	Ölsumpfschmierung
Viskositätsverhältnis κ	0,38

Figure 2.18: Weibull diagram representing results on FE8 test rig for differents coatings and testing configurations in TMP ester oil at P_{max} = 2,134 MPa [GOL07].

2.9 Vapour deposition

The vapour deposition process can be divided into two major groups:

- the Chemical Vapour Deposition (CVD),
- and the Physical Vapour Deposition (PVD)

These two deposition methods have in common the formation of a vapour or gas of a material and then its condensation on a substrate to form a coating. But the principal difference resides in the material origin: during the PVD process the deposition is purely physical and the material comes mainly from a solid state. In the case of the CVD process, the material deposited comes from chemical reactions between different gases. Moreover the CVD process generally requires higher temperatures conditions for a proper deposition and also for activation of the deposition reactions. But recently the CVD techniques have progressed to lower deposition temperatures thanks to plasma enhanced/assisted technologies.

The PVD is a process which permits the deposition of material on substrates through condensation of vapour and regroups different techniques, the main ones being:

- the thermal evaporation,
- the cathode pulverisation or sputtering
- the ion platting deposition
- and pulsed laser deposition

The PVD techniques do not require temperatures as high as the pure CVD techniques. Usually the deposition temperatures vary between 200°C and 500-550°C. Lower temperatures can be achieved with the use of plasma enhanced techniques compared to those in the case of the CVD.

The arc evaporation technique is interesting for industrial deposition of hard coatings offering some advantages such as high adhesion of the coating [SAN00] and disrupting of columnar growth through high deposition energy. Faraday and Edison found the principle of arc evaporation but from the industrial point of view, historically it emerged in the USSR (Kharkov, Moscow and St Petersburg) and then in the USA [SNA71, SAB74] at the end of the 60’s and then extended to the “West” [GOR98]. The term arc evaporation however is a misnomer from a physics point of view since the flux of neutral metal vapour is usually negligible compared to the flux of ions [SAN00]. Cathodic arc plasma deposition (CADP) is more appropriate. Sometimes it is also called cathodic arc deposition or simply Arc-PVD. This method can be described as a combination of two deposition techniques, the “pure” vacuum evaporation and the (reactive) plasma ion platting. This deposition method has several advantages, such as high ionization degree of the evaporated species, a somewhat low contamination and high deposition rate. The ionized species travel toward the substrate to higher energies than the conventional evaporation which favours the quality of the deposited coating. This technique, industrially used in the preparation of nitride thin films, is also being used to produce oxides, metals and carbides.

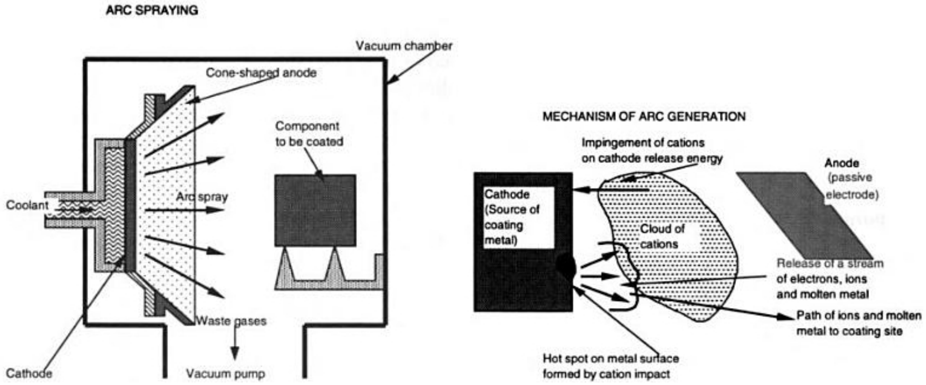

Figure 2.19: Principle of operation of an arc evaporation system or CVA Cathodic Vacuum Arc deposition from [BAT99]

During operation, an electric discharge is obtained by imposing a cathodic polarity on the coating material, which is in the form of a disc while an anode is built into the surrounding apparatus. Careful cooling by water jackets of both the cathode (coating material often a pure metal) and the anode is necessary to prevent bulk melting of either. The substrate is arranged in front of the cathode to receive the ionized flux of metal ions which form the coating (*Fig. 2.19*). The introduction of reactive gas such as nitrogen permits the formation of compounds coatings such as nitrides. It is put forward that ion bombardment of the coating surface influences gas adsorption behaviour by increasing the sticking coefficient of gases such as nitrogen and changing the nature of adsorption sites from lower energy physi-sorption sites to higher energy chemi-sorption sites [SAN00]. This would explain the high efficiency of cathodic arc process in forming nitrides or carbides thin film coatings during reactive deposition.

Besides the challenge of controlling the location of the arc on the cathode, one of the major drawbacks of this technique is the emission of micrometer-sized droplets of liquid cathode material known also as 'macroparticles'. Nowadays that has been partly controlled thanks filtering, the process is then called FCVA (Filtered Cathodic Vacuum Arc) deposition. Steered arc and pulsed arc represent another possibility to reduce droplets formation with the inconvenient of a lowering of the deposition rate compared to DC modus for conventional DC arc equipments. These droplets may only be a few micrometers in diameter but they are sufficient large to form large "lumps" on the substrate surface after cooling and solidification. Ideally a coating should be smooth and of uniform thickness as well as composition so that these protuberance do not degrade the coating.

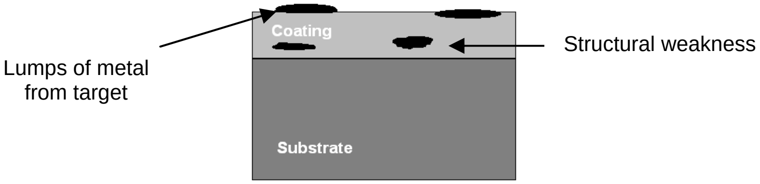

Figure 2.20: Schema of lumps affecting uniformity of coatings [BAT99]

The physical cause of the droplets is still unclear. It is believed that non uniform electric discharges form such defects by creating so called active spots where the metal is abnormally molten. Particles are ejected from those cathode spots generating macrodroplets as co-products of cathodic arc plasma containing high energy ions.

2.10 Some zirconium based materials

2.10.1 Zirconium

Zirconium is a malleable metal (if pure) with silver shine and belongs to the family of the transition metals. When exposed to oxygen, a thin oxide layer forms and passivates the metal. It has been firstly identified in 1783 and isolated in 1842. It is not a native metal (i.e. is not naturally present on earth in its metallic state) and is mainly extracted from the mineral zircon ($ZrSiO_4$). The actual major extraction sites are located in Australia and South Africa, countries with the highest geological resources of zirconium in its mineral form.

Zirconium can be considered as a precious by-product of the mining and processing of titanium minerals, such as rutile. [CAL08]. To produce metallic zirconium, firstly ZrO_2 is formed and then attacked by chlorine gas Cl_2 and carbon at about 800°C to form zirconium chloride $ZrCl_4$ which then is reduced by magnesium to form metallic zirconium as the standard free energy of formation of MgO, $\Delta G_{f\ MgO}$, lays under its of ZrO_2 in the Ellingham diagram. This represents the principal steps of the pyrometallurgical method called Kroll process, which is also used for the production of metallic titanium and hafnium. Economically, compared to titanium and hafnium, zirconium price is situated between these two metals. As their production processes are similar, their price should follow their geological and market occurrence. In Table *2.6* a comparison based on the prices of 1998 is given between Zirconium, Titanium and Hafnium in a same semi product state, the sponge metal [PRICE98].

Table 2.6: Prices in 1998 of Zr, Ti and Hf sponge metals [PRICE98].

1998	Zr sponge metal	Ti sponge metal	Hf sponge metal
$ / kg	~ 24 (250 powder)	~ 9	~ 190

Zirconium exhibits two crystal forms. Under 876°C, zirconium crystallises in its hexagonal close packed form known as α-Zr. Above this temperature, Zirconium undergoes a diffusionless allotropic transformation and takes a body centred cubic phase, β-Zr, like titanium (T = 882°C, P_{63}/mmc, hcp, to Im3m, bcc) and hafnium. Some of its properties are recapitulated in *Table 2.7*.

Table 2.7: Some properties of pure zirconium

Atomic mass	91.224
Melting temperature	2125 K
Boiling temperature	4650 K
Density	6.51 g/cm^3
Ionisation energy	6.84 eV
Oxidation number	**4**, 3, 2, 1
Atomic radius	160 pm
Ionic radius	87 pm (+4)
Young's modulus (Polycrystalline)	97.1 GPa [LID97]
Shear modulus (Polycrystalline)	36.5 GPa [LID97]
Poisson's ratio	0.33 [LID97]

Contrary to titanium, zirconium is not used for aeronautical purposes because of its high density. Its principal use in industrial applications concerns the nuclear domain, where its alloy category named Zircaloy, all containing over 97 wt.-% zirconium, absorbs the most of the world production. It serves as cladding material for rods containing uranium and used in nuclear reactors (because of its very low absorption cross-section of thermal neutrons) since the beginning of the 1950, when it has been internationally decided to use it for this aim. (Thence it partly explains the switch from the Hunter Process towards the more efficient Kroll Process and the production increase of zirconium from this date). Another production process named FFC Cambridge Process is currently tested at a semi industrial scale and avoids the use of expensive magnesium). Zirconium powder is used in pyrotechnic and as propeller or weapons as it reacts violently with oxygen and light inflammable. It is also used as "getter" in vacuum tubes [LID97].

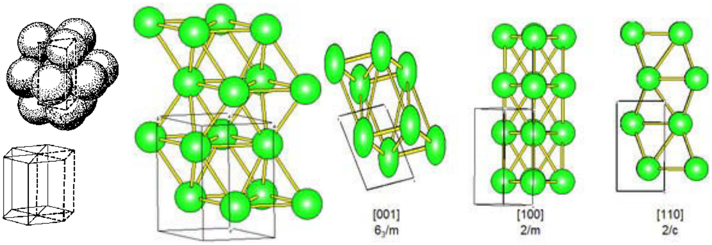

Figure 2.21: crystallographic structure of pure zirconium

2.10.2 Structure and properties of ZrC

Zirconium carbide (ZrC) is an extremely hard refractory ceramic material, commercially used for cutting tools. It is usually processed by sintering. It has the appearance of a grey metallic powder with cubic crystal structure. It is highly corrosion resistant. Like most carbides of refractory metals, zirconium carbide is substoichiometric, i.e., it contains carbon vacancies. At carbon contents higher than approximately $ZrC_{0.98}$ the material contains free carbon (*Fig. 2.22*).

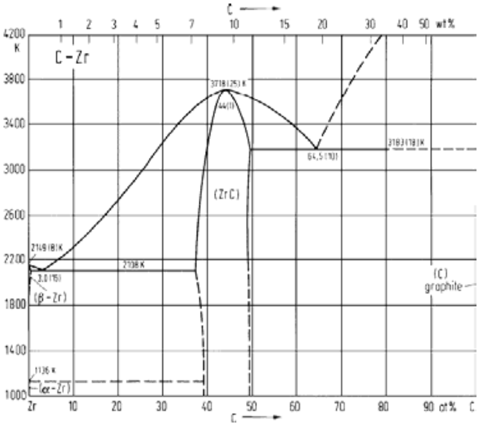

Figure 2.22: Zr-C phase diagram [PRE98]

2.10.3 Structure and properties of ZrN

The solid solution of N in Zr can be described as nitrogen at interstitial sites in metallic zirconium. As in the Ti-N phase diagram, the Zr-N system contains two domains of solid solutions for low nitrogen contents. The solution of nitrogen in hexagonal α-Zirconium (P_{63}/mmc, a = 3.2318 Å , c = 5.1483 Å) reaches about 21 At.-% (at room temperature). The β-Zr solid solution (Im-3m a = 3.5453 Å) exists only at high temperatures (above 882°C) and for N concentration until 5.5 At.-% at 1850°C.

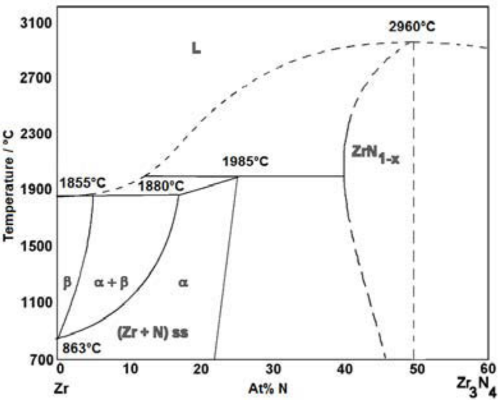

Figure 2.23: Phase diagram of the system Zr-Zr_3N_4 from [KIN94]

Above 45% at low temperature (this amount can differ between authors) a unique FCC phase ZrN_{1-x} appears. This phase can vary in its stoechiometry and can be seen as two overlapping FCC systems, the first for Zr and the second for N (*Fig. 2.23*). For a Nitrogen amount under 50% (or x>0), the formed ZrN phase is substoechiometric. From the literature, a saturated phase ZrN_{1+x} exists too, and is then overstoechiometric. This is related to the good solubility of N in Zr. ZrN with the ideal ratio N/Zr = 1 crystallises in the rock salt structure. A mono crystal with the perfect concentration ratio N/Zr = 1 was analysed with neutron diffraction [CHR75], where the whole octahedral sites of the FCC-structure (a = 4.585 Å) were filled / occupied. It was then observed that variations around the ideal ratio value of N/Zr = 1 (i.e. in the existence domain of the FCC-ZrN phase) do not really influence the crystal lattice parameter ($ZrN_{0.83}$=4.585 Å, $ZrN_{1.00}$ = 4.584 Å ; Rudy 1961, $ZrN_{0.86}$: 4.580 Å, $ZrN_{1.00}$: 4.578 Å ; [CHR77]) contrary to the similar structure of δ-TiN. With higher amount of Nitrogen in ZrN_{1+x}, a small decrease of the lattice parameter was registered correlated with higher x values ($ZrN_{1.02}$: 4.569 Å ; $ZrN_{1.22}$: 4.550 Å, [JUZ64]). However it should be noticed the samples in this study were not totally made of one phase, i.e. contain a second phase with a composition near to Zr_3N_4 and could correspond to orthorhombic Zr_3N_4. Low amount of oxygen in deposited ZrN films seems to have no influence on the cubic crystalline phase [VAZ04].

Alike TiN, ZrN (zirconium mononitride) displays a very yellow colour with metallic shine near to the color of gold, and therefore makes it suitable for decoration purposes as previously mentioned. Its colour depends on its stoechiometry. It can be altered by the amount of nitrogen present. Alike a lot of nitrides and carbides based on transition metals of IVb, Vb und VIb (such as TiC, TiN, ZrC, ZrN, HfC, HfN, VC, VN, NbC, NbN, TaC, TaN, CrN, $Cr_{23}C_6$), ZrN phase is cubic and belongs to the space group Fm-3m (NaCl structure), Nr 225. The stoechiometric phase melts at high temperature, i.e. 2980°C under nitrogen atmosphere. It is one of the most stable nitride based on transition metals with metallic conductivity. No structural changes or phase transformations take place until reaching the melting temperature. Contrary to the Ti-N and Hf-N systems, no subnitride phases are known. This material becomes supraconductor under 8 K.

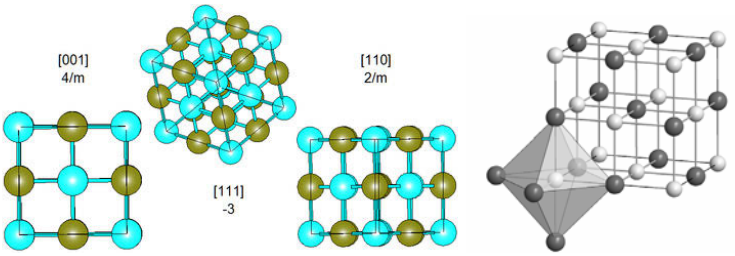

Figure 2.24: Elementary cell of ZrN and its octaedral coordination of cation or anion [DZI09]

Compared to bulk cubic TiN, higher fracture toughness is reported for bulk ZrN. In the case of bulk TiN, toughness values between 2.7 and 3.5 $MPa.m^{½}$ [RUS07] or 5.0 $MPa.m^{½}$ (bulk, hot isostatically pressed, ~1% porosity) [DEM89] are reported. Bulk ZrN seems to possess an higher toughness (bulk, hot isostatically pressed, ~1% porosity) in the range of 5.9 to

6.6 MPa.m$^{\frac{1}{2}}$ [ALE93]. Regarding these values, ZrN films should be superior to TiN ones (although properties of coating materials differ often greatly from their bulk state).

As in the case of TiN, the preferred orientation of ZrN coatings is mainly (111) and can be changed to (200) depending on the bias voltage and chamber pressure (i.e. (111) to (100) with higher N content in the film). Lower droplets amount than with TiN was often reported probably because of the higher melting temperature of Zr.

ZrN coatings can be achieved by employing divers deposition techniques such as ion beam assisted sputtering, reactive ion beam sputtering, magnetron sputtering, vacuum arc deposition, pulsed laser deposition and even chemical vapour deposition [BEN02]. These methods can engender two kinds of coatings:

- a stable ZrN or ZrN_x (with $x > 1$) which can co-exist with the stoechiometric ZrN, metallike
- metastable phases Zr_3N_4, insulator, and even ZrN_2 if the N_2 pressure or flow are very high, for example during reactive magnetron sputtering or microwave electron cyclotron resonance (MW-ECR) [FRA08, ZHI06].

The Zr_3N_4 phase is here reported to have a lower hardness, i.e. being softer than ZrN by microhardness measurements, and mix of ZrN and Zr_3N_4 a higher hardness of the single phases [ZHI06]. At very high N_2 flows (N/Zr ratio of the coating above 1.7) a soft amorphous phase forms.

Zirconium reaches its maximal valence in Zr_3N_4, and can also be produced by ammonolyse of $ZrCl_4$ [LER96]. It is isostructural with Eu_3O_4 and here crystallises in orthorhombic form following the Pnam space group (a = 9.7294 Å, b = 10.8175 Å und b = 3.0342 Å [BAU96]).

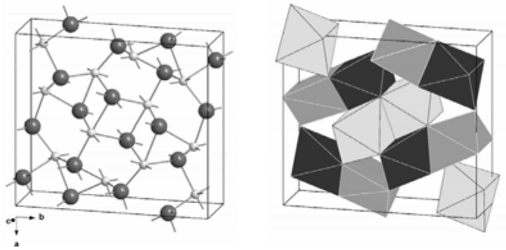

Figure 2.25: Crystal structure of orthorhombic zirconium(IV) nitride, o-Zr_3N_4 (space group Pnam , No. 62): (a) unit cell with Zr- and N-atoms represented by grey and black spheres, respectively; (b) the polyhedral structure plot showing the interconnection of ZrN6-polyhedra [DZI09]

In Zr-based coatings, the Zr_3N_4 structure can be described as a relaxed NaCl structure with some Zr vacancies according to [SCH85] or also as an orthorhombic phase. The same authors also suggest some metastable structures with coordinations of four, five or six for the nitrogen atoms. The structure of Zr_3N_4 varies with the incorporation of nitrogen in the solid. (This metastable phase has been reported for hafnium but not for titanium).

However a new form of Zr_3N_4 was recently produced. In 2005 Chhowalla [CHH05] reported the synthesis of Zr_3N_4 coating using the FCA (filtered cathodic arc) deposition method which is stabilized in cubic phase by residual compressive stresses above 9 GPa. The XRD peak positions of this cubic- Zr_3N_4 film are compared with the results obtained by Zerr

[ZER03] for a cubic Zr_3N_4 synthesized by mixing Zr and ZrN powders and crystallizing in the space group I-43d (a = 6.740 Å) with thorium phosphide (Th_3P_4) structure. They match with some of the values calculated on the base of the space group I-43d with a lattice parameter of 6.740 Å. The c-Zr_3N_4 films are harder than cubic ZrN films under nanoindentation with a maximum applied load of 5 mN (ca. 36 GPa vs. ca. 27 GPa) [DZI07].

It is often mentioned that the N/Zr ratio of the coating increases with the N_2 pressure or flow, and thus for different deposition techniques. Therefore the coatings based on Zr and N present a high variety of structures (*Fig. 2.26*) and properties steered by the method and parameters used for their production.

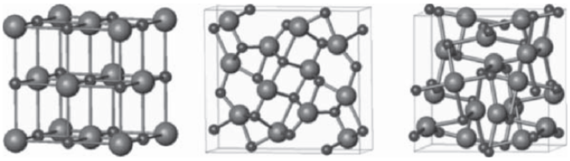

Figure 2.26: Crystal structures of ZrN based on the rock salt NaCl structure (left), orthorhombic Zr_3N_4 based on the space group Pnam (middle) and the cubic Zr_3N_4 structure based on the I43d space group (right) [CHH05].

2.10.4 ZrCN

Carbonitrides of the IVb metals are interesting materials for a number of technological applications, e.g. as wear-resistant materials in cutting operations. They are used as powders for starting materials to produce sintered hard materials or as layers for wear resistant and decorative coatings such as nitrides. There have been a lot of research reports discussing binary nitrides of IVb metals including ZrN. However, knowledge on ZrCN is still limited, the experimental information on the phase equilibria in the ternary carbonitride systems is restricted mainly to the quasi-binary MeC-MeN systems where complete miscibilities were observed.

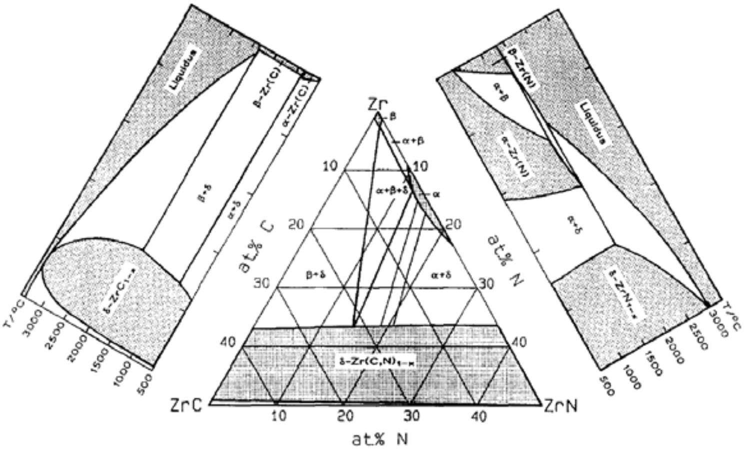

Figure 2.27: Tentative phase diagram of the Zr-C-N system at 1150 °C established by Binder, Lengauer and Ettmayer [BIN95] together with boundary systems [MAS91].

The Zr-C-N ternary phase diagram established by Binder, Lengauer and Ettmayer at 1150°C is given in *Figure 2.27*. The phase equilibria at 1150°C in the solid regions of the systems Ti-C-N, Zr-C-N and Hf-C-N were investigated by means of arc-melted as well as hot-pressed alloys. As previously shown, the binary carbide system Zr-C is characterized by an intermediate phase with the B1-type structure (i.e. NaCl) and here mentioned as δ-phase. The binary nitride system Zr-N features also a so called FCC δ-phase. Mentioned in [LIU09] and [MOR02], the lattice parameters in the ZrN-ZrC quasi-binary system were found to obey Vegard's rule, i.e. they follow a linear relation with the concentrations of the constituent elements.

Moreover, Agte and Moers observed in 1931 that the high temperature sintering of ZrC should be undertaken under high purity argon, i.e. almost free of nitrogen, as zirconium carbide was found to be very sensitive to nitrogen at high temperatures. Then ZrN is preferentially formed or nitrogen tends to mix easily with ZrC. Then at high carbon and nitrogen content, a δ-phase is also found in the Zr-C-N ternary system.

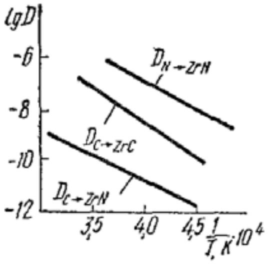

Figure 2.28: Effect of temperature on coefficients of diffusion of nitrogen in zirconium nitride and of carbon in zirconium carbide and zirconium nitride [AND81]

Diffusion of C and N in ZrN and C in ZrC are very slow in Zr. In *Figure 2.28*, at high temperatures ($1/T \cdot 10^4 = 4.5$ is equal to T = 1950°C, for T = 400°C, $1/T \cdot 10^4 = 14.9$) the coefficient of diffusion of nitrogen was found to be 10,000 times higher than C in ZrN. However in [ROS68] it was reported nitrogen diffusion in zirconium nitride at the temperature range 700–900°C. Carbon in ZrN can hardly migrate engendering a stable solid solution of the δ-phase. The self-diffusion of zirconium in zirconium nitride is registered above 2400°C [MAT99] (from [CUN06]).

ZrCN coatings may find different applications from medical tools for minimally invasive surgery [HOL01] to manufacturing tools or also for optical or diffusion barrier purposes [CHE05]. Its attractive colour combined with high corrosion resistance makes it suitable also for decorative protection in aqueous environment [GU06]. Concerning the deposition of ZrCN coatings, different methods are used, like PVD-arc deposition [KAO07], MOCVD [ALL00] or PACVD using radio frequency and pulsed-DC Plasma [WOH00].

W.H. Kao worked in Taiwan at the end of the 90's on TiN and TiCN coatings grown by PVD-arc deposition and tested under sliding conditions for machining purposes and switched his researches towards Zr-based coatings mostly deposited by unbalanced magnetron sputtering [KAO07,08]. ZrCN coatings were found to exhibit better wear and friction properties than arc-deposited TiN coating, but no correlation between deposition parameters, microstructure and properties could be highlighted [YAO05]. Carbon coatings containing Zr were successfully tested on WC-Co drills, with the best performances in drilling and turning of printed circuit boards (PCB) for the a-C:Zr45% columnar coating although it was not convincing under sliding testing. Recently he tested Zr–C:H:Nx% coatings with nitrogen contents varying from 0 to 25 at.% and produced by unbalanced magnetron sputtering too. Here the nitrogen-rich coatings displayed a better tribological behaviour under high speed micro-drilling tests on PCB (Printed Circuit Board), the nitrogen enrichment of the coating showing positive influences on the wear resistance and lifetime.

Allenbach and Morstein synthesized ZrCN coatings at 400-600°C by means of MOCVD (Metal-organic chemical vapour deposition) with the following precursors [ALL00]:

- $Zr(NEtMe)_4$ (TEMAZ, tetrakis(diethylamido)zirconium),
- $Zr(pyrr)_4$ (TPyrrZ, tetrakis(pyrrolidido)zirconium),
- $Zr(pip)_4$ (TPZ, tetrakis(piperidido)zirconium),
- and the binuclear complex $Zr_2(\mu\text{-N}^t\text{Bu})_2(\text{NH}^t\text{Bu})_4$, (TBUZ, bis(μ-tertbutylimido)tetrakis(tert-butylamido)dizirconium),

These metal dialkylamides precursors, also used to form Zr_xN_y powders, had the advantages over halides based ones of showing higher volatility and better dissociation at lower temperatures. Moreover, thanks to these molecules they tried to develop the deposition of metal carbonitrides without using additional external carbon source alike gas (for example, methane). A large panel of chemical compositions (with different Zr, C, N and O contents) was created depending on deposition parameters. The tribological behaviour in dry-sliding conditions of the MOCVD-deposited ZrCN coatings shows advantages over Ti-based (TiN, TiCN, and TiAlCN) and ZrN commercial coatings regarding friction but concerning wear, it was higher.

During carbothermal nitridation of monoclinic zirconia ZrO_2 above 1400°C, the formation of rock-salt-type Zr(N,O,C) phases was observed [LER96, LER97]. Rock salt like type Zr(N,O) phase was also produced by mixing ZrO_2 and ZrN powders and heating them at 1600°C under N_2 and H_2 atmosphere. A quadrupled cell dimension of the rock salt-type ZrN was found in ZrO_2-ZrN system. This fcc phase coexists with $Zr_7O_{11}N_2$, ZrN, and ZrO_2 in the ZrO_2-ZrN system with ZrN fraction ranging from 30 to 90 mole%. It is supposed to substitute a small amount of nitrogen atoms with oxygen atoms in the ZrN host lattice in an ordered form [IKE88]. Therefore near γ (Zr_2ON_2, cubic, a = 10.135 Å), β ($Zr_7O_8N_4$, rhombohedral, a = 9.540 Å, c = 8.834 Å), and β' ($Zr_7O_{11}N_2$, rhombohedral, a = 9.560 Å, c = 17.60 Å). In zirconium oxy(carbo)nitride coatings, with increasing nitrogen content in the films, the ZrO_xN_y structure changes from monoclinic ZrO_2 to orthorhombic ZrO_2, then to the partially amorphous zirconium oxynitride phase and finally to the cubic ZrN phase. In ZrO_xN_y it also may exist the rock-salt like structure, where oxygen and carbon at low amounts substitute nitrogen atoms or are interstitial atoms in ZrN crystal implying a lattice distortion and formation nonuniform microstress [CUN06]. The possibility of the formation of poorly crystallized oxygen-doped orthorhombic, Zr_3N_4-type structures in such coatings is evocated by different authors [CAV05]. The presence of oxygen in deposition chamber is often reflected by the systematic decrease in the deposition rate, which can be explained by the target poisoning by both reactive gases [VAZ04] or possible interfering of oxygen with the mobility of the adatom species [CAV06].

3 Experimental details

3.1 Materials

In order to apply the coatings and to study their slip-rolling resistance, the high-nitrogen steel Cronidur 30 (X30 CrMoN 15 1, equivalent to DIN 1.4108 and AMS 5898) was chosen as substrate material. This steel was developed at the end of the 80’s with high corrosion resistance (almost Ni free) and tenacity [GEN99]. It finds applications in aircrafts for conception of fuel pumps or for the realisation of servo drives for air brakes/deflector or landing flaps. Bearings of the main output shaft in aero-engines are made in Cronidur 30 too. It is on the way to be validate by ESA as standard material for bearings in space application because of its better performances in high temperature bearings (up to 500°C, the Cronidur 30 keeps its characteristics, in comparison to the more traditional 440C, which looses its main characteristics at temperature above 250°C). The Cronidur 30 is also used for rams in water cooled turbodrills and screws.

This choice of substrate material was motivated by two reasons: first of all the steel is produced by means of pressurized electroslag remelting, (PESR, DESU, Druck-Elektro-Schlacke-Umschmelzverfahren) which in a same manner as VIM-VAR method (Vacuum Induction Melting - Vacuum Arc Remelting) ensures a high quality of substrate material, i.e. without (centreline) segregation or porosity and defects due to production process. This is important in the way that failure of the substrate must be avoided to study the slip-resistance of the coating itself. Secondly, contrary to the traditional bearing steel 100Cr6H (equivalent to AISI 52100), the hardened and tempered Cronidur 30 can withstand high temperatures without loss of hardness. Its hardness decreases after 500°C as shown in *Figure 3.1* which makes it suitable for deposition processes at such ranges of temperature.

The composition of the nitrogen alloyed steel Cronidur 30 is presented in the *table 3.1* and the measured values by means of WDX on a sample.

Table 3.1: Chemical composition of the Cronidur 30 steel (wt. -%).

Element	C	N	Cr	Mo	Si	Ni	Mn
Wt. -% min - max	0.25 – 0.35	0.30 – 0.50	14.00 – 16.00	0.85 – 1.10	0 – 1.00	0 – 0.50	0 - 1.00
WDX Wt. -%	0.38	0.38	15.57	1.00	0.62	0.12	0.24

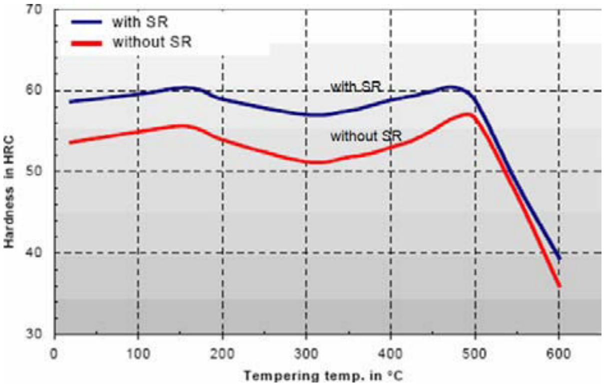

Figure 3.1: Tempering chart of steel Cronidur 30 hardened at 1,030°C during 1h and quenched in oil. tempering: 2 x 2h / air (SR: Subzero Refrigeration). 500°C is the maximal temperature acceptable to maintain bulk hardness. Evolution of hardness for Cronidur 30 with the temperature [ENE03]

The substrates were firstly machined from a steel rod to give them their basic form, and then heat treated. The heat treatment (*Fig. 3.2*) was carried out following a sequence of:

- austenitization (above 800°C) under vacuum (P ~ 2.10^{-3} mbar) in three temperature steps during several hours, until a final temperature of 1,030°C for 30 min,
- followed by a martensite hardening by N_2 quenching with a subzero cooling at -80°C to remove the retained austenite (as M_f is under the ambient temperature)
- and two tempering treatments at 475°C of 1hour under neutral atmosphere (N_2) … .

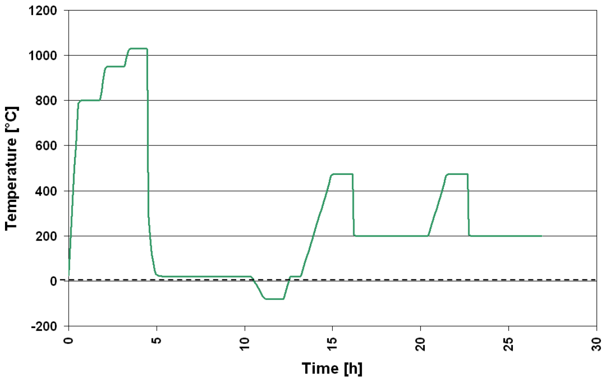

Figure 3.2: Schematic heat treatment curve of the Cronidur 30 substrates.

The final substrate hardness reaches 59 HRC after heat treatment and their elastic limit (yield strength, offset yield point at 0.2% plastic strain) $R_{p0,2}$ has a value above 2,300 MPa (in Four Point Bending Test). The amount of residual austenite must be as low as possible, as it is metastable at room temperature and it loses its metastability under repeated cyclic loading.

After being trough hardened, the cylindrical and spherical samples have been finally finish-grinded to their final dimensions. The spherical discs were honed until reaching a roughness of $R_a = 0.6$ µm with machining scores oriented along the circumference (i.e. with an isotropic topography) and the cylinders were mirror polished on their outer cylindrical surface until roughness values of $R_a < 0.010$ µm and $R_z < 0.050$ µm.

In order to protect their mirror polished surfaces after machining, a multifunction spray based on isopropanol and aliphatic oil was used (Technolit WL-50). The isopropanol ensures a good spreading of the protective oil film and at the same time a good removal of it by using isopropanol as cleaning agent and solvent in ultrasonic bath prior to shipment and deposition. As additional preventive action, the substrates were finally stored in exsiccator in order to prevent them from any water condensation.

3.2 Deposition of the coating for slip-rolling tests

The Zr(C,N) coatings were all made at Tekniker Technological Center (Eibar, Spain) in an industrial coating installation by Cathodic Arc Plasma Deposition. This method is a combination of two deposition techniques, the arc evaporation and the plasma ion platting. Prior to the deposition a pre vacuum is made at $7{\cdot}10^{-5}$ torr. The substrates act as anode and the Zr-target as cathode. After the activation of the arc on the whole surface of the cathode, the evaporation of the target takes place. The evaporated material migrates through traverses the plasma of argon and is ionisated. It reacts then with the reaction gas made of nitrogen N_2 (and acetylene C_2H_2) to form the material to be coated, i.e. ZrN and Zr(C,N). By applying a negative polarization on the substrate, the so called bias, the ionised material is finally deposited on the substrates.

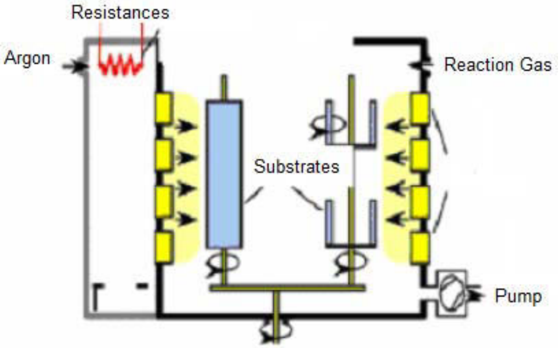

Figure 3.3: Scheme of the arc evaporation assisted by plasma system [ESP05]

The cathodes and the anodes are situated in the reactor or deposition chamber (*Fig. 3.3* and *3.4*). The substrates are mounted on a planetary system which keeps them in a continuous rotation during the process and a system of resistances ensures the heating of the chamber. The deposition sequence of the Zr(C,N) consists in three phases of gas mixtures: primary only Argon is added in the reactor, then it is mixed with Nitrogen and finally Acetylene is added at the final step (*Tab. 3.2*). Therefore the coating consists theorically in a layer with a rich Zr-content on the substrates, acting as a very thin adhesion layer, this one being then overcoated with a ZrN layer and a final Zr(C,N) layer.

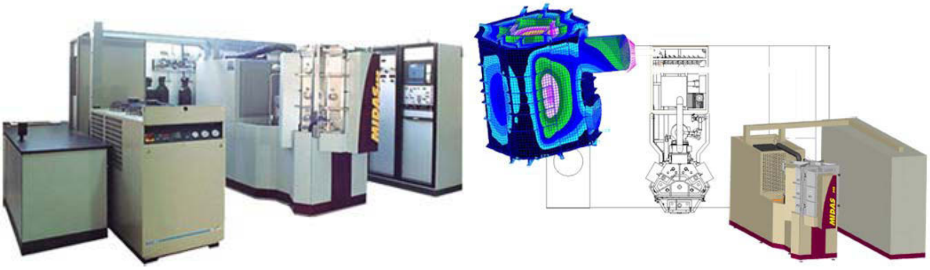

Figure 3.4: MIDAS 450 from Tekniker

Table 3.2: deposition sequence for the automated deposition

Location	Outside	Deposition Chamber					
Phase	*Preparation*				Deposition		
Step	*Cleaning + clearing*	*Heating*	*GD cleaning*	*Evacuation*	Zr "interlayer"	Nitrogen	Acetylene
Time		*120 min*	*20 min*		3 min	90 min	
Temperature		*300°C*					
Pressure		*< 0.1 mtorr*		*< 0.1 mtorr*	3.5 mtorr	8 mtorr	
Substrate polarization					600 V	30 V	30 V
Current					150 A ?	150 A (magnetically steered arc)	
Gases			*$Ar + H_2$*	*-*	Ar	N_2	$N_2 + C_2H_2$

3.3 Slip-rolling experiments

3.3.1 Contact configuration, choice of the contact geometry

The cylindrical steel discs, after being super polished and coated, are tested under slip rolling motion at low speeds and under high starting Hertzian stresses. To apply the high Hertzian stresses, an uncoated spherical disc made of steel is chosen as counterbody to create a configuration “coating on cylindrical super polished steel / uncoated spherical steel with rougher surface”. The choice of a spherical steel disc as counterbody is motivated by the possibility of applying higher starting Hertzian stresses than with a more traditional “cylindrical vs. cylindrical” configuration (see *Table 3.3*). With the spherical geometry it is possible to reach an average starting Hertzian pressure of P_{0mean}= 1.94 GPa (P_{0max} = 2.91 GPa) by using a normal force of 2,000 N (limit of the maximal normal force of the tribometer). In the “cylinder on cylinder” configuration such a normal force would only induce an average starting Hertzian pressure of P_{0mean} = 660 MPa. Indeed the maximum and average contact pressures have a higher dependence on the applied normal force (*Tab. 3.3*) in the “cylinder vs. cylinder” configuration but the contact surface is in the same time larger because it depends also on the sample geometries. Furthermore aligning errors and geometry errors with a spherical counterbody are of lesser importance in comparison of a cylinder-cylinder configuration. Misalignment, which may be responsible for edge effects and then very high and concentrated stresses, is simply banned.

Spherical disc / Cylindrical disc	Cylindrical disc / Cylinder disc (axially parallel)	
$P_{max} = \frac{3 \cdot F_N}{2 \cdot \pi \cdot a \cdot b}$ $a,b \propto \sqrt[3]{F_N}$ $P_{max} \propto \sqrt[3]{F_N}$	$P_{max} = \frac{4 \cdot F_N}{2 \cdot \pi \cdot L \cdot b}$ $b \propto \sqrt{F_N}$ $P_{max} \propto \sqrt{F_N}$	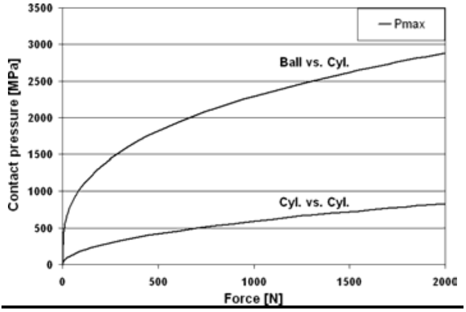

Table 3.3: Dependence of the maximal Hertzian pressure for “sphere on cylinder” and “cylinder on cylinder” configurations and comparison of the evolution of P_{max} with the applied normal force

The counterbody remains uncoated for two main reasons. First of all, the perfect polishing (prior to any coating deposition) of spherical surfaces is harder than that of cylindrical surfaces. And secondly, it is favourable to use an uncoated counterface because the starting roughness, crucial in determining the lubrication domain, is controllable. A third reason, is cost effectiveness, for latter applications self-matted surfaces engender higher manufacturing prices. The counterbody material was made in steel, Cronidur 30 (like the substrate for the coatings) or 100Cr6H (AISI 52100). These steels are typically used as bearing steel since they are very hard and wear resistant. This choice was governed by the possibility of conserving as long as possible the initial contact geometry (and then the initial average Hertzian pressure). Wear increases the radius of the counterbody which induces a loss of Hertzian contact pressure, while keeping steel as counterbody base material.

Table 3.4: Maximal, mean contact pressure, and maximum shear stress with its depth position following the Hertz theory for the contact configuration used. The whole deformation δ is also shown.

$R_{x1} = R_{x2} = R_{y1} = 21$ mm		E=208 GPa				
$R_{y2} = \infty$		$\nu = 0.3$			z = 0.59 b	
P_{mean} (GPa)	F_N (N)	P_{max} (GPa)	b (mm)	τ_{max} (GPa)	z (µm)	δ (µm)
1.00	287	1.50	0.239	0.50	-141	6.1
1.25	561	1.88	0.298	0.63	-176	9.6
1.50	970	2.25	0.358	0.75	-211	13.8
1.75	1540	2.63	0.418	0.88	-247	18.8
2.00	2300	3.00	0.477	1.00	-281	24.5
2.25	3274	3.38	0.537	1.13	-317	31.0
2.50	4492	3.75	0.597	1.25	-352	38.1

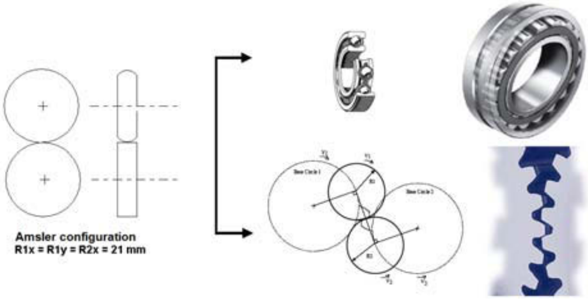

Figure 3.5: Interest of using a two disc machine for simulation of conformal contacts subjected to rolling motion

3.3.2 Amsler tribometer

The tribometer used for the slip-rolling experiment is an Amsler-type machine [NN22], used in the 70’s for wheel-rail contact research purposes. It is well adapted for slip-rolling experiments in mixed boundary lubrication because of the low driving speeds of the samples. Effectively, the discs speed is limited at 390 rpm which enable the mixed/boundary lubrication regime, higher speeds engendering the so-called EHD regime. In order to establish the mixed/boundary regime, the rotation speeds must be in accordance with the chosen counterface roughness. Moreover, this testing machine can reproduce the working conditions and contact configuration for contacting gear teeth and ball bearings (ball on a cylinder) and can be use for simulation aims (*Fig. 3.5*).

The slip amount between the two rolling discs is controlled and continuously maintained at 10%. The construction of the machine with a single electric motor does not permit the variation of the slip. The speed of the upper axis is slaved to the lower axis through mechanical construction and the use of gears coupling the upper axis to the lower axis.

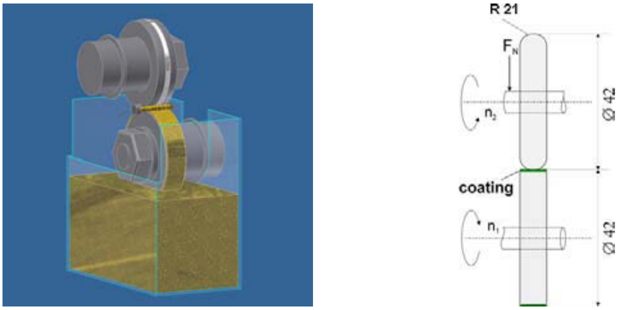

Figure 3.6: Testing arrangement

A normal force is applied to create the Hertzian stresses. A spring maintained in compression with a stiffness of 14,650 N/m serves to stress the discs against each other.

With the lever action by hinging down the counterbody holder and the release of the spring, forces can be applied up to 2,000 N in the contact point (*Tab. 3.5*). The force is adjusted by controlling the initial compression of the spring, the resulting force being read on a scale (step of 50 N). After release of the spring a more precise adjustment can be made by applying an additional traction force on the spring. The two discs are in rolling/sliding contact against each other under controlled load. The lower disc is partly submerged in oil. Its rotation drags the lubricant also into the contact (*Fig. 3.6*).

The friction torque is caused by the friction acting in the contact and is measured during the tests by the axial torque of the lower shaft using a pendulum as well as a planetary gearing coupled with the lower sample axis. The friction coefficient μ (or also COF, Coefficient Of Friction) follows the equation:

$$\mu = M/(F_N \cdot r) \tag{3.1}$$

with M Friction torque in N.m, F_N applied normal force in N and r radius of the lower driven sample in m. The inclination of this pendulum is translated into a translation movement for the measurement of the corresponding torque on a scale. Coupling a LVDT permits the transduction of this translation into an electric signal, and thanks to calibration, the friction coefficient can be directly recorded. Before each test, the equilibrium point is determined by mounting the samples and letting them roll without bringing them into contact. This permits a preheating of the mechanical parts ensuring a stable measure and avoiding a “thermal drift” which would imply an overestimation of friction.

Table 3.5: Summary of the testing parameters used

Conditions	Parameters
Dimensions of the discs	Diameter : 42 mm; Width : 10 mm
Contact	Grinded spherical disc (radius of curvature: 21 mm) against coated cylindrical disc.
Substrate	Cronidur 30
Type of motion	Rolling with a 10% slip rate
Initial average Hertzian pressure P_M	1.5 –1.75 – 1.94 GPa (F_N = 935 N – 1,480 N – 2,000 N)
Rotation speed	390 rpm (coated disc) – 354 rpm (spherical disc)
Sliding speed v_{diff}	0.08 m/s
Cycles n_{tot}	Until 10^7 or rupture (flaked surface of 1 mm^2)
Sliding distance / Rolling distance	Until 132 km / until 1,320 km
Surrounding temperature	Ambient Temperature (≈22°C), 120°C
Lubricants	Paraffinic oil Factory fill engine oil FF 0W-30

The temperature of the oil bath for the tests at 120°C is simultaneously recorded with a type K thermocouple dipped a few millimetres under the surface of the oil. For security reason the thermal sensor is coupled with a programmable relay, taking the temperature down if it exceeds 140°C. After each test, the oil recipient as well as the axles are cleaned to eliminate wear particles and rinsed with isopropanol, to eliminate residues of lubricant. Before each test, both discs are cleaned in ultrasonic bath with isopropanol

3.3.3 Lubricant properties

Two lubricants were used for the slip-rolling tests (*Tab. 3.6*). First of all, an unadditivated paraffin oil ISO VG 46 was taken as lubricant for testing at room temperature with the aim of avoiding any effect due to EP/AW (Extreme Pressure / Anti Wear) additives contained in fully formulated oils. This is advantageous to evaluate the ability of the coating in replacing toxic additives.

As previously mentioned and shown by the expression of the minimal film thickness in Eq. 2.11, the two easiest possibilities to increase the severity of the contact, i.e. to reduce the specific film thickness are the reduction of the speed or the diminution of the viscosity and/or of the piezo-viscosity. A reduction of the speed would dramatically extend the testing time, therefore the increase of the temperature emerges as a better alternative. However without adapted additives, paraffin oil cannot be heated (for a long time) to increase the severity of the contact by diminishing the oil film thickness because of oxidation phenomenon or evaporation (NOACK volatility). Therefore a second oil, a factory fill motor oil i.e. with a low content of additives, was selected to carry out tests at 120°C, a temperature more representative of today's lubricated applications. Certainly the additives play a role and partly counterbalance the severity augmentation but their content remains low and it offers a possibility to observe any positive interaction with the coating, a reacting coating offering advantages for latter applications and better chances for a relative fast industrial mutation towards low SAP or "bio" (more ecological) lubricants.

Table 3.6: Viscosimetric properties of the paraffin oil ISO VG46 and factory filled oil SAE 0W-30 [SCH06]

Properties	Unadditivated paraffinic oil	Factory fill BMW SAE 0W-30 motor oil
VI	100	168
Pour Point [°C]	-6	-57
$\eta_{40°C}$ [mPa.s]	44.2	57
$\eta_{100°C}$ [mPa.s]	6.01	8.04
$\nu_{100°C}$ [mm²/s]	7.4	10.2
$\eta_{150°C}$ [mPa.s]	3.06	3.34
$\nu_{150°C}$ [mm²/s]	2.4	4.42
HTHS [mPa.s]	2.13	2.98
α_p [GPa^{-1}]	20.7 @ 40°C	14.17 @ 80°C
	12.6 @ 150°C	11.9 @ 150°C

3.3.4 Assessment of the lubrication regimes in the slip-rolling tests

As shown in part 2.6, the lubrication regime can be described by the lambda ratio. The equation 2.11 can be used to evaluate the specific minimal film thickness and in turn the operating lubrication modus. According to this expression, it is obvious that a load increase has almost no direct effect contrary to the speed and the piezo-viscosity. (Note: the load acts on the properties of the lubricant). It reflects the fact that the EHD regime is mostly governed by the lubricant.

To illustrate, this expression involves that:

- an elevation of a factor 10 of the speed parameter multiplies it by 4.8, a reduction of a factor 10 implies a decrease of it by a factor 0.2;
- an elevation of a factor 10 of the coefficient of piezo-viscosity α multiplies the materials parameter G by 3.1, a reduction of a factor 10 implies a decrease of it by a factor 0.3. However α is not subjected to such variations in practice.
- an elevation of a factor 10 of the force implies a multiplication by 0.84 of the load parameter W (with the hypothesis of an unchanged viscosity and piezo-coefficient). At high loads, a load augmentation does not basically modify the film thickness but the deformations of the contacting materials are greater.

Therefore the speed parameter appears to be the most influencing parameter on the minimal film thickness, and the easiest to tune. This supports the fact of constant developments in lubricants technology, as they have the most powerful effect to control the lubrication regime in mechanical design.

In the light of testing purposes, to act on the lubricant film thickness taking place in the slip-rolling tests, the most effective testing parameters and the easiest ones to handle are the speed or the viscosity. Speed is mostly fixed by the testing machine or the application requests and the rotation speed must permit to achieve a reasonable number of revolutions in a reasonable testing time. Then viscosity remains the only “screwable” system variable. To “force” the tribosystem to work under severer mixed/boundary lubrication, besides controlling the roughness of the facing samples (which is only achievable at the beginning of the test), the rise of temperature, which modifies the dynamic viscosity of the lubricant, occurs as the best method. Moreover some liquid lubricated mechanical applications do work at temperatures higher than the room temperature, making sense to carry out tests at a temperature above 100°C.

Table 3.7 summarizes the evaluated minimal lubricant film thicknesses for the paraffin oil at room temperature and the factory fill motor oil SAE 0W-30 at 120°C for the testing parameters chosen.

Table 3.7: Hertzian contact pressures for the substrate geometries tested and evaluated minimal lubricant film thicknesses

Force [N]	930	1,470	2,000
P_{mean} [GPa]	1.5	1.75	1.94
P_{max} [GPa]	2.25	2.63	2.91
Global deformation [µm]	13.4	17.8	21.2
h_{min} (Paraffin oil @ 40°C) [µm]	0.147	0.142	0.139
h_{min} (Motor oil @ 120°C) [µm]	0.027	0.026	0.025

Moreover the preparation of the spherical steel counterparts by honing respects the purpose of testing under severe lubricating conditions. The honing was done by rotation of the samples causing longitudinally oriented scores. The parameter γ describing the surface pattern of the roughness is then far greater than 1 (longitudinal orientation of the surface topography, see chapter 2). It favours the establishment and conservation of the boundary lubrication for the tests.

3.3.5 Failure criterion and test stop

The tests were run until failure of the coating (and only of the coating) or until 10 millions cycles (see *Tab. 3.5*). This upper limit for the duration of the tests corresponds to 18 days, if no damage occurred. The appearance of a surface damage with a continuous area of more than 1 mm² was defined as ‘critical’, leading to an immediate end of the test and the respective sample was considered to have failed after the number of cycles run. The coatings were still considered as slip-rolling resistant, if none of the damages reached an area larger than 1 mm², especially so, if the in-situ monitoring Acoustic Emission did not detect any fracture activities (crack propagation) under lubrication at RT. This failure criterion has so far proven to be easy to handle, quick and successful. In recent literature, however, the total removal of the coating is proposed as failure criterion for lubricated slip-rolling tests [LIU07, KUM07]. Since the aim of the coating is to protect the substrate as long as possible, this concept fails once the damaged surface area is bigger than the contact area. The area of 1 mm² chosen as critical in the present work is about the size of the Hertzian contact ellipse (1.142 mm x 0.712 mm) at an average pressure of $P_{mean} = 1.5$ GPa. Using the complete removal of the coating as failure criterion ignores the fact that the coated part is no longer protected. The uncoated counter body can already sustain some serious damages once the coating starts to give way. The functionality of the system/component can no longer be guaranteed. This 1 mm² criterion places higher demands on the coatings compared to the complete removal of the coating [KUM06] or the PCW [AMA05, MAR08] (percentage of coating worn) found in the literature or the detection of mechanical vibration with acceleration sensors.

4 Experimental results

Seven batches of coatings deposited on Cronidur 30 steel were delivered and are regrouped in *Table 4.1* with their particularity. Due to a somewhat higher roughness of the coatings compared to the coating of reference (i.e. from the first batch), slip-rolling tests were carried out with their as deposited state and after mechanical polishing of their surface. A variation was also done with a batch containing substrates as received from the coating manufacturer and fresh repolished ones just before deposition. All the samples were deposited on polished Cronidur 30 (*Fig. 4.2*).

Table 4.1: Summary of the tested Zr(C,N) coatings

Batch#	Sample #	Thickness	Particularity
1	LA0X	3.6 µm	Slip-rolling resistant coating, “reference”
2	LA12X	3.3 µm	Slip-rolling tests with as deposited coatings and some coatings mechanically polished
3	LA11X	2.6 µm	Slip-rolling tests with as deposited coatings and some coatings mechanically polished
4	LA10X	1.5 µm	Slip-rolling tests with as deposited coatings and some coatings mechanically polished
5	MC5X	2.8 µm	Trouble during deposition, instability of the arc. Some coatings mechanically polished
6	MC2X	2.8 µm	Slip-rolling tests with as deposited coatings and some coatings mechanically polished
7	MC8X	~ 3 µm	Slip-rolling tests with as deposited coatings and some coatings mechanically polished
	MC6X	~ 3 µm	Repolishing of the substrates prior deposition, Some coatings mechanically polished
8 & 9	MC12X	~ 3 µm	two batches of pcnl Zr(C,N) coating (process-controlled nanolayering)

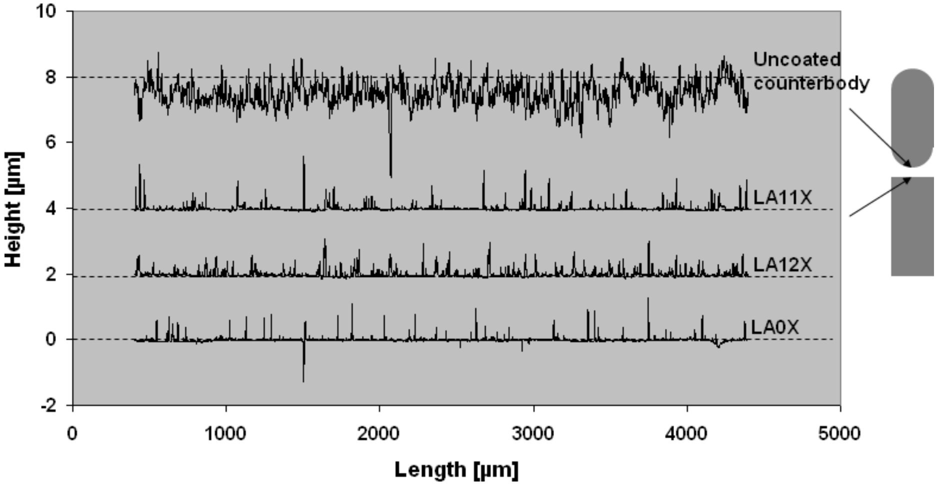

Figure 4.1: Examples of roughness’s profiles of some coatings obtained by profilometry (Hommel profilometer, peaks are droplets)

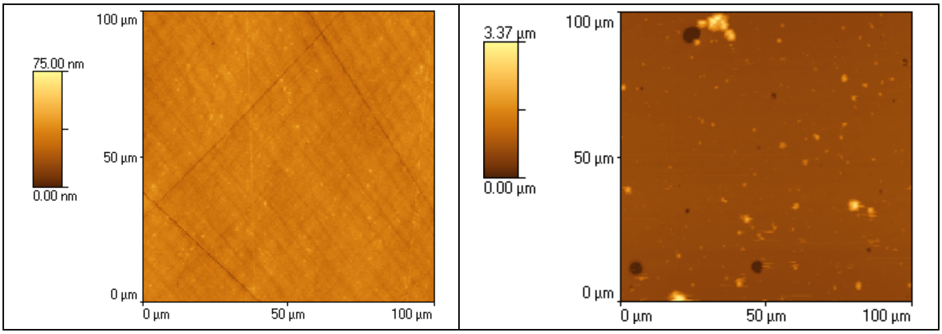

Figure 4.2: Surface topography of uncoated, polished Cronidur 30 (left) and of a Zr(C,N) coating after deposition

Due to variations of colours after deposition, Zr(C,N) coatings on discs were characterized by means of colorimetry (CIE 1976 L*, a*, b* colour space). The three coordinates build a three-dimensional model in which L*, a* and b* represent respectively the lightness, the position between red/magenta and green and the position between yellow and blue. *Figure 4.3* compiles the L*a*b* values measured for the different coatings. The thickness of the coatings is not correlated with the colorimetry values (samples LA126, LA114, LA104). Therefore it is supposed that only the surface causes colour variations which would be generated by the adjunct of acetylene during the last step of the deposition process.

a) **Optical images of Zr(C,N) coatings**

1st batch	2nd	3rd	4th	5th	6th
3.6 µm LAX	3.31 µm LA12X	2.6 µm LA11X	1.5 µm LA10X	2.8 µm MC2X	2.8 µm MC5X

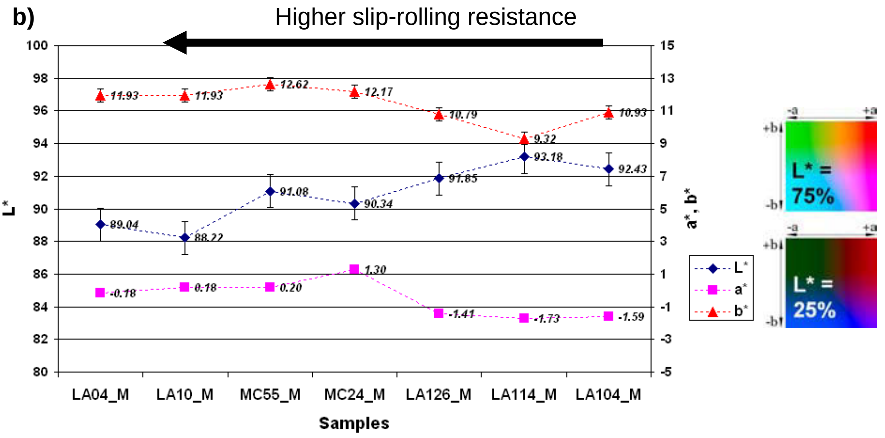

Figure 4.3: a) optical images and b) L, a* and b* values of the investigated samples extracted from their respective reflectance curve.*

4.1 Slip-rolling tests

4.1.1 Reference uncoated steel vs. uncoated steel

In order to investigate the benefit of applying a coating on the cylindrical part, reference tests were carried out. Reference tests should be understood as configuration “uncoated steel vs. uncoated steel” under standard testing conditions, i.e. a starting Hertzian pressure of P_{0mean} = 1.5 GPa in the unadditivated paraffin oil at room temperature and in the factory filled (FF) motor oil 0W-30 at 120°C. Namely the design of the standard testing conditions used for the reference tests corresponds to the less demanding functional requirements to be achieved by the coating. The cylindrical part is mirror polished and the grinded counterbody shows the same roughness and surface state as for tribological tests with the coatings.

P_{0mean} = 1.5 GPa Unadditivated paraffin oil, R.T. 10,000,000 cycles	P_{0mean} = 1.5 GPa Unadditivated paraffin oil, R.T. 10,000,000 cycles	P_{0mean} = 1.5 GPa FF SAE 0W-30, T = 120°C 10,000,000 cycles
 Cylindrical uncoated disc (SAE 52100)	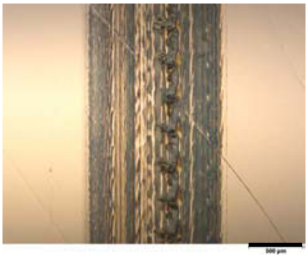 Cylindrical uncoated disc (Cronidur 30)	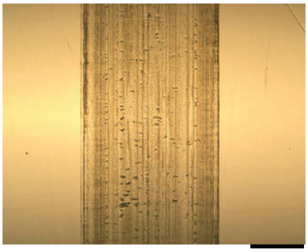 Cylindrical uncoated disc (Cronidur 30)
 Spherical uncoated Counter body (SAE 52100)	 Spherical uncoated Counter body (Cronidur 30)	 Spherical uncoated Counter body (SAE 52100)

Figure 4.4: light microscopy photographs of typical wear tracks of steel/steel contacts displaying their morphology (scale: 500 µm for all the pictures)

Figure 4.4 recapitulates the typical morphologies of the wear track on the cylindrical part (top) and on its respective spherical uncoated counterbody (bottom). These morphologies are engendered after the upper testing time limit of 10 million cycles. Notwithstanding superfinishing is one of the most powerful technologies for significantly increasing the load carrying capacity in gears by retarding micropitting [WIN09], on these light microscopy pictures it is obvious that the polished cylindrical part suffers extremely from degradation. Cracks appear (on the left), scuffing and pitting (middle) and begin of micropitting (right) take place, characteristic damages of mechanical parts operating at high load and low speed and subjected to fatigue. Evidentially the motor oil avoids scuffing thanks to its additives separating the two contacting surfaces, but cannot prevent the formation of micro pitting and micro cracks due to contact fatigue. A magnification of the picture on the right is represented in *Figure 4.5* showing microcracks of about 20 to 100 µm formed, as usual, transversally to the rolling track and traces. In comparison, the spherical counterpart is otherwise relatively undamaged, only wear can be found in the track of the 100Cr6H counterbody. The Cronidur 30 counterbody undergoes some pitting in the middle of the track in paraffin oil.

In the tracks of the samples run in the motor oil, signs of a reaction layer can be observed locally, probably due to the repeated passage of the roughnesses of the counterbody causing brief local high stresses.

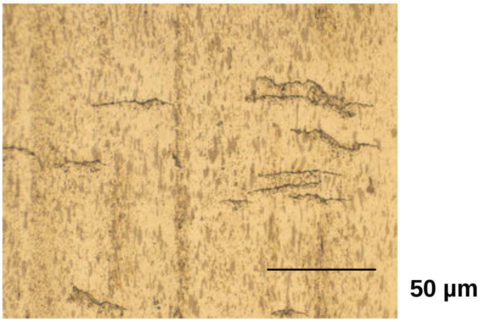

Figure 4.5: Magnification of the track in the cylindrical uncoated Cronidur 30 sample run in motor oil showing microcracks formation.

4.1.2 Tests with cylinders coated with Zr(C,N) coatings

To compare the results obtained, the diagram in *Figure 4.6* presents the performance of the different batches. Almost everything to describe the tribosytem is available.

The logarithmic y-axis mentions the number of cycles. In the figure, the lubricants are represented by colours, blue for paraffin at room temperature, pink for the factory filled SAE 0W-30 motor oil at 120°C. When the tested coating did not fail after 10 million rolling cycles, an arrow symbolizes the good performance, with the indication that it could longer sustain the tribological strain. In the grey boxes, top and bottom, are reported the kind of the steel counterpart and the kind of the substrate (the coatings were always deposited on super polished Cronidur 30 steel). The average starting Hertzian pressures P_{0mean} are indicated under the counterpart boxes. At the base of the bars representing the numbers of cycles reached, smaller bars represent the coefficient of friction at the beginning (left) and at the end of the tests (right one). The geometrical contact configuration is depicted at the left side of the figure with the speed parameters used.

At first view, an imbalance in the performance between the batch #1 and all the others is obvious. On the left side, the batch #1 is the most successful; all samples are slip-rolling resistant under all the conditions tested. These coatings will be mentioned as good or high performing in the rest of the text. This batch forms the core of the present work in order to figure out the cause of this occurring high difference.

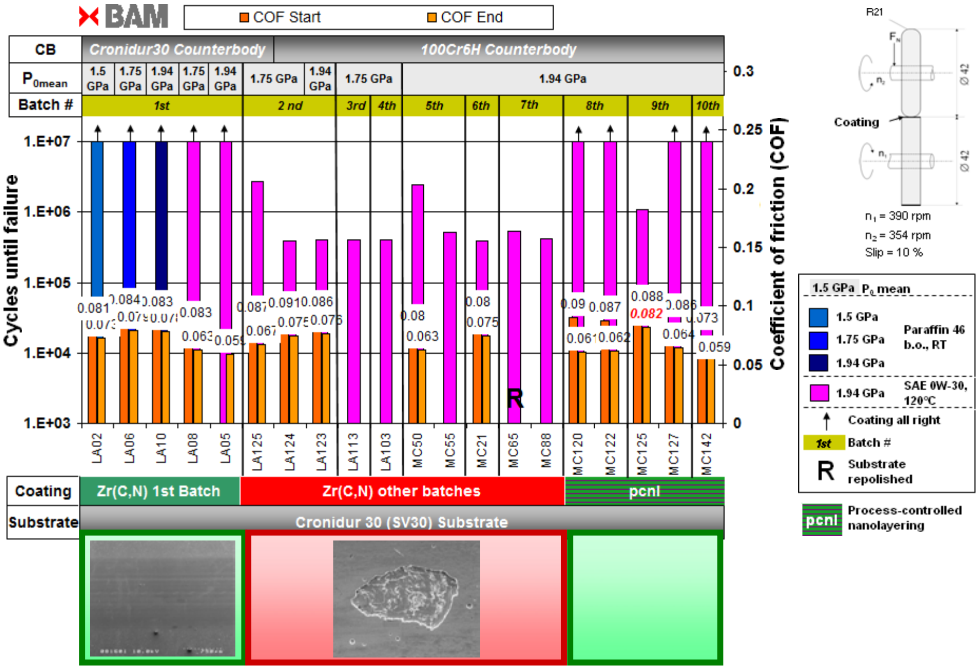

Figure 4.6: Diagram summarizing the slip-rolling results obtained with Zr(C,N) coatings.

In the case of the first batch, the topographical pictures of the surface of the coating and its respective uncoated counterbody are summed up in *Figure 4.7*. No damages or spalling on the coating are visible on this overview photographs and neither at higher magnitude. A defect on the coating tested at P_{0mean} = 1.94 GPa in paraffin oil is present but it was already there on the coating before testing (see *Fig. 4.8*). It implies the slip-rolling resistant coating with droplets was not sensible to presence of surface defects and the rolling contact resistance was not influenced (in the range of 10 millions cycles). This is an encouraging sign as it is almost impossible to obtain industrial "thick" PVD coatings on large surfaces without defects such as droplets (often produced during cathodic vacuum arc deposition) or holes, those being mostly responsible for a lowering of technical performances.

All the other coatings were flaked off mostly before reaching 500,000 cycles (example of topographical pictures in *Figure 4.9*). The poor slip-rolling coatings were much sensible to surface defects.

Very recently, following the microstructural characterisation performed (see part 4.5), three new batches were produced with small variations of a deposition parameter in order to promote the formation of a nanolayered structure with a controlled parameter (batches #8, 9 and 10, pcnl Zr(C,N) coating, pcnl: process-controlled nanolayering). These coatings perform as well as the high slip-rolling resistant Zr(C,N) coatings of the first batch and thus with a similar tribological behaviour (same friction and wear coefficients).

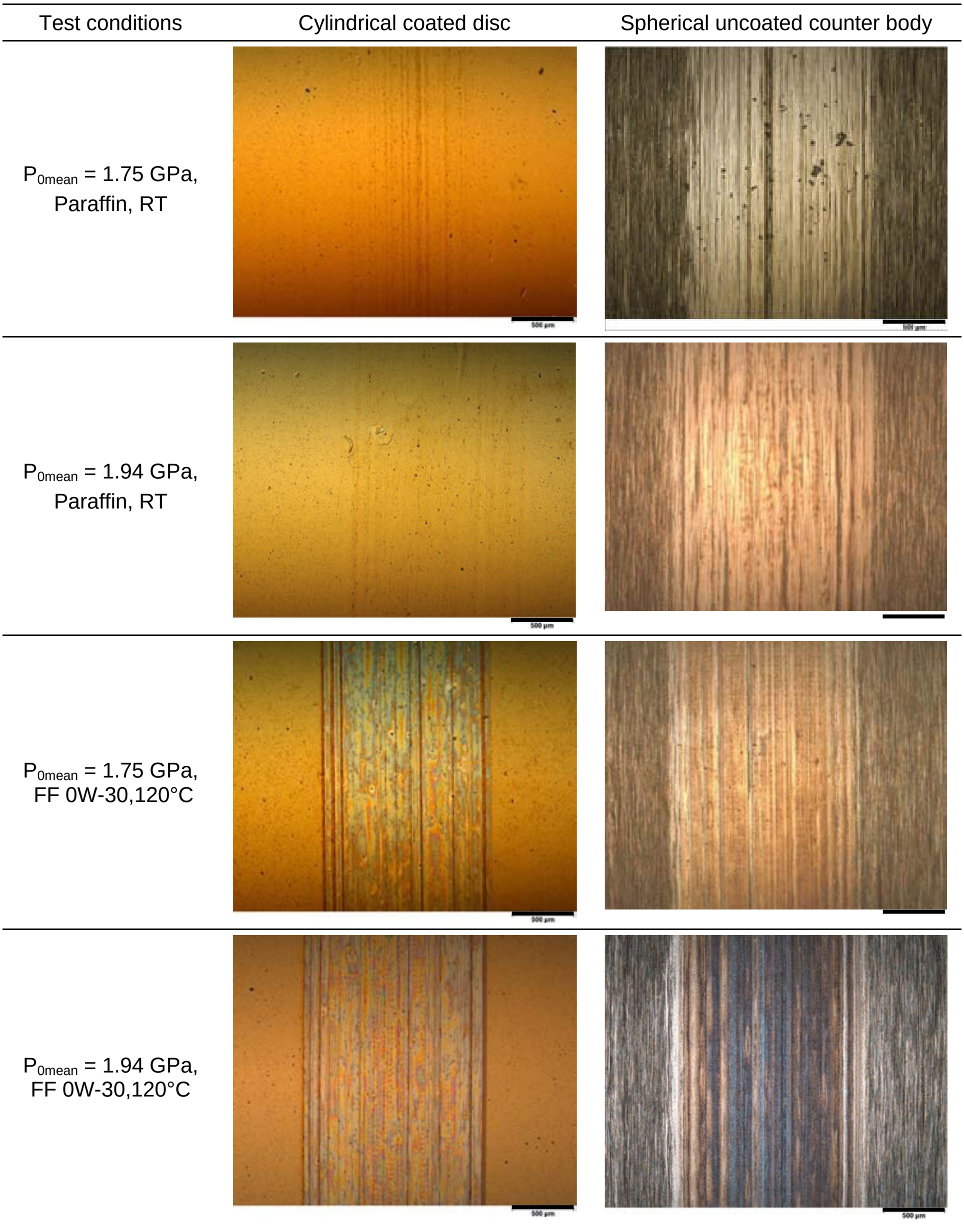

Figure 4.7 : Optical microscopy pictures of the counterbody and of the primary slip-rolling resistant coating (batch #1) after test in paraffinic oil at room temperature and in FF motor oil at 120°C (all at the same magnification, scale bar = 500 µm)

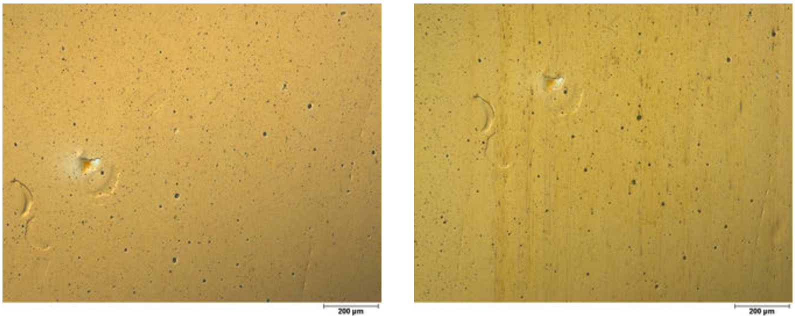

Figure 4.8: Same area with initial surface defect on the slip-rolling resistant coating (batch #1) before (left) and after (right) 10 millions cycles at P_{0mean} = 1.94 GPa, Paraffin, RT (scale bar = 200 µm)

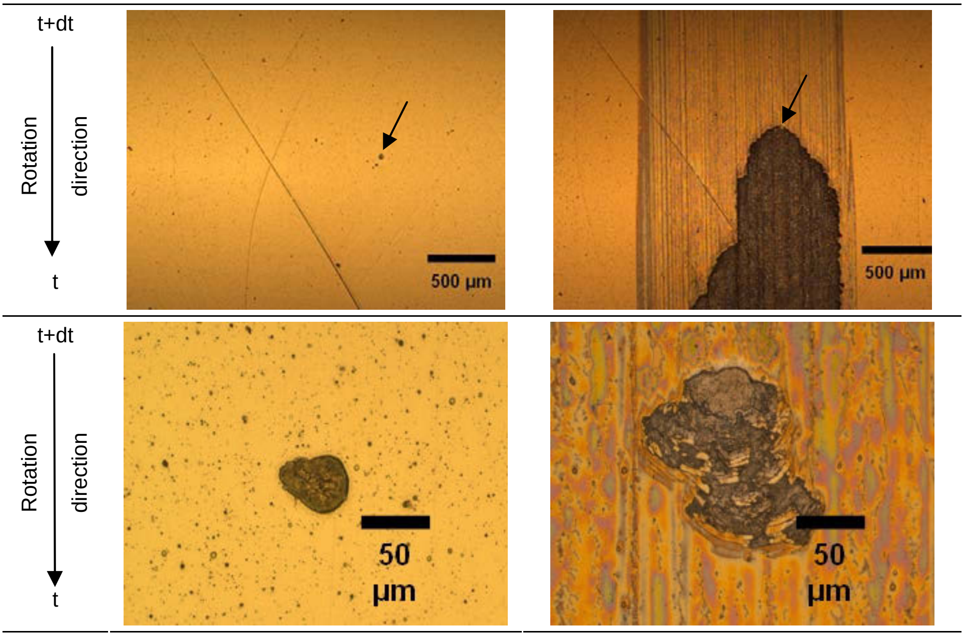

Figure 4.9: Defects on poor slip-rolling resistant coatings inducing spalling at P_{0mean} = 1.94 GPa, FF motor oil at 120° (before test (left) and after (right) 529,000 cycles (top) and 413,000 cycles (bottom) (coatings from batch #7).

To exclude whether the microstructure or the surface state is responsible for the higher slip-rolling resistance, many coated sample discs from the different batches of poor slip-rolling resistant coatings at disposition were mechanically polished by the manufacturer after deposition.

This polishing step should avoid the presence of protruding droplets or, at least, reduce their occurrence on the surface. The mechanical polishing was believed to permit more slip-rolling cycles of the coating before its spalling. However this improvement was not accomplished and rather a worsening is engendered through this additional manufacturing step. Effectively the slip-rolling tests carried out under the severest testing conditions achieved by the best coating, i.e. under a mean starting Hertzian pressure of 1.94 GPa in FF motor oil at 120°C, do not show a better behaviour and worse results were obtained (i.e. cycles to failure under 500,000). This fact is reinforced by looking at the coefficient of friction (COF) over the number of cycles (*Fig. 5.2*, in chapter 5). The polished coatings display another shape of friction curve and the COF becomes unstable more rapidly than for the "as deposited" ones. Moreover the curves presented here refer to coatings deposited on repolished substrates just prior to deposition. Apparently, the repolishing of the substrates does not offer any improvement of the slip-rolling resistance.

4.2 Composition of the coatings

Primarily, the composition of the slip-rolling resistant coating was assessed with EDX, although the measure of light elements is critical. The results of the quantitative analysis were performed using a ZrN reference sample. The elemental concentrations are included in *Table 4.2*. The coating comprises mostly zirconium and nitrogen. Around 5.0 at.-% of carbon were also quantified. Linescan and mapping examinations across polished cross sections remained sterile, carbon was not identifiable, probably due to its low amount and distribution coupled with a too fast mapping time.

Table 4.2: Composition of a slip-rolling resistant measured by EDX from the surface (5 kV, 20 x 20 µm²)

Element line	ZAF	Wt.-concentration %	Wt. % error	Atomic concentration %	At- % error
C K	1.594	1.13	+/- 0.18	4.82	+/- 0.76
N K	1.609	12.92	+/- 0.56	47.08	+/- 2.03
O K	0.000	---	---	---	---
Zr L	1.088	85.95	+/- 0.94	48.10	+/- 0.53
Zr M	0.000	---	---	---	---
Total		100.00		100.00	

The Zr(C,N) coatings were then analysed using WDX since the EDX line scan analyses on polished cross sections do not reveal the presence of carbon. The WDX measurements were carried out in the middle of metallurgical cross sections of samples (sections of coated discs were cut orthogonally and mirror polished). The chemical compositions of the slip-rolling resistant coating and of a coating presenting bad performances during the tribological test are shown in *Table 4.3* where the atomic concentrations for both coatings are given. Boron could not be detected here.

Table 4.3: Results of the WDX analysis of the coating K1 in at. % from the middle of a metallurgical polished cross section (Spot ∅= 1 µm), average of 5 measurements and related standard deviation.

Coating	Element	Zr	C	N	O	B	Ca	(C+N)/ Zr	N/Zr
High	$\bar{x}$ [at.-%]	41.74	5.979	50.67	1.615	n.m.	0.003	1.36	1.21
	σ [at.-%]	0.383	0.583	2.447	0.139	n.m.	0.004		
Poor	$\bar{x}$ [at.-%]	41.25	9.165	47.56	2.015	n.m.	0.005	1.38	1.15
	σ [at.-%]	0.149	1.242	0.809	0.551	n.m.	0.007		

From this table, the zirconium content of both thin films remains constant at about 41 - 42 at.-%, no noticeable differences are measured. In the same way, the sum of the carbon and nitrogen concentrations in both cases is the same. Therefore the (C+N)/Zr ratio has the same value in the slip-rolling resistant and in the poor resistant coating and is almost constant at 1.36 and 1.38 respectively. The two coatings do not basically differ in their composition. A substitution of nitrogen by carbon in the cubic crystal lattice is conceivable, since ZrN and ZrC belong to the same space group “Fm-3m”. Moreover the crystal lattice parameter of ZrN coating is about 4.58 Å and that of ZrC coatings is about 4.69 Å which makes a minor difference of 2.4%. In comparison to the quantitative EDX measurements made at the surface of a sample, the WDX analysis gives comparable results. Moreover the presence of oxygen in the thin films was quantified at around 1.6 and 2.0 at.-%.

However comparing the N/Zr ratio highlights a certain stoechiometric difference since this ratio varies slightly, i.e. with values of 1.21 and 1.15. This statement reinforces the hypothesis of a solid solution of C in ZrN lattice. Anyhow this ratio remains for the whole coating (integral) inferior to 1.33, so that no microscopic Zr_3N_4 domain is expected in the coating. The high slip-rolling resistant coating is however the nearest to this theoretical value. The presence of carbon in the coating could hinder the formation of such a phase, the carbon could promote the stabilization of an Fm-3m structure. Nevertheless this phase richer in nitrogen could exist at the nanoscale, if local variations of the N/Zr ratio take place due to instability during the deposition process or for example when the distance between sample and Zr-target increases.

The presence of oxygen was also determined in both coatings. Atomic concentrations around 1.6 at.-% and 2.0 at.-% were assessed. There is no significant difference, as the standard deviations bring both concentrations in the same range.

To further characterize the two coatings, AES depth profiles were recorded from the surface to the substrate, outside the tribological tracks (region not subjected to external stresses) (spectrometer PHI-700 at 3 keV). From *Figure 4.10*, it is clear that the surface of the two coatings do not possess the same composition.

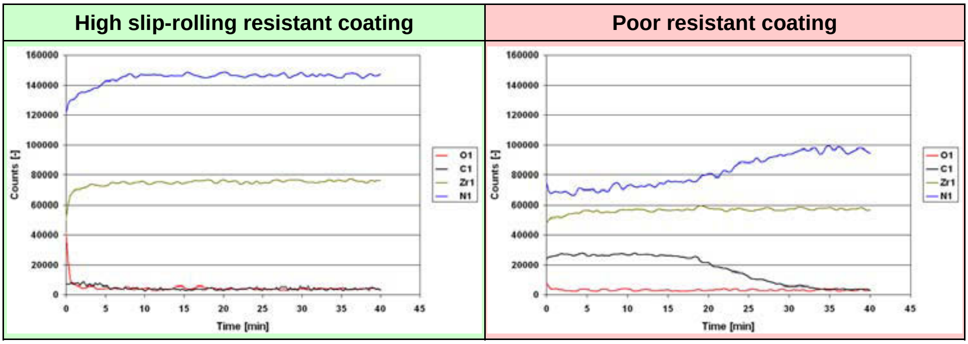

Figure 4.10: AES depth profiling (from the surface to ~1.2 µm deep) of the coating LA02 (~3.6 µm; left, „good“) and MC25 (~2.8 µm; right „bad“)

Effectively the coating exhibiting the poorest slip-rolling resistance comports a more pronounced surface enrichment in carbon. Since the maximal depth after AES-profiling was assessed by profilometry to be in the range of 1.2 µm for both coatings and on the assumption of a constant sputtering rate, the carbon-rich zone measures about 0.5 µm and a 0.3 µm wide gradient transition is noticeable. In the case of the better performing coating, a carbon signal higher than in the rest of the coating is only detected in the first 0.15 µm, i.e. near the surface, and is far lower.

In the same time, more oxygen covers the first 20 – 30 nm of the efficient coating contrary to the other one where the O-signal remains globally constant along the whole profile. The higher oxygen content at the surface finds most probably its origin at the end of the deposition or at the beginning of the cooling, the samples may have been faster/earlier exposed to air. A pollution film of the surface is excluded, the samples were both cleaned with argon before AES measurements following the same experimental procedure.

Anyway, the Zr content remains quite stable along the whole depth in both cases, proof of stabilized target evaporation. This is consistent with the composition results measured by WDX.

By applying the second derivative on the intensity signals (not shown), the small variations of the signals seen along the depth profile do not disclose a correlation among them, i.e. the fluctuations of the N and C signals are not shifted with the fluctuations of the Zr signal. (Nota: measurements were taken by step of 0.25 min, i.e. 7.5 nm). The surface is composed of Zr(C)N.

The surfaces of the two samples were also analysed using AES under lower voltage to only analyse the first nanometres outside the track (*Fig. 4.11*). The carbon concentration of the “bad” sample is definitely higher. The (C+N)/Zr ratio (relating to the intensities) gives in both cases a value around 2 (good: ~2.15 ; bad: ~2.0). It can be noticed that the good sample displays a surface containing more oxygen in the unstressed area than the bad sample, as aforementioned.

High slip-rolling resistant coating	**Poor resistant coating**
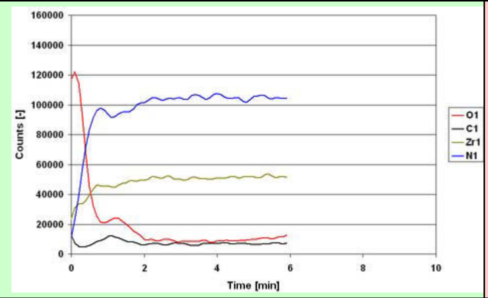	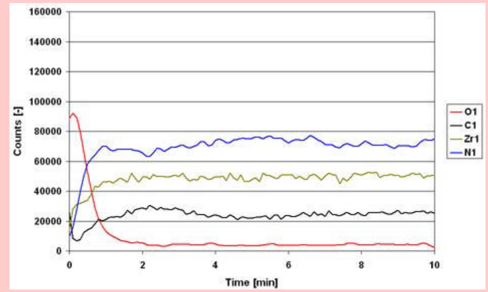

Figure 4.11: AES surface analyses in unstressed areas (left: good sample, LA02 ; right: bad sample, MC21)

AES and WDX results are compared in *Table 4.4* regarding the N/Zr ratio. To permit the comparison between the two methods, the N/Zr ratio of the good sample is weighted by it of the bad sample, in each method of analysis. Almost the same value is obtained (1.05 and 1.10 respectively).

Table 4.4: Comparison of the N/Zr ratio measured by WDX and by AES (ratio of atomic content in WDX and intensity in AES) and resulting weighted N/Zr ratio

Sample	**WDX**	**AES (at the deepest point)**
LA02 (High)	N (at.-%) /Zr (at.-%) = 1.21	N (Int.) /Zr (Int.) ~ 1.88
MC25 (Poor)	N (at.-%) /Zr (at.-%) = 1.15	N (Int.) /Zr (Int.) ~ 1.7
N/Zr_{LA02} / N/Zr_{MC25}	1.05	~ 1.10

Referring to the composition data in *Table 4.3*, the phase diagram of Zr–C–N ternary carbonitride system and XRD analyses results in ZrN (cubic-type, a =0.4578 nm, JCPDS 35-753) and ZrC (cubic-type, a =0.4693 nm, JCPDS 35-784), it is found that all the ZrCN films were of δ-$Zr(C_xN_{1-x})_{1-y}$ phase. So, concerning the chemical composition of the coatings, the only distinct and relevant difference resides in the presence of an upper region rich in carbon in the case of the inefficient coating.

4.3 Surface analysis after test

4.3.1 Coating tested in unadditivated paraffin oil at room temperature

First of all, the surfaces of the slip-rolling resistant coating before and after tribological solicitation are depicted in *Figure 4.12*. Outside the wear track, i.e. in its unsolicited state or here more precisely “as deposited”, one can discern a large amount of bright points reflecting the presence of lot of peaks or droplets produced during the deposition or at its end and previously detected by means of the profilometer and reflected by the roughness values. Some holes are also apparent, probably let by sheared droplets (hole does not reach the substrate) or slack droplets ejected (hole reaches the substrate). Besides these deposition defects related to the unfiltered arc evaporation process, the surface is relatively smooth without any cracks or local debonding.

After tribological testing, the surface loses these bright points evocating the loss of the droplets. The track contains no more droplets but obviously holes having quietly the same size as the droplets. Furthermore the track contains more holes than the side, suggesting the creation of holes through shearing or, worse, loosing of the droplets. It can act as micro reservoir of lubricants. However in the case of the poor slip-rolling resistant coatings it seems that most of the holes created reach the substrate.

At higher magnification, the surface is no more as smooth as in its unloaded state. Effectively in the track, wear marks are found all oriented in the same direction (the rolling direction), deteriorating the smoothness of the surface. At this scale, droplets can be recognized again. They lose their sharpness, letting them appear less bright on the SEM observations. Moreover some of these droplets are wear particles stuck on the surface.

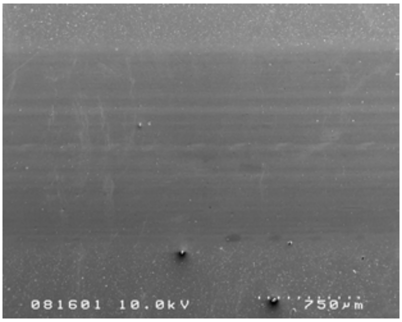

Side of the wear track | Wear track

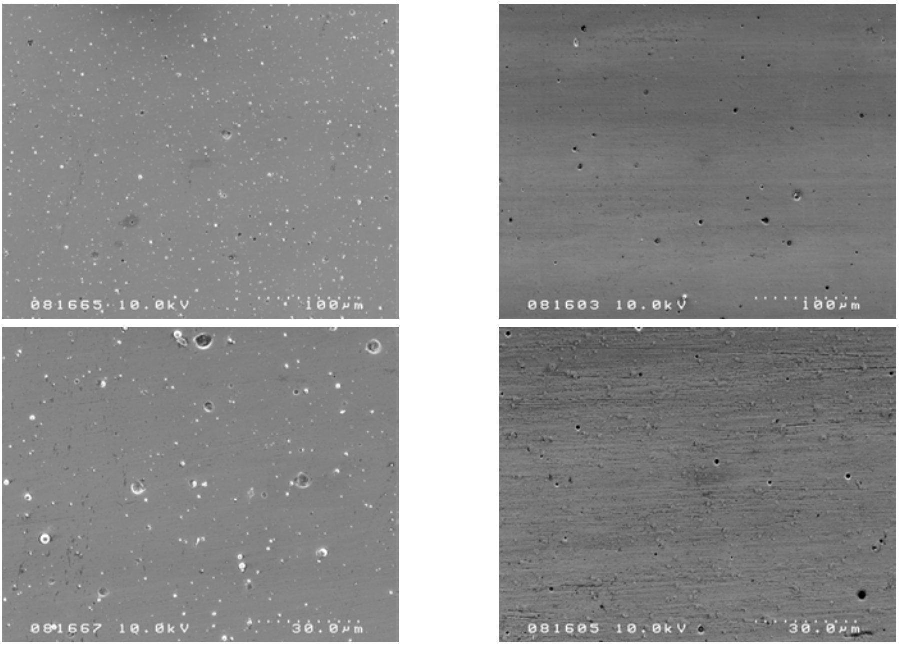

Figure 4.12: SEM observation of changes of the coated surface of the slip-rolling resistant coating (batch #1, LA02))tested in unadditivated paraffin oil at 1.5 GPa and Room Temperature after 10,000,000 cycles.

In the track of the coated cylinder, after 10 million cycles in paraffin under an average Hertzian pressure of 1.5 GPa, the oxygen profile is no longer so abrupt (*Fig. 4.13*) compared to the one displayed in *Figure 4.11* (unstressed area), the signal levels off at a deepest location. Mutually the Zr and N contents grow more slowly than in the unstressed area (Fig. …). This is due to the presence of “external” chemical elements, i.e. not included in the composition of the coating. Effectively, iron and chromium traces are present in the first two minutes of the diagram, following the oxygen trend. This presence denotes that a very thin tribological layer is produced and transfer from the counterpart takes place during testing despite of the slip motion, which could wear this transfer layer. The transferred iron is probably in an oxidized state.

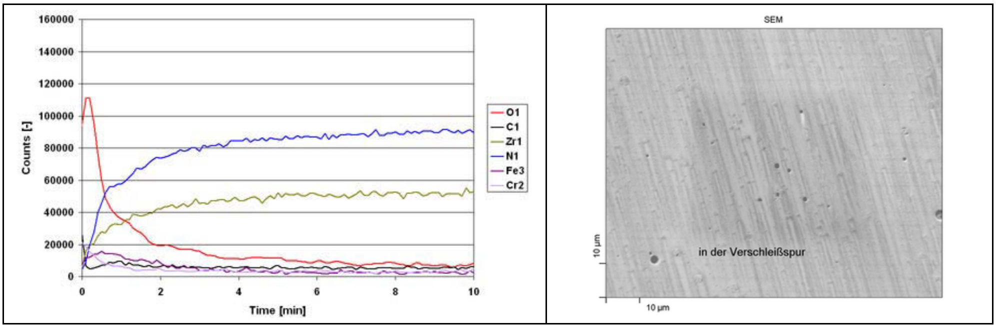

Figure 4.13: AES surface analysis in the track of the same good sample (batch #1) after test in paraffin and corresponding SEM picture.

The same sample has been analysed using electronic microscopy too (*Fig. 4.14a and Fig. 4.14b*). The aforementioned finding can be further observed in SEM pictures superimposed with EDX mappings (*Fig. 4.15*). Effectively on the SEM picture, fine stripes oriented in the rolling direction prove an adhesive transfer from the counterpart on the coating. These stretched transfer traces are probably generated by the surfaces in contact submitted to sliding due to the slip induced by the difference of rotating speeds. Effectively the SEM picture exhibits spherical particles made of steel, iron and chromium being similarly located (see corresponding EDX mapping). These particles are created by adhesive wear or transfer. Applying a shear stress produced by the combination of friction and slip will stick and stretch them on the coated surface giving those elongated shapes. Oxygen is also found on the same areas as iron, suggesting the formation of iron oxides, as previously observed with AES surface analyses. Neither phosphor nor sulphur, characteristic of oils containing SAP (sulphur, ash, and phosphor), are detected with EDX and superimposed with iron and oxygen, for the reason that no lubricant additives are mixed in the pure paraffinic oil.

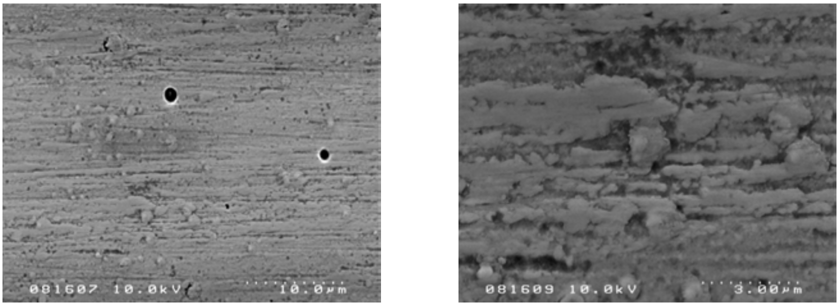

Figure 4.14a: SEM pictures of the slip-rolling resistant coating (batch #1, LA02) tested in unadditivated paraffin oil at 1.5 GPa and Room Temperature after 10,000,000 cycles.

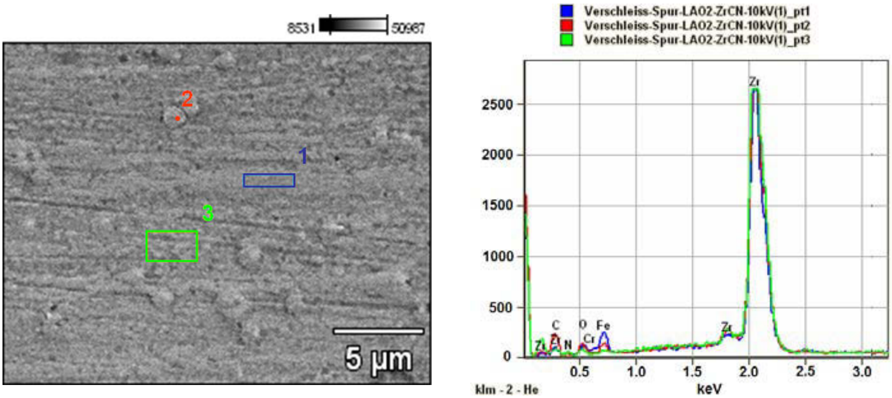

Figure 4.14b: SEM picture and corresponding local EDX spectra of the slip-rolling resistant coating (batch #1, LA02) tested in unadditivated paraffin oil at 1.5 GPa and Room Temperature after 10,000,000 cycles.

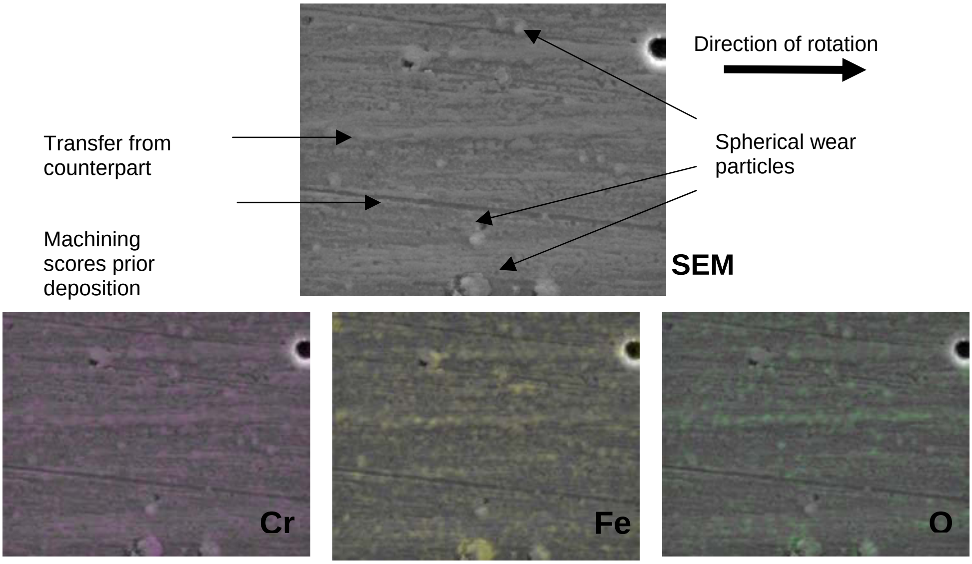

Figure 4.15: Surface observation and corresponding EDX mapping of the slip-rolling resistant coating (batch #1) tested in unadditivated paraffin oil at 1.5 GPa and Room Temperature after 10,000,000 cycles.

4.3.2 Coating tested in FF 0W-30 motor oil at 120°C

Furthermore, the coated parts tested in motor oil at 120°C exhibit colour changes in the track (see light microscopy in *Figure 4.7*). Using electron microscopy, bands oriented in the direction of rotation can be revealed. With EDX it could be established that these bands contain calcium, sulphur, and oxygen (*Fig. 4.18*). As the original surface does not display such chemical elements, they can only originate from the oil, more precisely from the additives package used in the motor oil. This is the proof that the commonly industrial additives can react with the coating surface to form a protective layer as usually verified for systems functioning in mixed/boundary lubrication. The elements detected (Ca, S and O) refer surely to calcium sulfonates. Effectively overbased (with high Total Basic Number) or neutral calcium sulfonates (*Fig. 4.16*) are frequently applied in engine oils. They were firstly used as detergent but exhibit good EP (Extreme Pressure) and AW (Antiwear) properties too [MAR08].

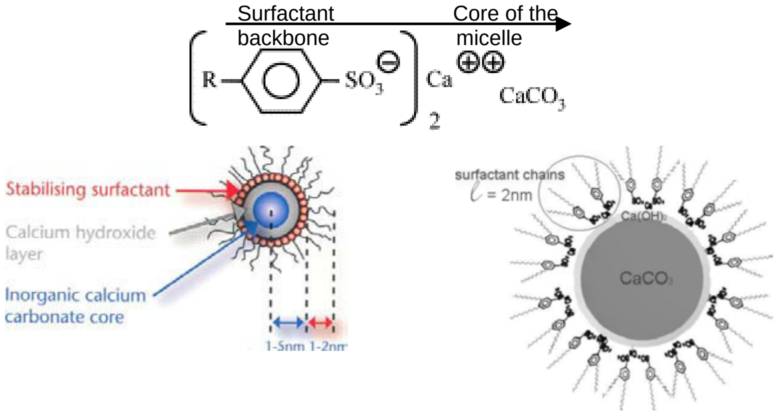

Figure 4.16: Schematic representation of an overbased sulphonate detergent particle (typical diameter from 5 to10 nm, OCABS: overbased calcium alkyl benzene sulfonate micelle) [NAJ06, HUD06]

Moreover, signs of Zn traces are detectable around 1 keV, indicating the presence of Zn-based additives. The most known and widely used are Zinc dialkyldithiophosphates (ZDTP also called ZnDTP or ZDDP, *Fig. 4.17*) forming a zinc (poly)phosphate protective film from a few nanometres up to 100 nm having high antiwear properties. It also shows antioxidant properties. However phosphorus cannot be identified in the EDX spectrum as the P K-line lays at about 2.1 keV and suffers from the traditional peak overlapping with zirconium.

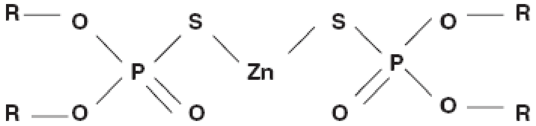

Figure 4.17: Schematic structure of the ZDDP molecule [GRA00]

Generally the aforementioned additives are formulated for the most widespread contact configuration, i.e. steel/steel contact. As the surface analyses carried out on coatings tested in unadditivated paraffin oil revealed that iron is transferred from the counterpart on the coating, it is conceivable that the additives react with this transfer layer. It was verified (Fig. 4.18) by the simultaneous presence of Fe, Ca, S and Zn in a tribofilm formed on the coating. But this possibility was however not always established, as the EDX spectra presented in Figure 4.18 (left, top) contain in a case S, Ca and Zn without a Fe peak corresponding to a transfer, and in the second area the spectrum indicates Fe without typical elements originating from additives (left, bottom). Then it proves that the additives react to some extent with the steel transfer, but do really react with the coating too.

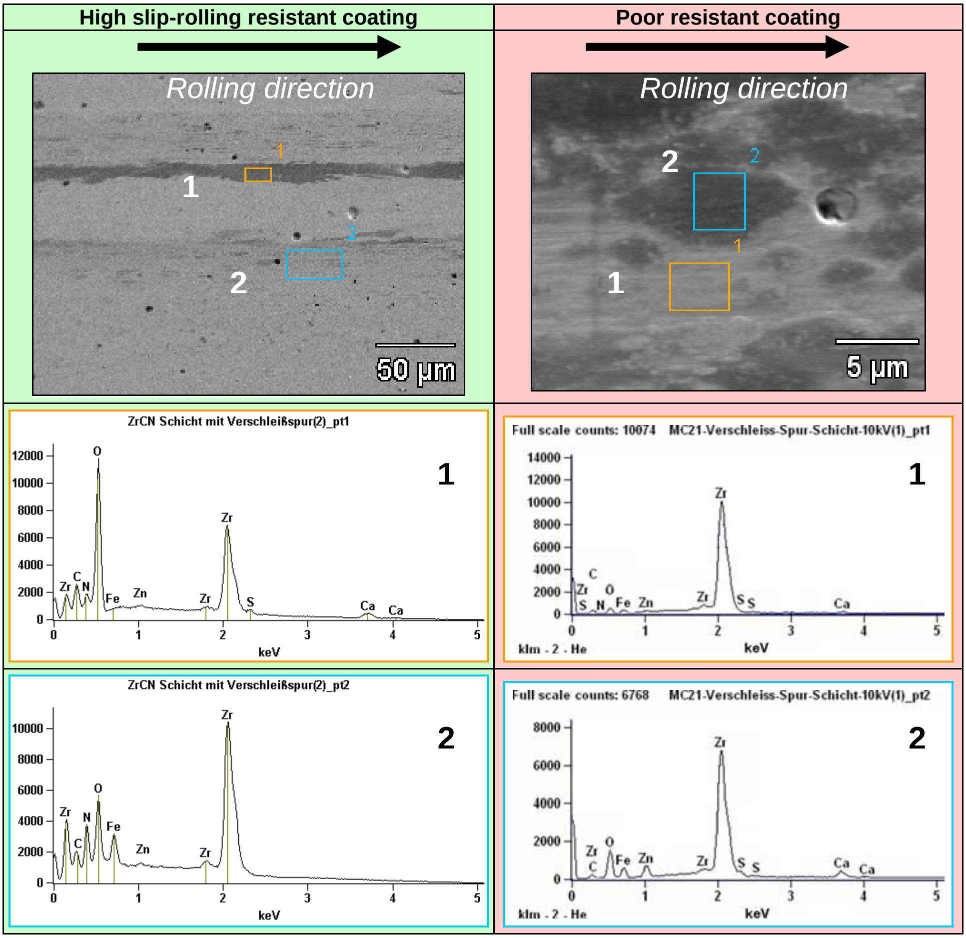

Figure 4.18: surface analysis of a slip rolling resistant coating (batch #1, LA02) and of a poor resistant coating (batch #7) tested in FF motor oil at 120°C

4.4 XRD results

4.4.1 X-Ray diffraction spectrum

The coating was examined with XRD. The CuKα 2θ diagram using the Bragg-Brentano configuration is displayed in *Figure 4.19*. The angular positions of the peaks corresponding to ZrN (JCPDS 35-753), ZrC (JCPDS 35-784) and Zr_2CN (JCPDS 03-062-8779 calculated from NIST using POWD-12++ [BIT63]), all belonging to the space group Fm-3m n° 225, are also given for comparison purposes. From the diagram, the diffraction peaks of the coating are very close to those of the ZrN. Compared to the JCPDS values of ZrN (JCPDS 35-0753), the peaks measured in θ/2θ are therefore slightly shifted to lower angles, i.e. higher interplanar (or d-spacing) values. This is in accordance with the expectation of compression residual stresses since the somewhat higher deposition temperature usually introduces considerable residual compression stresses in PVD coatings (as a result of the higher thermal expansion of the steel substrate since $\alpha_{SV30} = 10.8\ 10^{-6}\ °C^{-1} > \alpha_{ZrN} \sim 7.2\ 10^{-6}\ °C^{-1}$ [ENE03, FRI97]). Applying the Scherrer equation (4.1), the evaluated average grain size is between 7 to 10 nm involving a fine grain structure.

$$t = \frac{0.9\lambda}{B \times \cos(\theta)} \tag{4.1}$$

where λ is the wavelength of Cu Kα, B is the FWHM of the diffraction peak, θ is the peak position, and t is the grain size of the thin film.

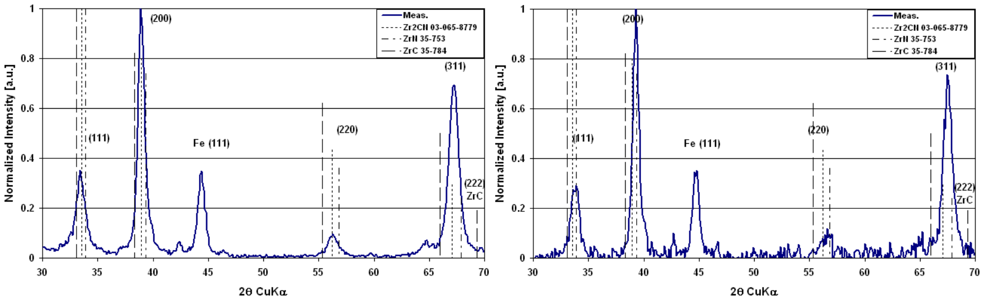

Figure 4.19: XRD spectrum of a Zr(C,N) coating with Cu Kα wavelength (left: XRD, Bragg-Brentano ; right: GIXRD, grazing incidence: 2°)

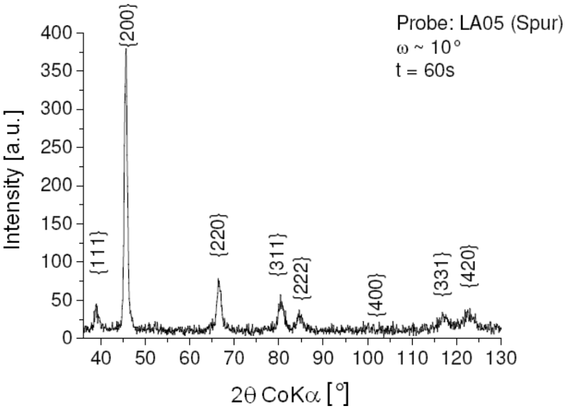

Figure 4.20: XRD spectrum of a Zr(C,N) coating with Co Kα wavelength, incidence: 10°

A peak near 2θ = 42.5° cannot be indexed. Regarding the main elements present in the coating (Zr, N and C), one of the possibilities for explaining the peak can be the presence of Zr_3N_4. Effectively this was reported in [LAM05] for ZrN coatings produced by reactive magnetron sputtering. For chemical compositions of these ZrN_y thin films with y lying between 0.81 and 1.35, two phases of different structures exist. A structure cfc-ZrN was found in a broad range of composition of $y = 0.81$ to $y = 1.30$ and an orthorhombic phase Zr_3N_4 for $1.30 < y \leq 1.35$. However with regard to the peak angular position, it does not really match with the orthorhombic phase. According to [CHH05], a second form of Zr_3N_4 also exists which is cubic and can be produced by cathodic arc deposition. Its two main peaks are located at around 32.9° and 41.4° with the Cu Kα wavelength. Anyway they also do not correspond with the peak found at 42.5°. By the way, no registered phases based on the composition $Zr_xN_yO_z$ correspond to this unidentified peak. One possibility could be the formation of a phase based on a mix of Fe, Zr and Cr by the diffusion of zirconium at the interface between substrate and coating during the first minutes of the deposition at the start of the sputtering of the zirconium target under high substrate polarization. Different peaks near the values of 43° for a material based on Fe, Zr and Cr were found in [VIZ08] and assigned to the C14 phase (θ-ZrFe1.5Cr0.5, 1997, JCPDS 42-1289).

The (200) peak is always the pre-dominant peak in the present XRD spectra. Probably a preferred orientation, i.e. a growth texture, is present along the coating thickness. Often <100> and <111> fibre textures are reported in ZrN or TiN coatings. In ZrN, for a N/Zr ratio above 1.1, a strong <100> with a medium <110> and a weak <111> texture was found by Fillit and Perry [FIL91]. Change of preferred orientation is commonly observed with the coatings thicknesses variation too. Moreover as an fcc structure like TiN, ZrN is supposed to exhibit the sequence of (111)–(220)–(200) orientation with increasing ion bombardment in plasma based ion implantation & deposition [HEI08]. It is suggested that this preferred orientation is determined by the competition between two thermodynamic parameters, the free surface energy and the strain energy [ARI06].

Using GIXRD (Grazing Incidence XRD), the same peaks are found as with the Bragg-Brentano method. The Zr(C,N) coatings are likely to have a fcc B1 (NaCl) structure as the detected peaks are close to those of ZrN.

4.4.2 Residual stresses in the coatings

In order to clarify if the coatings possess different states of residual stresses, Zr(C,N) coatings with the most similar thicknesses were chosen as the amount of stress in a film can change as a function of coating thickness [FIL91]. The angular drift of diffraction peaks in an XRD spectrum is directly linked to the residual stresses since the crystal lattice and the interplanar distances of diffracting (hkl) planes vary under stresses. The determination of residual stresses based on XRD was done by the $\sin^2\Psi$ method (d_Ψ versus $\sin^2 \Psi$) using Co Kα radiation (λ = 1.7889 Å) on the (331) peak (crystallographic factor Γ for cubic crystal structure $\Gamma = (h^2k^2+k^2l^2+l^2h^2)/(h^2+k^2+l^2) = 0.27$) with a Huber Ψ diffractometer equipped with a parallel beam unit consisting of a horizontal soller-slit followed by a (LiF200) monochromator analyser crystal, in the rocking curves configuration in ω-2ϑ scan mode ($\omega \sim 10°$; $111° < 2\vartheta < 129°$) The X-ray elastic constants (XECs) needed to interpret the residual stress measurements were calculated with the program Xec [WER98] as $\frac{1}{2}s_2^{\text{Kröner}} = (1+\nu)/E = 3.195\ 10^{-6}\ \text{MPa}^{-1}$ and $s_1^{\text{Kröner}} = -\nu/E = -0.67110^{-6}\ \text{MPa}^{-1}$, values homogeneous with those of [SAR06] where the coating deposition method was similar with a final coating thickness of about 2 µm. Analysis of the measurements was performed with the Kröner model [KRÖ58], corresponding to an intermediate solution between the extreme conditions set by the Reuss and Voigt models for values of XECs. Here each crystallite is considered as an elastic anisotropic particle embedded in an isotropic matrix (then XEC depend on the crystal planes used). The assumption of a principal pure biaxial planar stress state is assumed (principal stresses σ_1 and $\sigma_2 \neq 0$, $\sigma_3 = 0$, direction 3 perpendicular to the coating free surface, i.e. with liberty of dilatation or contraction in this direction). Residual stresses were determined at three temperatures (room temperature, 100°C and 200°C) to follow their stability.

Three tribologically untested samples from three different batches (MC23, MC56 and LA126) as well as a coating having demonstrated good slip-rolling resistance (LA05) were analysed. Residual stresses in the circumference direction and in the transverse direction are given in *Figure 4.21* for measurement at room temperature.

All the samples show compressive residual stresses which is commonly reported for PVD nitrides coatings on steel substrate. They all vary between -2,000 MPa and -4,000 MPa. The samples MC23 and LA126 tend to display lower residual stresses in the circumference direction as in the transverse one. On the contrary, MC56 and LA05 (outside the tribological track) display a somewhat relative homogeneous distribution of the plane residual stresses (in the limits of the errors of measure) with values a little bit higher in the case of MC56. On the sample LA05 in the track after 10 million cycles at 120°C and P_{0mean} = 1.94 GPa, the residual stresses seem to be reduced, but in the range of the measurement errors it can be also accepted that they remain almost unchanged.

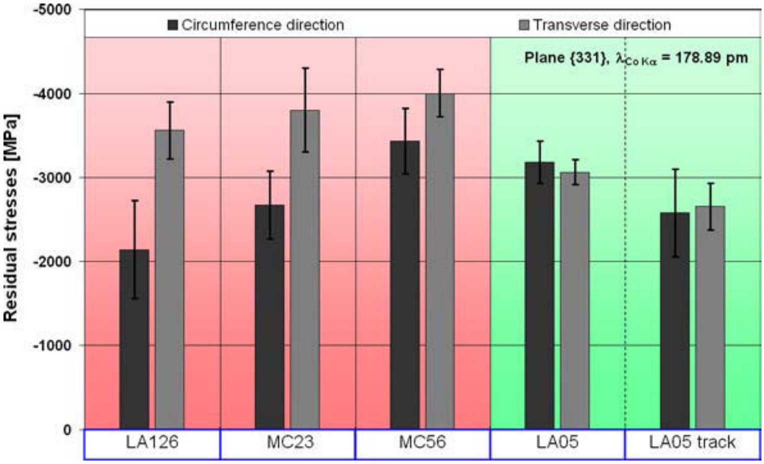

Figure 4.21: residual stresses measured with the sin²ψ method after the Kröner model in three poor slip-rolling resistant coatings (labelled MC56, LA123 and MC23, samples having not been tribologicallly stressed) and a sample after being stressed over 10 million cycles (LA05, stresses measured outside and in the tribological track). Slip-rolling resistance increases from left to right.

Since the severest tribological tests are performed in motor oil at 120°C, the coatings were also investigated concerning their residual stresses at 100°C and 200°C in order to evaluate their sensitivity to temperature. In some cases they were measured twice (*Fig. 4.22*) at two different locations in order to check the reproducibility. As reference, the residual stress in the track of LA05 (high slip-rolling resistant coating) was measured two times at the same location and the third measurement was carried out at another location. The results are each time the same.

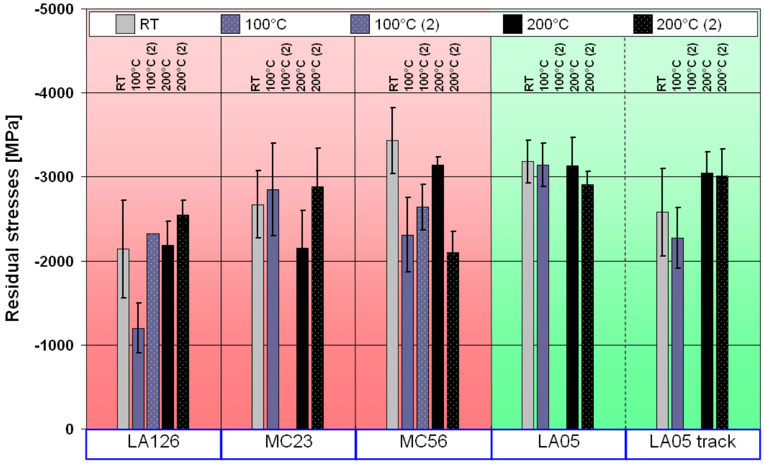

Figure 4.22: Residual stresses in circumference direction measured in the coatings at RT, 100°C and 200°C. Slip-rolling resistance increases from left to right.

Table 4.5.: measured circumferential residual stresses in the track of the high slip-rolling resistant coating at 200°C at different locations.

LA05 track (high slip-rolling resistant coating)	
1st position	-3,050 ± 250 MPa
	-3,080 ± 280 MPa
2nd position	-3,010 ± 320 MPa

The sample LA05, which was thought to present a decay of its residual stresses in the tribologically stressed track (*Fig. 4.21*), shows comparable values at 200°C in and outside the track. At 200°C no variation is detected. Therefore, the track should also display the same residual stress state as the unstressed side at room temperature. This coating is thermally and mechanically stable for temperature between RT and 200°C. However, it should be noticed that for nanocrystalline materials the measurement of compressive residual stresses is more difficult as they do not thermally relax in the same way as polycrystalline materials.

Concerning the other samples, no clear trends appear: the coating MC56 could globally suffer from a decrease of its residual stresses (but with two different trends between the two measure sequences). On the contrary the residual stresses in LA126 tend to increase with the temperature. Anyway, these coatings seem to be more unstable or/and inhomogeneous, as the reproducibility of the measures is not assured. The residual stresses vary with location and perhaps with temperature. Moreover, if the samples do not have the same texture it is hard to interpreted the residual stresses as a strong texture in coatings is generally assumed to reduce the residual stresses because of the preferred orientation of the crystallites which diminishes their mutual distortion.

The origin of stress in thin films is due to the grown-in stress, i.e. the intrinsic residual stress, and extrinsic residual stresses also known as thermal stresses. The thermal stress can be estimated due to the difference in thermal expansion coefficient between film and substrate materials. If T_d is the temperature of deposition then the thermal stress σ_T is proportional to (T_d – T) $\Delta\alpha$ - ε^{pl} (plastic strain) at any temperature T. The intrinsic residual stress is related to the incident energetic particles impinging on film surfaces during deposition and defects or stresses having lattice inherent origins. Since all the coatings were deposited under almost the same conditions and therefore involving that the value of the thermal stress participating in the residual stress is in each case the same. Differences in intrinsic residual stresses could explain the bad reproducibility of the measurements of the residual stresses for the poor resistant coatings.

For nitrides coatings, in the case of stress temperature cycles an increase of the compressive residual stress was reported with an increase of the temperature in the range of room temperature up to 200°C and then a decrease of the compressive state from 200 to 300°C for TiN in [BIE05]. The same phenomenon was revealed for CrN with an increase of the residual stresses until 350-400°C and decrease of the compressive state from 400°C to 700°C [MAY01] during the first temperature cycles. This phenomenon was supposed to be related to defect annihilation in the coatings as it occurred no more after some temperature cycles. The establishment of a purely regular linear evolution without hysteresis between increase and decrease of the temperature was only effective after a few temperature cycles and is thought to be related to the complete intrinsic stress relaxation. Therefore in view of the residual stress results it is conceivable that this effect takes place in the case of the poor slip-rolling resistant coatings and not for the good coating since no veritable variations were noticed here. The good coating could show a better temperature stability in the range of the considered temperatures due to its microstructure hindering the displacement of defects or dislocations. Another possibility is that the slip-rolling resistant coating was already submitted at a temperature of 120°C during 18 days, inducing an already well-established state of the residual stresses.

4.5 Microscopic analyses of cross sections

Observations along the cross section using different techniques of microscopy (optical, SEM, FIB and TEM) were undertaken on a high slip-rolling resistant coating and a coating displaying poor slip-rolling resistance. The aim was to identify and highlight any differences in their architecture and microstructure.

4.5.1 Architectural overview

With optical microscopy, some horizontally oriented stripes in the cross section were distinguishable in a cross section of the high resistant coating. They are not occurring because of a preparation failure, but should have been authentic as they were detected in other cross sections prepared of the sample. They really belong to the architecture of the coating. Nevertheless the presence of those stripes was not visible in the poor rolling resistant coating. This noticeable difference motivated for further observations with SEM to check if these stripes were parts of the coating or due to any optical effects.

First of all, two SEM devices (Hitachi S4100 and Zeiss SUPRA 40 equipped with EDX) were used to confirm the presence of the stripes. With both devices, the picture quality could not really be enhanced. Effectively, the substrate does not favour the image sharpness because of the magnetic remanence of the ferromagnetic martensite in the Cronidur 30 substrate. Anyway, the microscopy confirms: horizontal stripes exist in the slip-rolling resistant sample and are inexistent in the low resistant one by comparing the two SEM micrographs of *Figure 4.23*. Using the Quadrant Back Scattering Detector (QBSD) on the second microscope permits a better visualization of the stripes, indicating eventual variations of the chemical composition within the coating as the backscattered electrons are emitted “proportionally” following the atomic number. The electronic microscopy allows then the following statements: the stripes are not artefacts and the architectures of both coatings differ in spite of the same deposition procedure. Unfortunately, EDX line scans along the cross section do not deliver more information, presumably due to the thinness of the layers. Therefore, the coatings were further analysed using Focused Ion Beam (FIB) for cross section imaging in the groove and for further processing in TEM lamellae. Their preparations were done by the focused ion beam technique (Strata™ 200xP, FEI) in combination with an in-situ lift-out method (Kleindiek Nanotechnik).

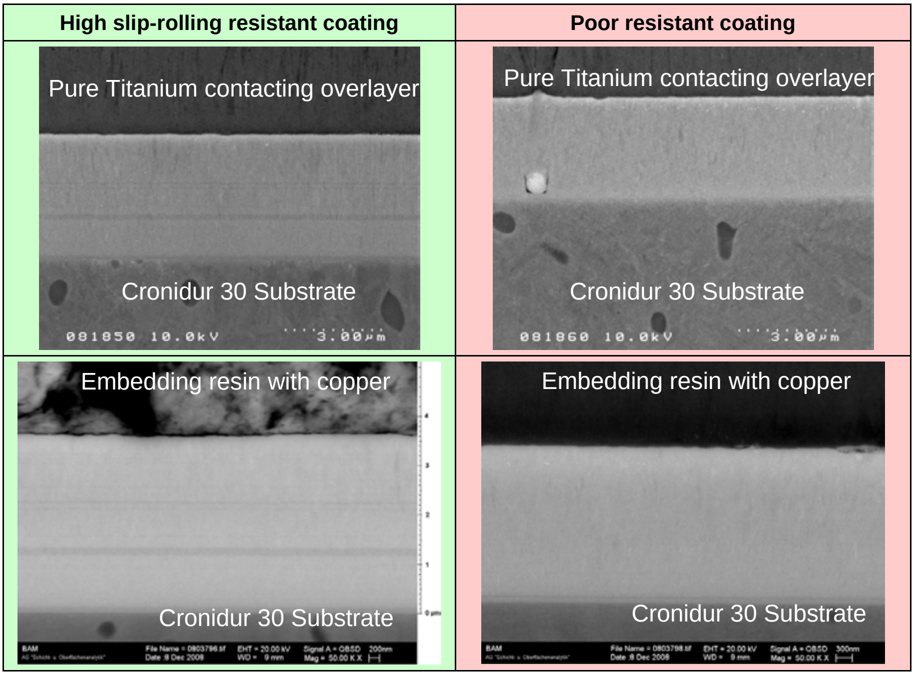

Figure 4.23: SEM pictures of cross sections taken from the high slip-rolling resistant coating (left, batch #1, LA02) and the poor one (right, batch #6) with two different electronic microscopes (top/bottom).

In the same manner, a structural comparison of both samples was performed by means of FIB milling and TEM. The illustrations in *Figure 4.24* are representing cross sections of the samples carried out by FIB. Here the stripes are not visible in both samples but another difference can be stated: the sample on the left of the figure, i.e. the one having shown the best performance in slip-rolling, displays a “graduated grain morphology”, from a fine grain size at the interface with the steel substrate towards a “coarser” one along the thickness in the direction of the surface. In the case of the sample on the right side of the figure, i.e. coating having failed rapidly, this graduation is not so distinct or hardly discernible. But without any doubt, between the substrate and the whole coating, a fine grain stripe forming an interface is identifiable. Here, only a fast graduation of the grain size takes place and is localised in the first ~200 nm of the coating.

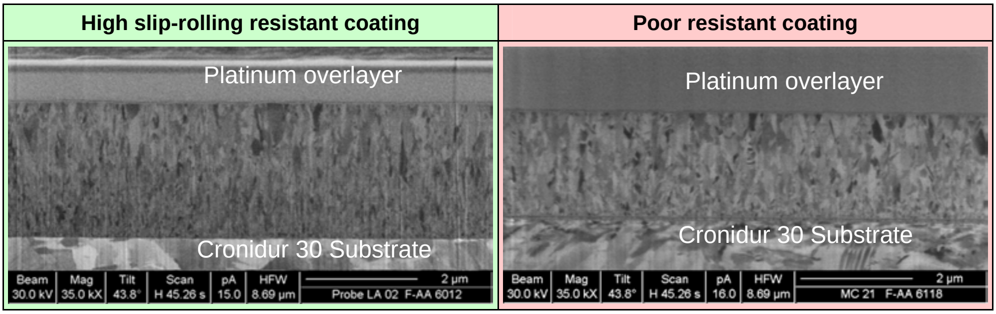

Figure 4.24: FIB cross sections of the high slip-rolling resistant coating (left, batch #1, LA02) and the poor one (right, batch #6)

Considering the TEM cross section overview, the coating displaying a high slip-rolling resistance exhibits architectural differences compared to the poor one. The presence of a very fine multilayer architecture is obvious in the picture on the top of *Figure 4.25*. This multilayer disposition contrasts with the picture on the right side, where such an arrangement does not take place. The absence of fine stripes in the poor slip-rolling resistant coating makes it structurally different, more basic.

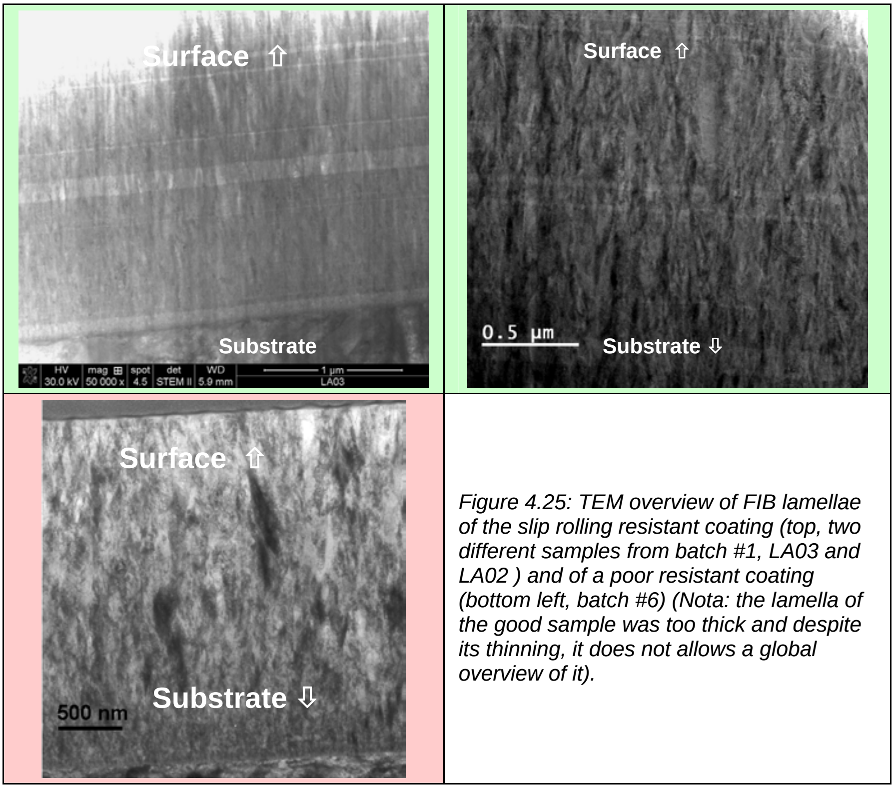

Figure 4.25: TEM overview of FIB lamellae of the slip rolling resistant coating (top, two different samples from batch #1, LA03 and LA02) and of a poor resistant coating (bottom left, batch #6) (Nota: the lamella of the good sample was too thick and despite its thinning, it does not allows a global overview of it).

Both samples display a dense thin columnar structure (or even fibre-like), commonly reported for PVD nitride based coatings formed at $T < 0.3\,T_m$ (T_m, melting temperature, following the structure zone diagram of Thornton [THO86]). Apparently the structure is crystalline all along the cross section. However, in the high resistant slip-rolling coating, multilayers are randomly dispersed in the whole coating in form of packages or simply individually. No regular wavelength between layers is noticeable. Nevertheless within the packages, a certain periodicity is revealed. Effectively in the 140 nm layers package represented in *Figure 4.26* a regular alternation of bright and darker stripes is present. From this picture, a periodicity of about 2 nm (bright) and about 6 nm (darker) can be deduced for the package arrangement.

So, the stripes observed by means of optical microscopy and SEM are justified by the presence of a microstructure organised in multilayers at different scales: at a “microscale”, where brighter stripes were identified by SEM and TEM (see *Fig. 4.23* and *Fig. 4.25*) and at a nanoscale analysed by TEM (*Fig. 4.26* and *Fig. 4.27*), indicating that these stripes are composed of very thin layers regrouped in packages.

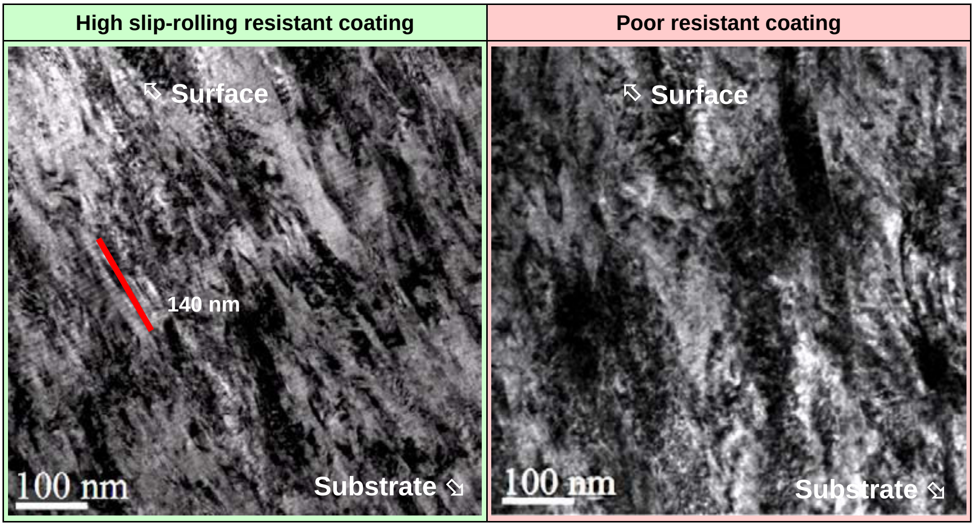

Figure 4.26: TEM overview in cross section taken from the high slip-rolling resistant coating (left, batch #1, LA02) and the poor one (right, batch #6) after lamellae preparation thanks milling by means of FIB.

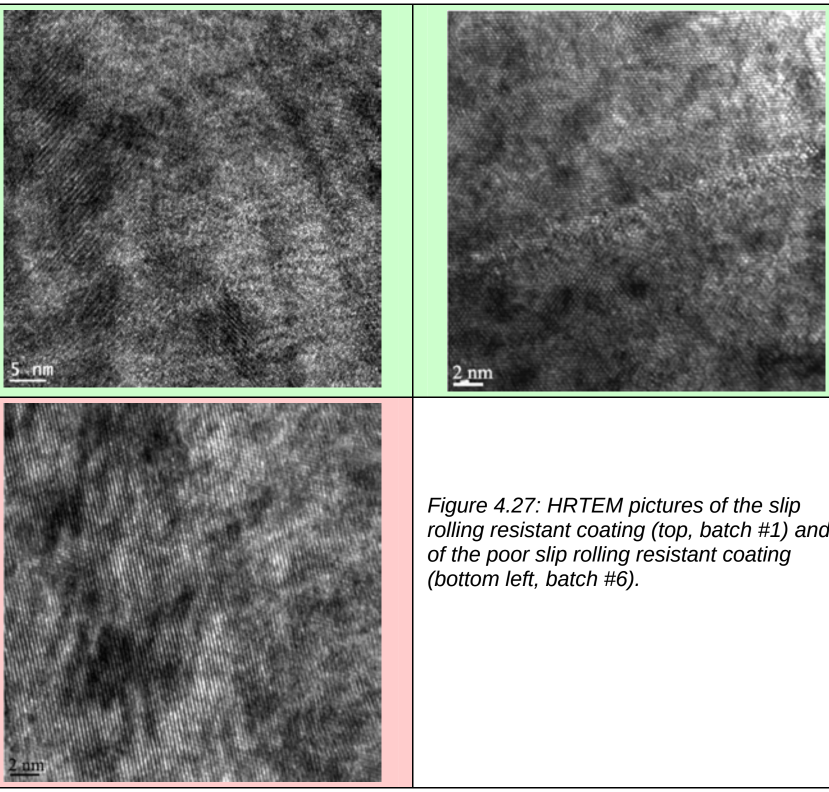

Figure 4.27: HRTEM pictures of the slip rolling resistant coating (top, batch #1) and of the poor slip rolling resistant coating (bottom left, batch #6).

4.5.2 Analysis of the “intra nanolayers” in the high slip-rolling resistant coating

The use of HAADF (High Angle Annular Dark Field) around a multilayer package permits the distinction of two types of layers, the HAADF analysis technique allowing the distinction of local difference in atomic number. The periodicity formed by the 15 bright and 16 dark layers seems almost regular on about 143 nm (involving an average layer thickness of about 4.6 nm). In the HAADF observation modus, the differences in the gray scale are representative of variation of atomic number: the brighter appearing domains contain more heavy elements (here Zr), than the darker ones which can be richer in light elements (such as C or N) or contain fewer Zr. Then, *Figure 4.28* clearly depicts local variations in the composition within the coating, then engendering the layered structured.

This is consistent with the previous observation made with SEM using the backscattered modus. This is also confirmed by the qualitative EDX linescan (step of 4 nm). Low variations of C and N are noticeable. However no correlation between the variation of the C and N signal can be found. Sometimes they are in phase and sometimes out of phase along the EDX-linescan. Oxygen and boron are also detected but in much lower quantity (Boron is due to the BN isolator forming the cathode shielding). Anyway the darker lines contain more light elements than the surrounding “matrix” and than the brighter stripes. Considering that the darker stripes correspond to a decrease of Zirconium content or increase of the content of light elements involves the displacement of the N/Zr ratio towards higher value, therefore promoting the formation of Zr_3N_4.

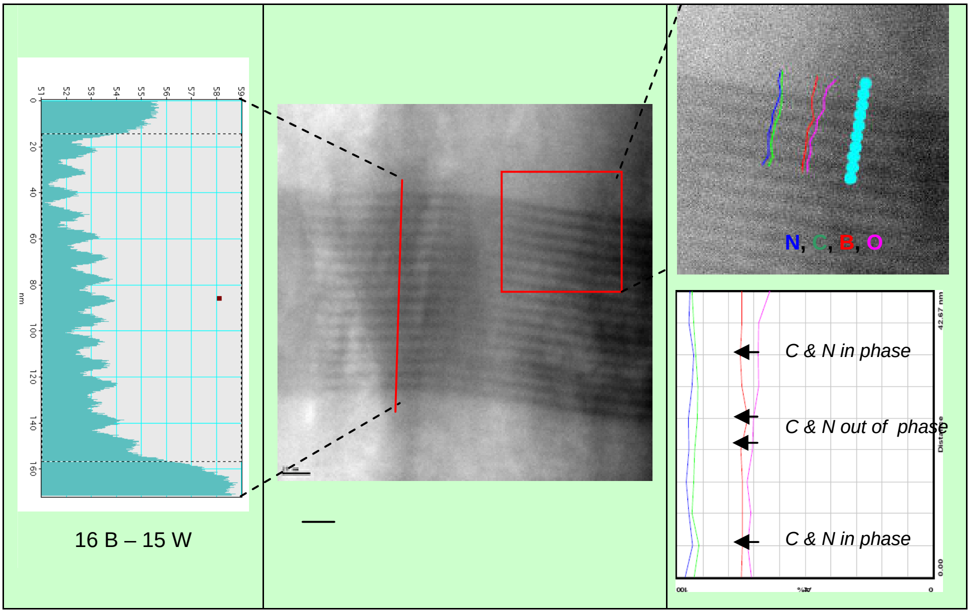

Figure 4.28: Package periodicity (left), HAADF (High Angle Annular Dark Field) picture in the good coating LA02 from batch #1 (scale: 20 nm, middle) and local EDX linescan (right)

Observation of a domain containing multilayers by HREM and EFTEM could not deliver a clear assertion about its composition: under HREM multilayers were clearly present (*Fig. 4.29*) with thicknesses of about 3 nm to 6 nm but the superposition of the images provided by the C and N jump ratio in EFTEM does not really accord with the layered structure in HREM, although a certain colour i.e. composition alternance is noticeable. The thinness of the layers with low variations of composition added to a possible drift could be responsible of the undefined imaging in EFTEM.

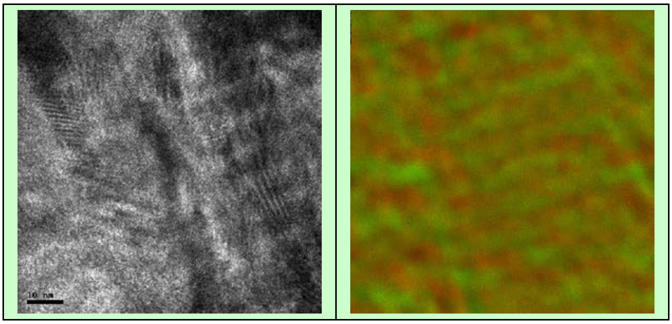

Figure 4.29: HREM picture and corresponding combined C (red) and N (green) Jump Ratio Image (EFTEM modus, coating LA02 from batch #1)

The C Jump ratio and N jump ratio images in *Figure 4.30* are here however plainly out of phase, involving in this case a clear out of phase variation of C and N contents. The presence of the layer is the consequence here of locally higher C content, where an increase of C is compensated by a decrease of N. The presence of higher C content in the layer is supported by the map image.

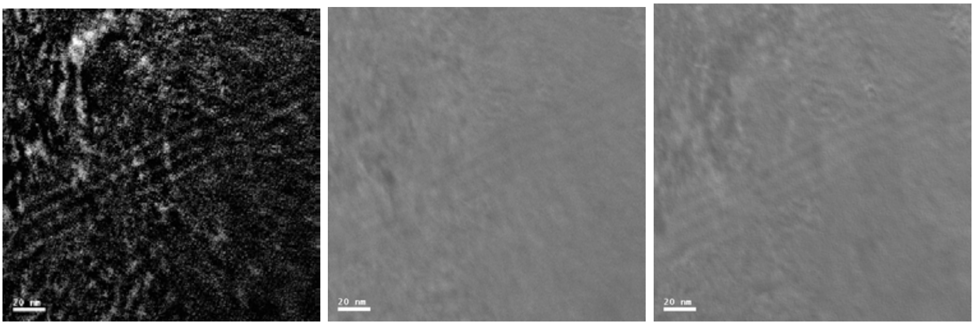

Figure 4.30: C map (left), C jump ratio image (middle) and N jump ratio image (right) showing a layer package from the middle of the coating (EFTEM modus, scale 20 nm, coating LA02 from batch #1)

It was reported that coatings based on Ti(Zr)N/CNx couples are thermodynamically unstable with respect to the formation of TiN–TiC and ZrN–ZrC solid solutions. In a same way, it is possible that two kinds of multilayers are present in the coating: some formed by alternative C and N composition in the domain of the rock-salt structure (thermodynamically stable if the N or C+N content do not diminish under 45 at.% in view of the phase diagram and diffusion of C in ZrN) and some based on higher variations of the N/Zr or (C+N)/Zr ratio leading to the formation of alternate Zr(C)N and $Zr_3(CN)_4$.

Some authors reported the variations of the multilayer periodicity in dependence on the rotation speed of the substrates. For example Evans [EVA05] found in his nanocomposite TaC/a-C:H thin films a dependence of the periodicity of the nanometre-scale lamellar film structure with the substrate carousel rotation rate. In the present case, perhaps the satellites in the deposition chamber were not correctly/constantly rotated or instability of the plasma or of the arc induced variation of N/Zr ratio creating “randomly distributed” nanolayers.

4.5.3 SAD and NBD analyses

The following TEM pictures and SAD patterns presented in the two following figures were obtained with the TEM JEOL 4000FX at an acceleration voltage of 400 kV for both samples (*Fig. 4.31 and 4.32*). The aforementioned isotropic behaviour of the good coating could also be microstructurally materialized. In Figure 4.31, TEM pictures from the interface of the high slip rolling resistant coating are shown. A very thin Zr “interlayer” and the multilayers are identifiable.

The SAD pattern on the left (arrows indicate the examined location) reveals almost complete rings without being diffuse, enlightening that crystalline grains are randomly oriented, i.e. with no preferred orientation near the substrate/coating interface. The interplanar d-spacing values calculated from the radius of the rings are very closed to those of cubic ZrN (PDF card 04-004-2860). At about 200 nm above the interface the diffraction pattern does not show anymore quasi perfect rings but the rings are partial and contain diffraction spots. It can be the sign of a texture in development or the diffracting grains become bigger than those near the interface. Anyway a huge amount of spots is depicted in the diffraction pattern which signifies that no preferred orientation (i.e. texture) takes place.

High slip-rolling resistant coating

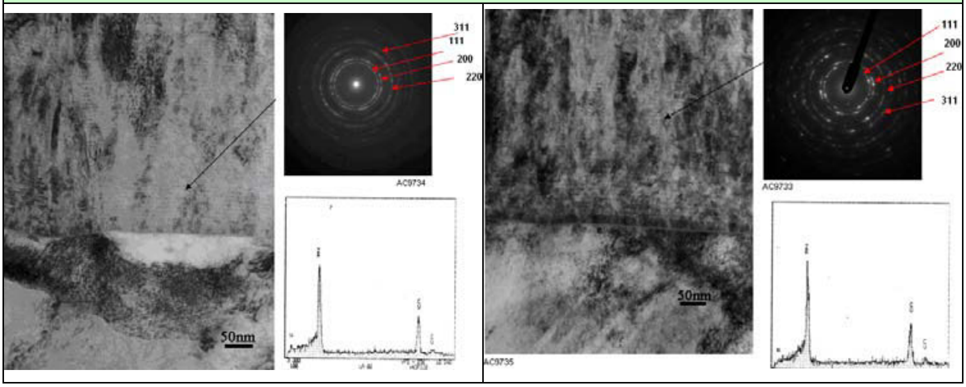

Figure 4.31: Electron diffraction pattern of the high slip rolling resistant coating (LA02 from batch #1) near the substrate interface. Diffraction rings are indexed following the d values of the ZrN PDF card 04-004-2860.

However differences were found concerning the core of the coating between the two samples, i.e. the high and the poor slip rolling resistant coatings. The diffraction rings are sharper and more distinct in the case of the high slip rolling resistant coating than in the case of the poor resistant one. Moreover numerous intense spots are included in the rings and are better dispersed, revealing either a more isotropic microstructure or smaller diffracting grains. In the core of the coating, the corresponding d-spacing values belong to the cubic ZrN (PDF card 04-004-2860). No ring or spot related to the presence of other phases were detected here using selected area electron diffraction in both cases.

High slip-rolling resistant coating	**Poor resistant coating**

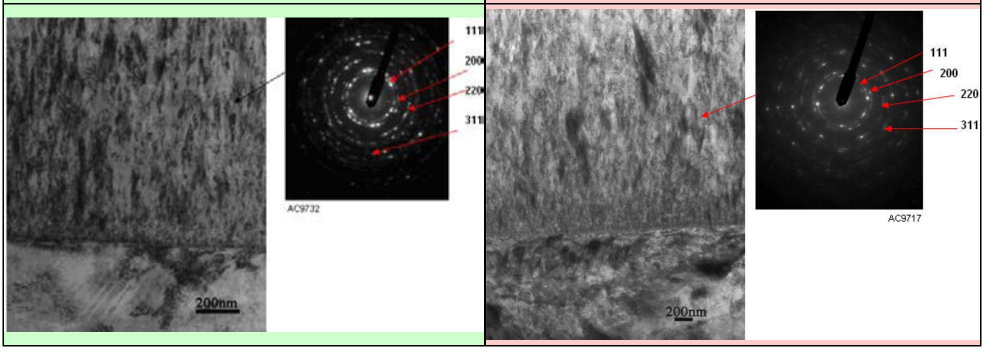

Figure 4.32: Electron diffraction pattern of the core of the coating taken from the high slip rolling resistant coating (LA02, batch #1) and of the poor resistant coating (MC21, batch #6). Diffraction rings are indexed following the d values of the ZrN PDF card 04-004-2860.

Table 4.6: Proximity of the rock-salt ZrN (PDF 04-004-2860) and Zr_2CN (PDF 01-071-6065)

ZrN PDF 04-004-2860		**Zr_2CN PDF 01-071-6065**	
$d_{Lit.}$ [nm]	hkl	$d_{Lit.}$ [nm]	hkl
0.265	111	0.267	111
0.229	200	0.231	200
0.162	220	0.163	220
0.138	311	0.139	311
0.132	222	0.133	222
		0.106	331

Other TEM/STEM investigations were carried out using a JEM-2200FS (JEOL) equipped with FEG, Omega-type energy filter, HAADF detector and EDX system (JED-2300, JEOL).

For both samples, typical SAD patterns are depicted in *Figure 4.33*. The ED ring pattern shown permits to conclude that the samples are both crystalline as it only contains rings almost continuous or spots arranged on rings; no diffuse scattering characteristic for amorphous phase is visible.

The diffraction rings marked 1,2,4,5,6 demonstrate the main phase of the coating belongs to the B1 NaCl type crystal structure. The measured d-spacing values and corresponding planes are listed in *Table 4.7*.

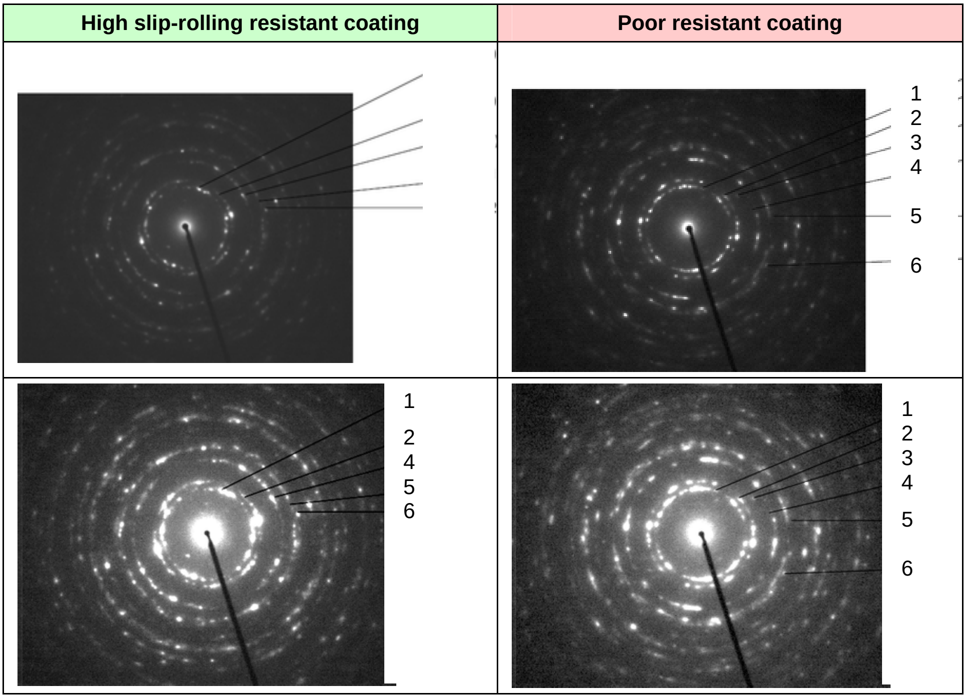

Figure 4.33: Typical SAD patterns for both samples (bottom, same picture with saturated grey levels to better highlight the rings and spots) (LA02 from batch #1, MC21 from batch #6)

The rings are more continuous in the case of the slip-rolling resistant coating, indicating a smaller grain size distribution and probably a higher equiaxial texturing. Sharp spots are of higher presence in the poor resistant coating, favouring a higher textured coating. However if the grain sizes are not similar, it is hard to make a clear and final assertion concerning the higher texturing of the coating showing a poor slip-rolling resistance.

Table 4.7: measured d-spacing values compared to ZrN and Zr_3N_4 phase (++ Reflex nearby)

Ring No.	Exp.d Value [Å]	ZrN (a = 4.63 Å)		Zr_3N_4 (Orthorhombic)
		d	plane	
1	2.64	2.67	(111)	(211)++
2	2.29	2.31	(200)	(311)++
3	1.88		-	(421)++
4	1.62	1.64	(220)	(511)++
5	1.39	1.40	(311)	(071)++
6	1.33	1.34	(222)	(560)++

The measured d-spacing values are listed in *Table 4.7* and are the same for both samples. All the values may also correspond with the orthorhombic Zr_3N_4 phase. Noteworthy is the presence of a spot in the poor resistant coating which do not correspond to a plane of the rock-salt ZrN structure but correspond with the (421) of orthorhombic Zr_3N_4. In the case of the high slip rolling resistant coating all the values respect well the equation describing the separation between adjacent planes in a cubic crystal which is given by

$$\frac{\sqrt{h_1^2 + k_1^2 + l_1^2}}{\sqrt{h_2^2 + k_2^2 + l_2^2}} = \frac{d_2}{d_1} \tag{4.2}$$

However local presence of $Zr_3(CN)_4$ cannot be excluded in the high slip-rolling resistant coating and is revealed by NBD.

With NBD (Nano-Beam Diffraction) a small and nearly parallel beam is used and data can be taken with the sample aligned directly to the low order processing zone axis. It enables the obtainment of diffraction patterns from regions of the specimen in the range of some nanometres or less in diameter. This analytical method permits the identification of phases but only locally. Then it was applied to both samples extracted from the high slip-rolling resistant coating and the poor slip-rolling resistant coating in order to identify nanophases. The NBD experimental results and their corresponding simulations are recapitulated in the *Figures 4.34* and *4.35*.

In both samples, a phase very near to cubic ZrN could be identified (*Fig. 4.34*). Carbon and oxygen can be responsible for some irregularities or differences between NBD measures and simulations as they can be dissolved in solid solution in the crystal lattice inducing a distortion of it. Nevertheless a high agreement is noticeable in any case.

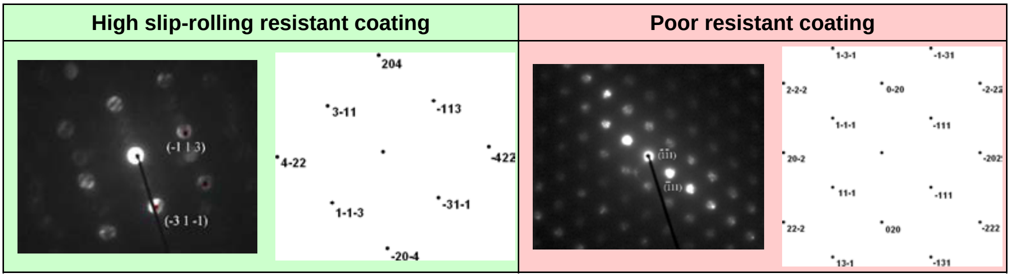
High slip-rolling resistant coating | **Poor resistant coating**

Figure 4.34: Examples for NBD diffraction pattern, that corresponds to cubic ZrN [25-1] orientation (left, (batch #1) and in [101] orientation (right, (batch #6) with their corresponding simulations

In a similar manner, in both coatings a phase corresponding to orthorhombic Zr_3N_4 was revealed by NBD measurements (*Fig. 4.35*) with a good agreement between simulated orthorhombic Zr_3N_4 and the measurements carried out with TEM. Although no ring or spot related to the presence of Zr_3N_4 were found in the SAD diffraction pattern of the high slip-rolling resistant coating (*Fig. 4.33, left*), its existence was even so identified with NBD. It is probably due to a very low amount of Zr_3N_4 or a really localized occurrence, as for example a localization of Zr_3N_4 in the nanolayers.

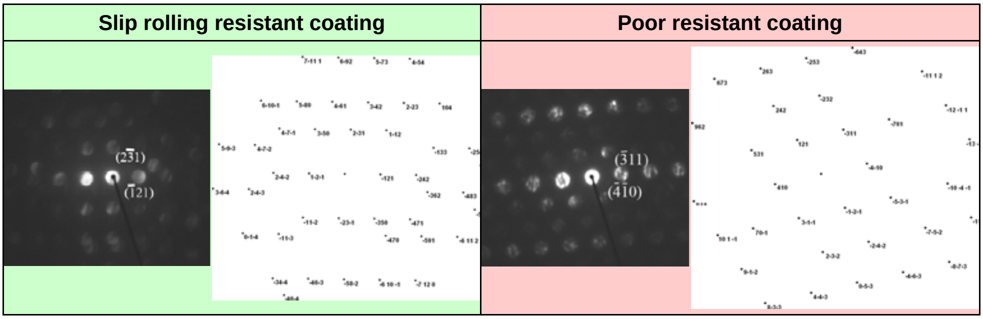
Slip rolling resistant coating | **Poor resistant coating**

Figure 4.35: Examples for NBD diffraction pattern (up), that corresponds to orthorhombic Zr_3N_4 in [53-1] orientation (left, batch #1) and in [-14-7] orientation (right, batch #6) with their corresponding simulations

4.5.4 Interface between coating and substrate

The “substrate-coating” interface was also analysed by TEM. The interface between substrate and coating is commonly designed by adding a bond layer or interlayer for enhancing adhesion and reducing contact stress as the interface is often seen as weak point of coated systems. Through the aforementioned deposition process, no metal (i.e. Zr) bond layer is intentionally deposited for all the samples. *Figure 4.36* depicts the interface of the slip-rolling resistant coating and that of the poor resistant coating.

According to the TEM pictures, a kind of interlayer is present though it is unintentionally deposited, and their thickness differs: in the case of the slip-rolling resistant coating this “bondlayer” is in the range of 20 nm thick and for the poorer one a thickness of about 75 nm is measured. This very fine “bondlayer” is made in zirconium and is produced during the first phase of the coating deposition or rather during the Glow Discharge cleaning phase.

The Zr-target is activated and high energetic Zr ions are accelerated to clean the substrate by impinging its surface, building then this very thin film.

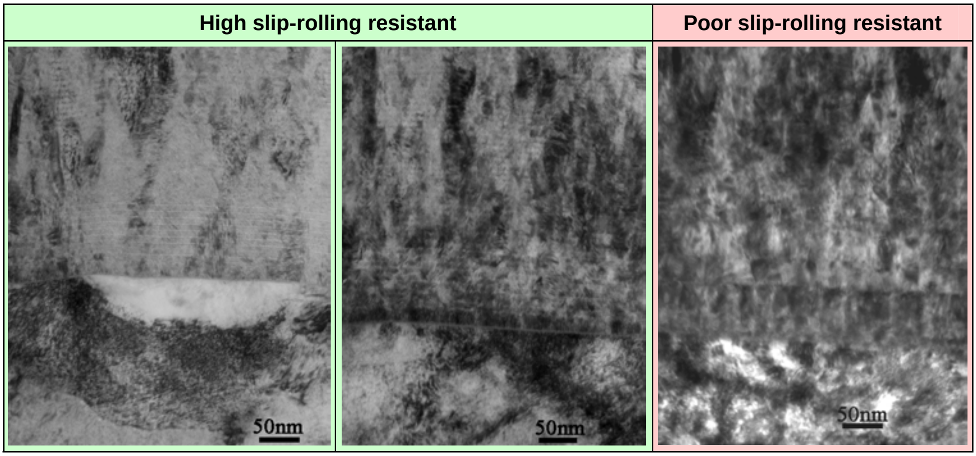

Figure 4.36: TEM pictures taken with microscope JEOL 4000FX (400 kV) of the coatings LA02 (~3.6 µm; left and middle, „high“) and MC21 (~2.8 µm; right „poor“).

EDX line scans were performed at this critical position between substrate and coating. The analytical results are summed up in *Figure 4.37*. Apparently, in both cases the thin layers are principally formed of zirconium but without a sharp transition between substrate and coating. Effectively a diffusion zone involving zirconium, iron and chromium is also existent and in both cases around 80 nm (60-70 nm for the good one, about 80 nm for the poorer resistant one). In all cases higher contents of C, N and B are found in the coating. The interpretation of the oxygen distribution should be carefully performed. Apparently oxygen displays a higher content in the substrate according to the EDX linescan, but this is not true due to the overlapping of the EDX-lines of Cr and O. Anyway a small difference is seen: the coating showing worse performances includes a real and non-negligible increase of the oxygen content just after the transition between substrate and coating: its interface contains locally a greater amount of oxygen.

In order to confirm the authenticity of this oxygen rise, EFTEM (Energy Filtered Transmission Electron Microscopy) analyses at the interface are shown in *Figure 4.38*. It totally corroborates the observation made with the EDX linescan. The increase of oxygen content is verified at the interface just at the beginning of the coating. In the same time, the fictitious character of the higher oxygen content in the substrate is demonstrated. This oxygen peak is however not found in the slip-rolling resistant coating using either EDX or EFTEM. (It should be noted that the grey scale between the two EFTEM images was not normalised, actually the grey scale for the good coating was set lower, involving that the appearing oxygen is actually by far lower than in the bad sample).

High slip rolling resistant coating **Fe, Cr, Zr, B, C, N, O**	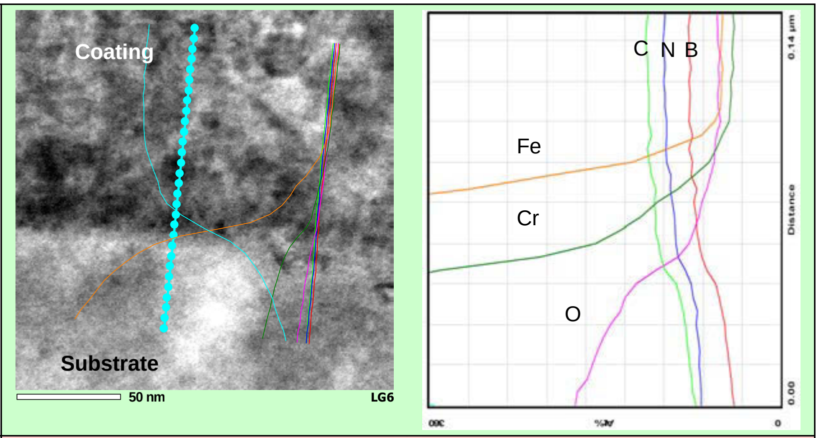
Poor slip rolling resistant coating **Fe, Cr, Zr, B, C, N, O**	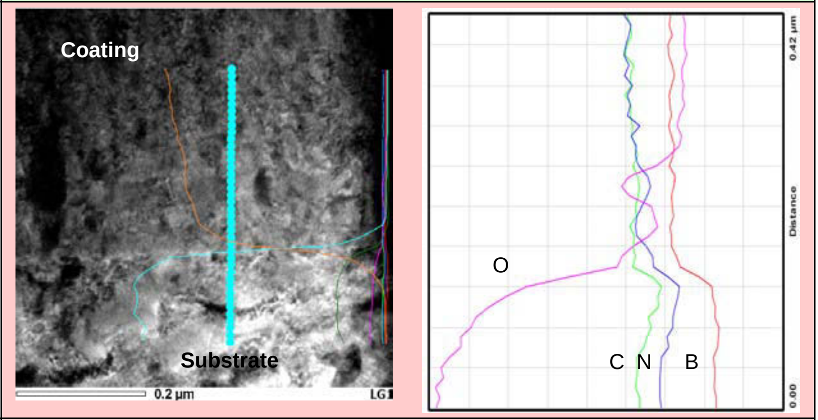
Poor slip rolling resistant coating **Fe, Cr, Zr, B, C, N, O**	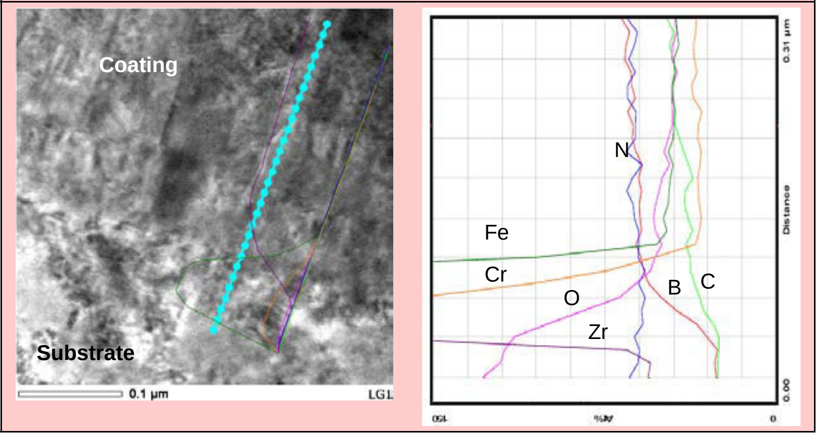

Figure 4.37: EDX Linescan in TEM over the interface between substrate and coating (up: coating LA02 batch #1, middle & down: coating MC21 batch #6).

	High slip-rolling resistant	**Poor slip-rolling resistant**
TEM picture	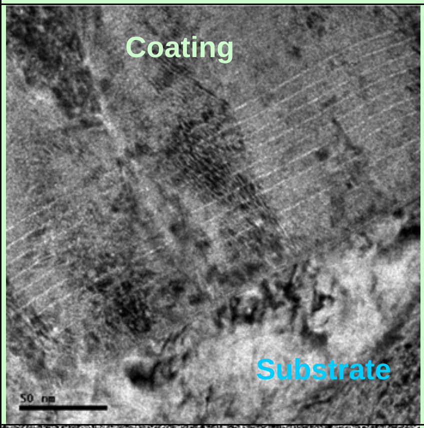	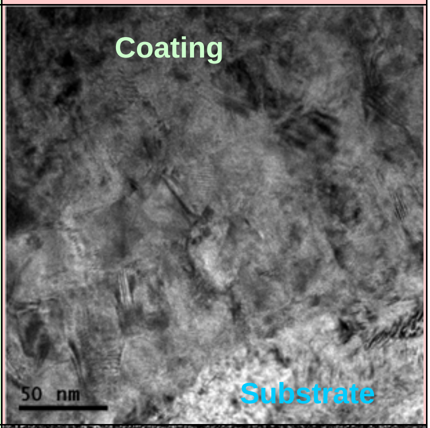
EFTEM Mapping of oxygen	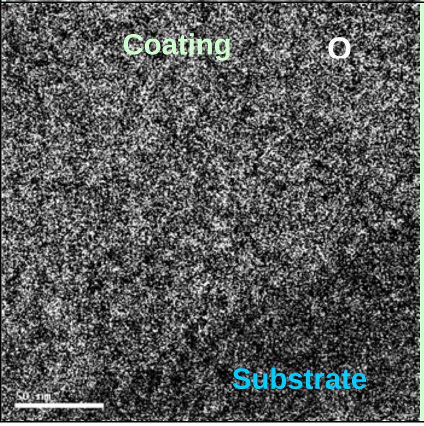	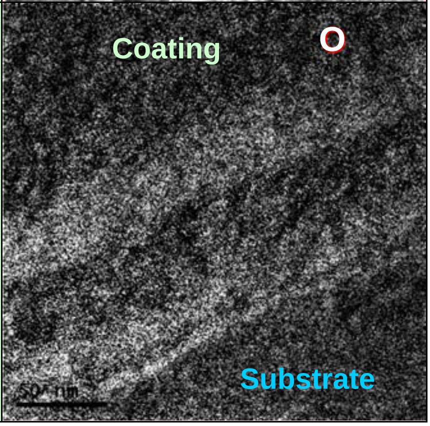

Figure 4.38: TEM analysis (picture with concordant EFTEM Mapping of oxygen) at the interface between substrate and coating: coating LA02 „High“ (left) and coating MC21 „bad“ (right).

4.6 Nanoindentation

The coatings were also investigated by nanoindentation in order to measure their mechanical properties, especially the young’s modulus and the hardness. *Figure 4.39* represents a typical load-displacement curve of the high and poor slip-rolling resistant coatings measured up to maximum load of 30 mN with a Fischerscope H100 apparatus equipped with a Vickers indenter. The calculated quantities W_{total}, W_e, W_r, $E/(1-v^2)$, H_{plast} and $h_{r'}$ are total, elastic and plastic work regard to the displacement of the indenter, modified Young's modulus, plastic hardness and depth defined by the point of intersection of the tangent with the indentation depth axis, respectively (*Tab. 4.8*). At first glance, it seems evident that the curves of both coatings do not differ and hence the resulting mechanical values are the same (*Tab. 4.8*).

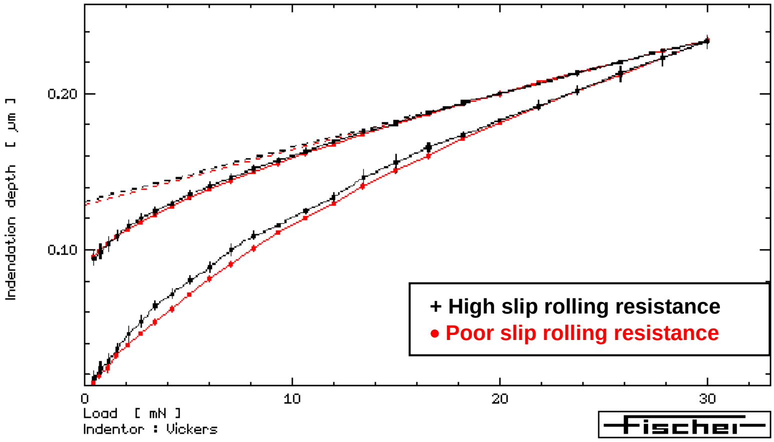

Figure 4.39: Depth vs. nanoindentation force curve at a maximum force of 30 mN for both coatings (apparatus: Fischerscope H100, Tekniker, Vickers indenter)

From the indentation curve a modified (or reduced) Young's moduli $E/(1-\nu^2)$ around 615 GPa could be deduced and a plastic hardness (hardness calculated from the size of the remaining plastic deformation) of around 67,000 MPa equivalent to 6,900 HV (when assumed that HV = 0.102 H_{plast}). The elastic recovery work is around 64%. This method does not perform well enough to distinguish divergences between both coatings.

Table 4.8: Nanoindentation results at a maximal force of 30 mN (Vickers indenter)

	High slip rolling resistant coating	**Poor slip rolling resistant coating**
$E/(1-\nu^2)$ [GPa]	619 ± 38	615 ± 20
H plast [MPa]	68,674 ± 5,120 (7,005 HV)	66,363 ± 2,824 (6,769 HV)
h r' [µm]	0.129 ± 0.005	0.131 ± 0.003
W_{total} [nJ]	2.74	2.64
W_e [nJ]	1.73 (63.02 %)	1.71 (64.78 %)
W_r [nJ]	1.01 (36.98 %)	0.93 (35.22 %)

Therefore a second indentation technique was also used. A higher maximal test load of 100 mN was chosen and nanoindentation was performed with the QCSM modus (Quasi Continuous Stiffness Measurement) developed by ASMEC (*Fig. 4.40*). A second poor slip rolling resistant sample was also investigated and its tribological tracks too (*Tab. 4.9*).

All the "Force vs. depth" nanoindentation curves measured on the side of the track of the samples (i.e. representing the as deposited state) display nearly the same profile. Compared to the measure made with the nanoindometer Fischerscope 100, the curves cannot also be separated until a normal force of 30 mN. The measured young's modulus is lower since the reduced modulus decreases with the contact area which also depends on the load applied [VEP03].

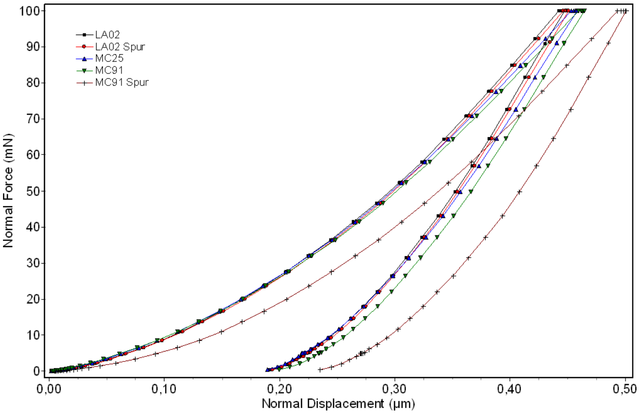

Figure 4.40: Force vs. depth nanoindentation curve at a maximum force of 100 mN for both coatings (apparatus: Universal Nanomechanical Tester UNAT in QCSM modus, ASMEC GmbH, Berkovich indenter)

Table 4.9: Nano indentation analysis at a maximal force of 100 mN for a Poisson's ratio assumed by 0.25 (Berkovich indenter, average of 10 individual measurements)

	LA02	**LA02 Spur (2)**	**MC25**	**MC91**	**MC91 Spur (2)**
Slip- rolling resistance	**High**		**Poor**	**Poor**	
h_{max} [µm]	0.447	0.451	0.458	0.465	0.501
H [GPa]	26.19	26.53	26.39	25.19	19.23
dH [GPa]	0.96	2.20	1.21	0.62	5.25
HV [kp/mm^2]	2476	2508	2495	2382	1819
dHV [kp/mm^2]	90	208	115	59	497
E (1) [GPa]	340.1	326.1	308.0	307.4	295.7
dE [GPa]	13.2	26.1	13.5	7.8	85.5
W_e [%]	61.2	61.1	61.6	58.9	56.4

(1) for an assumed Poisson's ratio of 0.25
(2) Spur = Track

Globally, the results show that the surfaces of the coatings have very similar mechanical properties. Within this method the high slip-rolling resistant coating exhibits a somewhat higher Young's modulus (340 GPa) than the poor slip-rolling resistant coatings (308 GPa, difference of ~9%). For all the coatings the Vickers Hardness HV is in the same range of 2400 to 2500 kp/mm². The elastic work is comparable with the value obtained by using the nanoindometer Fischerscope 100.

The largest difference concerns the tribological tracks. In the case of the high slip-rolling resistant coating, all the values remain stable. As regards the track of a poor slip-rolling resistant coating, the load-depth nanoindentation curve differs from one at the side of the track. Hence the mechanical properties of poor slip rolling resistant coatings do highly decline because of the slip-rolling test.

The QCSM method permits also a depth analysis of the hardness and Young’s modulus (nota: the variations of the curves for measurements situated under 0.05 µm are due to purely measurement artefacts induced by the rounding-off of the indenter extremity). The curves are depicted in the *figures 4.41 and 4.42.* Both poor slip-rolling resistant coatings have the same hardness and Young’s modulus profiles while the high slip-rolling resistant coating has a more constant Young’s modulus along the depth, without an increase at the surface, inducing no gradient in the mechanical properties.

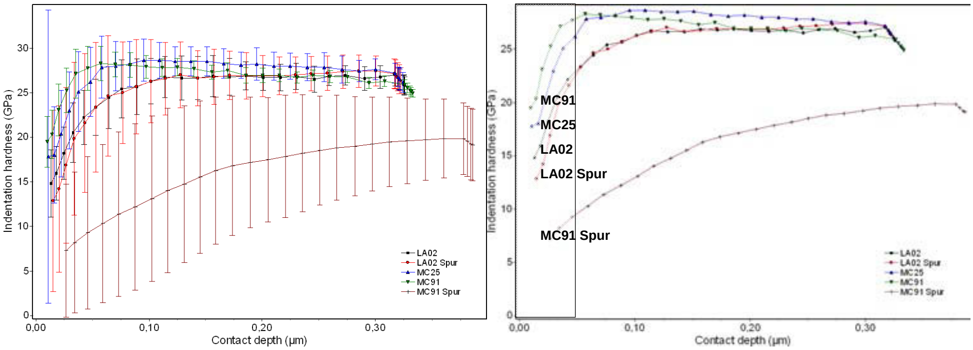

Figure 4.41: hardness depth profile obtained in QCSM modus (left with error bars, right without error bars)

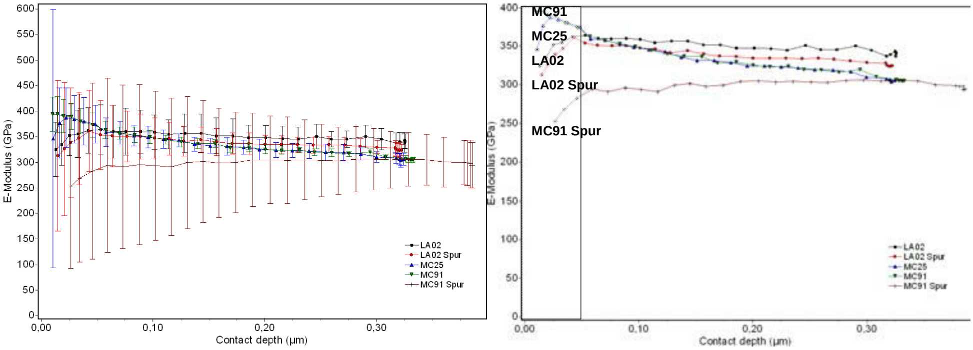

Figure 4.42: Young’s modulus depth profile obtained in QCSM modus (left with error bars, right without error bars)

5 Tribological considerations

In addition to the testing of Zr(C,N) coatings under slip-rolling at high Hertzian pressures, similar experiments were carried out with DLC (Diamond Like Carbon) coatings of different categories, designated and classified following the nomenclature of the report VDI 2840 [VDI05]. The same testing procedure as for the Zr(C,N) coatings was applied in order to compare their respective tribological performances. For comparison and homogeneity reasons, only the slip-rolling resistant DLC coatings are presented here. Since these coatings have also reached the upper limit of 10 millions cycles without fulfilling the aforementioned fixed damaging criterion, other criteria should be introduced in order to differentiate their performance. The tribological quantities measured during and after the tests, i.e. friction and wear, will be compared with those measured with the best Zr(C,N) coating batch. Basically, three kinds of DLC coatings (*Tab. 5.1*) displaying a high slip-rolling resistance were tribologically stressed:

- ta-C, tetrahedral hydrogen free amorphous carbon film characterized by a high stiffness (i.e. very high young modulus) and high hardness, mostly due to the high content of C-C bonds presenting a sp^3 hybridization (Diamond contains 100% sp^3 bonds).

- a-C, hydrogen free amorphous carbon film similar to the ta-C. This coating type contains no hydrogen but a higher content of sp^2 hybridized bonds, making it softer.

- a-C:H:N, coating similar to a-C, but contains a certain hydrogen percentage and is doped with nitrogen.

Table 5.1: Properties of the DLC coatings used for comparison of tribological performances

Parameter	ta-C		a-C		a-C:H:N
Film thickness	2.0 µm		2.0 µm		3.9 +/- 0.14 µm
Young's modulus	432 GPa (ASMEC nanoindenter)		204 GPa (ASMEC nanoindenter)		204 ± 15.7 GPa
Hardness	54 GPa		19 GPa		23.6 ± 3.3 GPa
Film stress	-3.1 GPa		-0.17 GPa		-
Critical load L_{C1} (scratch-test)	22 N		35 N		-
Substrate	Cronidur 30		Cronidur 30		Cronidur 30
Coating state	As Deposited	Polished	As Deposited	Polished	As Deposited
R_a (C.L.A.)	0.28 µm	0.011 µm	0.22 µm	0.009 µm	0.01 µm
R_z	2.37 µm	0.083 µm	1.86 µm	0.065 µm	0.06 µm
R_{pK}	0.73 µm	0.013 µm	0.64 µm	0.010 µm	0.010 µm
R_q	0.38 µm	0.015 µm	0.31 m	0.011 µm	0.014 µm

5.1 Zr(C,N) vs. hydrogen free amorphous carbon coatings in unaddivated paraffin oil at room temperature

The results of the slip-rolling resistance of ta-C and a-C coatings are presented in Figure 5.1 in the same manner as previously for the Zr(C,N) coatings. The DLC coatings presented here belong to the ta-C and a-C categories and were tested mainly in paraffinic oil. They are slip-rolling resistant at room temperature in the range of P_{0mean} = 1.5 GPa – 1.94 GPa. They are as resistant as the best Zr(C,N) coating of the first batch in the test field mentioned. The initial and final coefficients of friction are comparable. However the tests of these carboneous coatings in motor oil at 120°C are unsatisfying since no coating reaches 10 millions cycles. The a-C_3 coating seems to perform better during the severe test at 120°C if deposited on Cronidur 30 (such as the Zr(C,N) coating) than deposited on 100Cr6H.

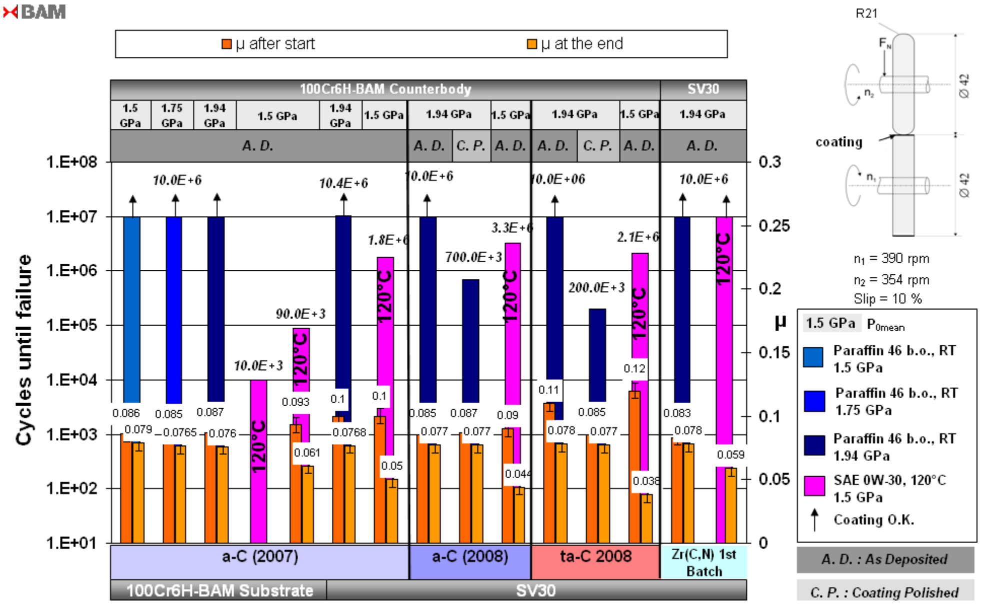

Figure 5.1: Slip-rolling results obtained with ta-C and a-C coatings

It must be noticed that both hard carbon coatings exhibited a high initial roughness (*Tab. 5.2*) of R_a ~ 0.22 - 0.57 µm due to the deposition process, leading to an intense and fast running-in during the first 2.000 cycles. In order to decrease this intense wear of the uncoated steel counterpart induced during the running-in phase, an additional mechanical polishing step, performed using brushing technique, (labelled as “c.p.” – coating polished - in *Fig. 5.1*) of the coatings down to R_a ~ 0.01 µm was introduced to reduce the roughness. Unfortunately (as previously noticed for the Zr(C,N)) this always shortened drastically the slip-rolling resistance of the coating.

Table 5.2: Roughness of the "as deposited" and polished coatings

Rugosity	**ta-C**		**a-C_3**		**Zr(C,N)**		**Zr(C,N) batch #1**
	As Deposited	Polished	As Deposited	Polished	As Deposited	Polished	As Deposited
Ra [µm]	0.3	< 0.02	0.25	< 0.02	> 0.1	0.01	0.05
Rz [µm]	2.4	< 0.2	1.9	< 0.2	> 1.1	0.05	> 1.5

Because of the unsatisfying slip-rolling resistance of Zr(C,N) coatings produced during the successive batches, the poor slip-rolling resistant Zr(C,N) coatings were mechanically polished by the producer with the expectation of an improvement since droplets were removed. The mechanical polishing has disastrous consequences on the slip-rolling resistance of thin film coatings. It is believed that it creates surface defects. The good results in paraffinic oil at room temperature of the a-C and ta-C coatings in their as deposited state could no longer be achieved in their polished state. It must be mentioned that globally the a-C variant seems more slip-rolling resistant than the ta-C coating. The polishing seems to influence less the performances as well as test results are better at 120°C.

In the case of the Zr(C,N) the lifetime is also shortened with a slight change in the friction behaviour (*Fig. 5.2*).

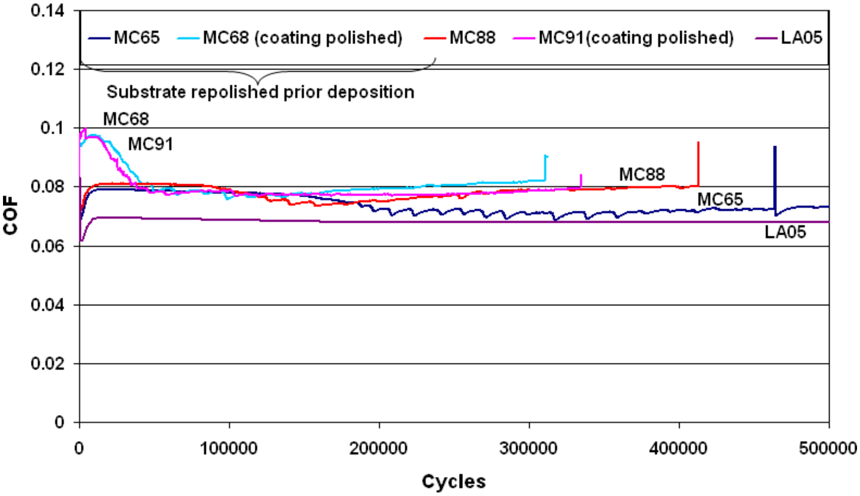

Figure 5.2: Examples of friction curves for the Zr(C,N) coatings

Aside from the comparable friction behaviour of all the thin film coatings, the ta-C, a-C and Zr(C,N) and with similar slip-rolling resistance at room temperature in unadditivated paraffinic oil, another tribological criterion should be taken into account, the wear of the whole system as criterion of protective function aside the criterion of load carrying improvement. The wear of the coating and uncoated counterbody after 10 millions cycles is presented in *Table 5.3*. The average worn surface in cross section *Wq* measured by profilometry along the transverse direction of the tribological track on four positions spaced at an angle of 90° permits the calculation of the wear coefficient k_V following the equation 5.1:

$$k_V = \frac{V}{F_N.L} = \frac{Wq \cdot 2\pi r}{F_N \cdot n \cdot 10\% \cdot 2\pi r} \tag{5.1}$$

with V the worn volume, F_N the applied normal force and L the distance run under sliding. Due to the low depth of the track, the wear volume is equal to the planimetric wear surface Wq multiplied by the sample circumference. It is noteworthy that the high slip-rolling resistant Zr(C,N) coating generates the lowest wear on the uncoated steel counterpart. Additionally the wear of the Zr(C,N) coating after 10 millions cycles is also the lowest compared to the one of the a-C and ta-C coatings (*Tab. 5.3* and *Fig. 5.3*). In the case of the hard carboneous coatings the high wear of the counterpart inducing a change of the contact geometry could decrease the applied Hertzian contact pressure. Regarding to this, the Zr(C,N) can be designated as most slip-rolling resistant.

Table 5.3: Comparison of wear coefficient of different tribosystems after 10 millions cycles at P_{0mean} = 1.94 GPa in unadditivated paraffinic oil at RT

After 10 Mio. cycles	**k_V coating [mm³/N/m]**	**k_V uncoated counterbody [mm³/N/m]**
ta-C on Cronidur 30	$5.2\ .10^{-10}$	$1.3\ .10^{-8}$
a-C on Cronidur 30	$3.2\ .10^{-10}$	$1.4\ .10^{-9}$
Zr(C,N) on Cronidur 30	$1.0.10^{-10}$	$5.1\ .10^{-10}$

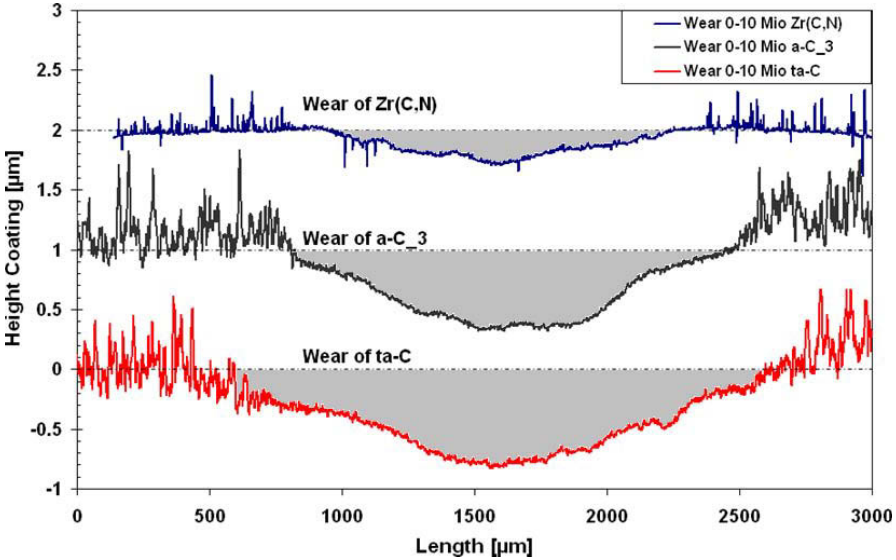

Figure 5.3: Profilometric traces of the coated samples after 10 millions cycles at P_{0mean} = 1.94 GPa in unadditivated paraffinic oil at RT

5.2 ZrCN vs. a-C:H:N in factory fill motor oil SAE 0W-30 at 120°C

Since the ta-C and a-C coatings were only slip-rolling resistant in unadditivated paraffinic oil at room temperature, another DLC coating should be chosen to compare the performance at 120°C in motor oil. This coating belongs to the a-C:H category and displays similar slip-rolling resistance with the best Zr(C,N) coating since it reaches also 10 millions cycles for each test condition (*Fig. 5.4*). It exhibits a substantial advantage, a certain reproducibility occurs batch to batch.

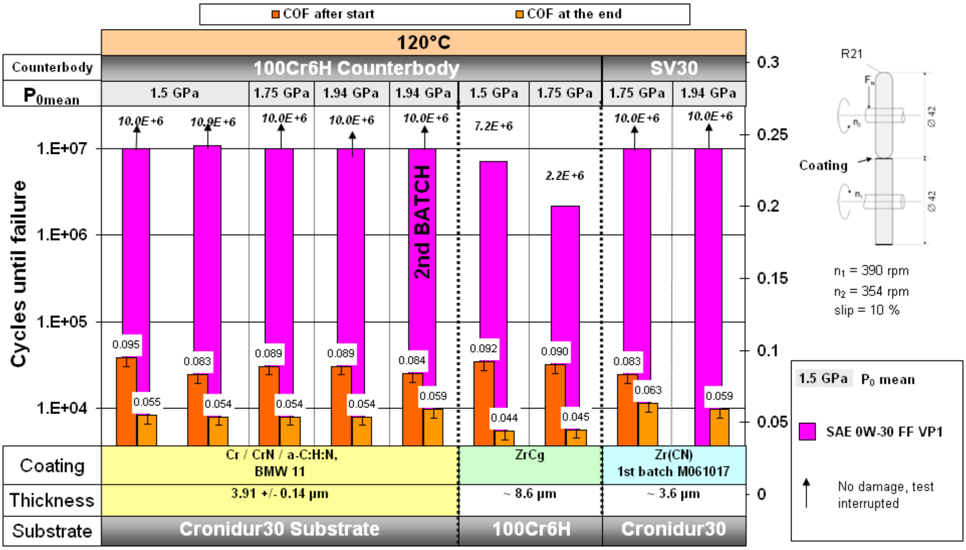

Figure 5.4: Slip-rolling results of BMW-11 a-C:H:N coating and ZrC_g in BMW SAE 0W-30 FF motor oil at 120°C

Another Zr-based coating, ZrC_g, with multilayer structure (*Fig. 5.5*) was also tested in motor oil at 120°C however it do not satisfy the required 10 millions cycles to enter the slip-rolling resistant category. Localized flaking spread all around the circumference of the coating appears after seven millions cycles and 2.2 millions cycles, respectively at P_{0mean} = 1.5 GPa and 1.75 GPa. The surface defects like droplets were identified as starting point of flaking. Hence this coating proves to be sensitive to surface defects generated during the deposition process, what makes it not optimal for high demanding application. The overall results picture invites to the conclusion that deposition of ZrC_g on Cronidur 30 might increase its slip-rolling resistance.

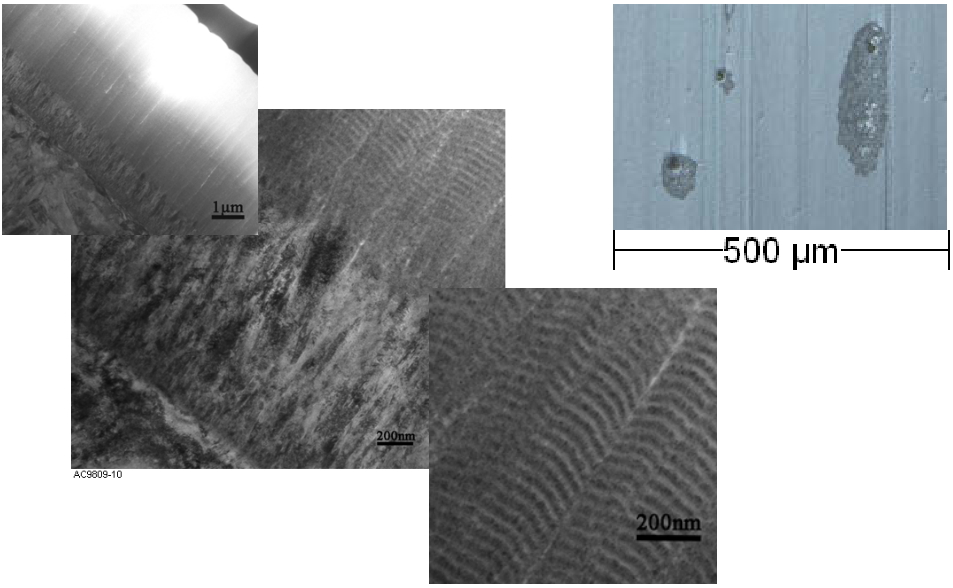

Figure 5.5: TEM pictures of the multilayer ZrC$_g$ (left) and surface defects (darker) causing flaking (top right)

The coefficient of friction (COF) at the end of the test was in all cases nearly constant around 0.05 to 0.06 in mixed/boundary lubrication, the lowest being recorded for the ZrC$_g$ and a-C:H:N coatings. Otherwise the evolution of the COF during the tests conducted at highest Hertzian contact pressure (P_{0mean} = 1.94 GPa) always remains lower than the one of the uncoated configuration “Cronidur 30 vs. 100Cr6H” at a milder average Hertzian contact pressure of P_{0mean} = 1.5 GPa (*Fig. 5.6*). The coating on the cylindrical sample allows a friction reduction of about 20% in the same lubricant and thus under a more than twice higher normal force applied.

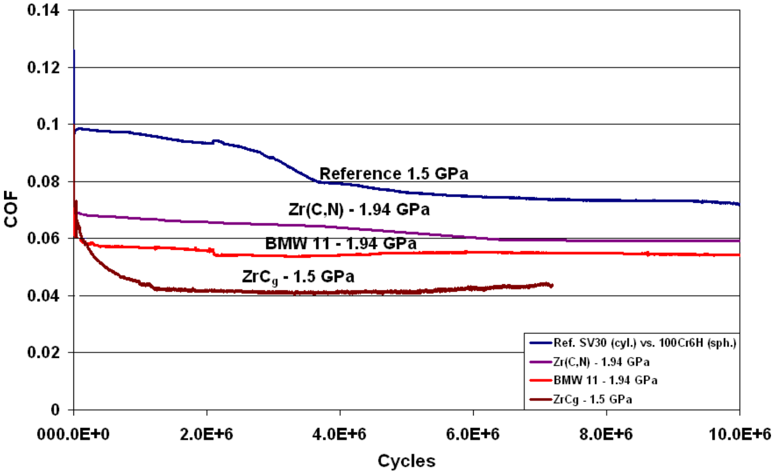

Figure 5.6: Evolution of the COF during tests in BMW SAE 0W-30 FF motor oil at 120°C

Table 5.4: Wear coefficient of different tribosystems in BMW SAE 0W-30 FF motor oil at 120°C after 10 millions cycles

n = 0-10 Mio. cycles	**k_V coating [mm³/N/m]**	**k_V uncoated counterbody [mm³/N/m]**
Cronidur 30 vs. 100Cr6H P_{0mean} = 1.5 GPa	$4.6 .10^{-10}$	$7.5 .10^{-10}$
BMW 11 a-C:H on Cronidur 30 P_{0mean} = 1.75 GPa	$1.3 .10^{-10}$	$3.9 .10^{-10}$
Zr(C,N) 1. Charge on Cronidur 30 P_{0mean} = 1.75 GPa	$1.1.10^{-10}$	$7.0 .10^{-10}$

BMW Factory Filled SAE 0W-30 at 120°C, 10 million cycles		
Cronidur 30 (cyl.) / 100Cr6H (bal.) P_{0mean} = 1.5 GPa $k_V = 4.6.\ 10^{-10}$ mm³/N.m	BMW 11 a-C:H on Cronidur 30 P_{0mean} = 1.75 GPa $k_V = 1.3\ .\ 10^{-10}$ mm³/N.m	Zr(C,N) on Cronidur 30 P_{0mean} = 1.75 GPa $k_V = 1.1\ .\ 10^{-10}$ mm³/N.m

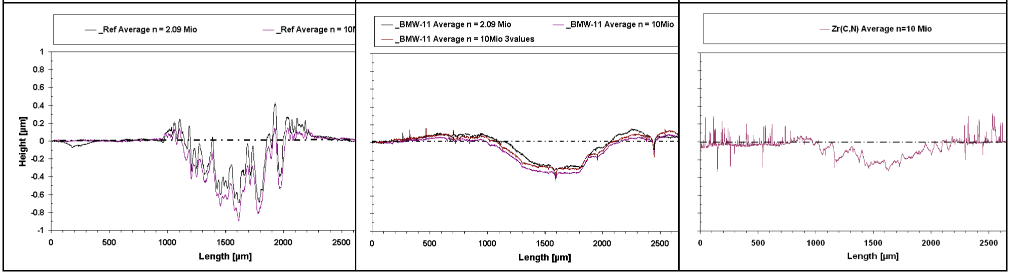

Figure 5.7: Profilometric traces of cylindrical samples after 10 millions cycles (same scale)

The high slip-rolling resistant Zr(C,N) coating and the a-C:H:N coating perform better than the reference couple „cylindrical Cronidur 30 vs. spherical 100Cr6H“ regarding the wear amount after 10 millions cycles (*Tab. 5.4* and *Fig. 5.7*). Contrary to the hard ta-C and a-C coatings, the a-C:H:N exhibits a wear coefficient k_v as low as the one of the Zr(C,N). The wear of the counterpart remains stable, but with the coatings, the wear on the cylindrical part diminishes of a factor 4. The average profile of four single measurements is given for each case in *Figure 5.7*. The plastic deformation of the DLC coating with the substrate is perceptible in form of the raises at the sides of the track. It illustrates the limits of the load carrying capacity of the substrates and the amelioration brought by elastic coatings.

6 Discussion

Figure 6.1 sums up some of the properties of the poor and well performing coatings in form of a radar diagram. The main features concerning the SEM, nanoindentation, XRD and colorimetric characterisations are presented. For comparison purposes, absolute values are displayed on the left and the measurements of the poor slip rolling resistant coating are relatively compared to those of the high slip rolling resistant coating on the right. Here the values of the coating having a high slip resistance are set to 100%. At first glance, the general shape of the poor slip-rolling resistant coating does not significantly deviate from that of the high resistant.

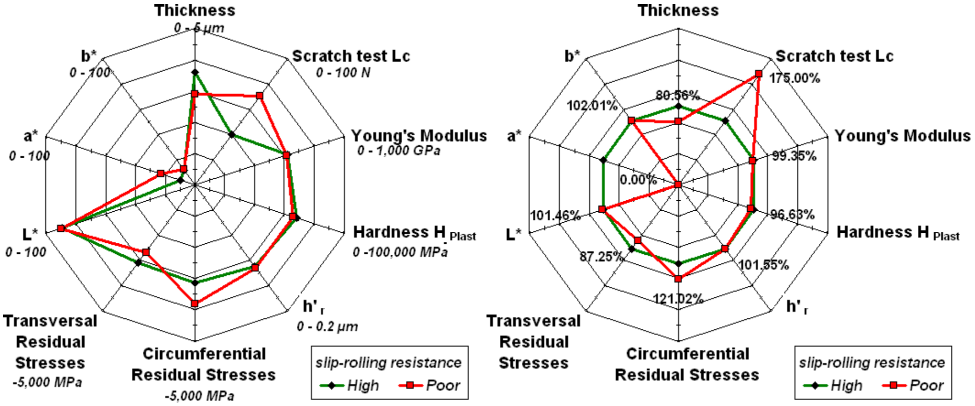

Figure 6.1: Absolute (left) and relative (right) comparison of properties of both coatings from batches #1 and #6 (values of the good coating set at 100% in the relative comparison)

6.1 Surface properties

As previously described, the colorimetry characterisation does not give satisfaction for complying the differences of slip-rolling resistance in spite of the colour difference discernible to the naked eye. The L* a* b* values are too close. A comparison of the whole reflectance spectrum may be much suitable, in order to differentiate the coatings. However deviation may also depend on the surface roughness. Nonetheless roughness values of the coatings were in the same range. (Note: the high deviation of a* in the diagram on the right is due to the absolute value of the high resistant coating which is situated around 0).

Considering at the mechanical properties of the coatings (Young's modulus, remanent deformation after test h'_r, Hardness…) measured by traditional nanoindentation (left side of the diagram), it may be concluded that the slip-rolling resistance does not depend on them as measured with the actual indentation technique. Even the scratch resistance does not justify a difference of slip rolling resistance since the poor slip rolling resistant coating behaves better than the high resistant one. A similar conclusion was found for various DLC coatings subjected to slip-rolling resistance in Benchmark form [to be published]. Different DLC coatings with similar mechanical properties (similar in the way that their values were almost all in the range of the error of measurement and measures were performed under the same measurement conditions), but with different build-up, performed differently under the same slip-rolling conditions. The coating organisation and then its microstructure may be much preponderant than the surface properties measured by traditional nanoindentation.

The nanoindentation can deliver mechanical properties for coatings but here the traditional method is not well adapted for discrediting of coatings stressed under slip-rolling motion. However it should be noticed that the choice of parameters for the measurement may also influence the values, and probably further investigations with different measures parameters should be undertaken and might lead to an other assertion. Anyway, in the current study no difference was found between both Zr(C,N) coatings for parameters of nanoindentation measurements traditionally used for manufacturing and quality control of hard coatings. The slip-rolling resistance might mainly not be governed by the upper surface. However, the QCSM (Quasi Continuous Stiffness) nanoindentation test method permits a better distinction of evolution of mechanical properties with the depth.

6.2 Residual stresses

Concerning the residual stresses of the coatings measured by XRD, an asymmetry in the poor slip rolling resistant coating is noticeable. The high resistant coating contains compressive residual stresses which are well distributed between the circumferential and transverse directions, i.e. almost perfect isotropic (*Fig. 6.1*, diagram on the left). On the contrary all the poor resistant coatings offer higher compressive residual stresses in the circumferential direction and lower compressive residual stresses in the transverse direction. In [THO04], a change of the residual stresses state was reported on the surface of thermally hardened bearing steel 100Cr6 (AISI 52100) between the beginning and the failure of slip-rolling tests with uncoated samples. Depth profiling of the residual stresses from the surface to the bulk (~ 2 mm depth) before the test, after running-in and after failure was carried out by XRD for uncoated 100Cr6 samples subjected to pure rolling under P_{Max} = 3.3 GPa and 3.8 GPa in mixed/hydrodynamic lubrication. Their evolution is represented in *Figure 6.2*.

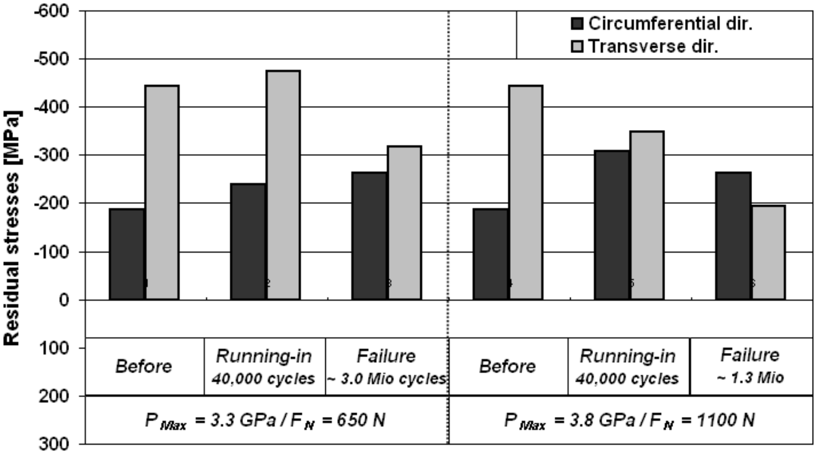

Figure 6.2: Evolution of the residual stress state at an uncoated surface stressed under high Hertzian pressures during pure rolling (original results compiled from [THO04])

Circumferential compressive residual stresses tend to grow and transverse compressive residual stresses tend to decrease at the surface. Then the uncoated surface tends towards a reduced but more isotropic state of its residual stresses during pure rolling motion under high Hertzian stresses. This evolution may favour the opening of cracks at the surface with propagation in the transverse direction, since the compressive transverse residual stresses are reduced and then “looser”, leading to the formation of localized pitting (see *Fig. 4.5*). The crack could find an (additional) activation energy source in the release of the transversal compressive residual stresses.

In the presence of a hard, thin coating, the high initial residual stresses of the surface (around -3,000 MPa) are “substrate and process-related”, i.e. there are two origins of stress in films: thermal and intrinsic residual stresses of the coating. They participate in a certain way in the bonding on the convex substrate surface. High compressive surface residual stresses enable the prevention of crack nucleation and propagation and the parameter that mainly affects crack propagation is just the surface residual stress, the sub-surface trend does not have a great influence on fatigue behaviour [BAR07]. If the surface residual stresses are already isotropic, this stress state could be more stable and might have more difficulty to change (*Fig. 6.3*).

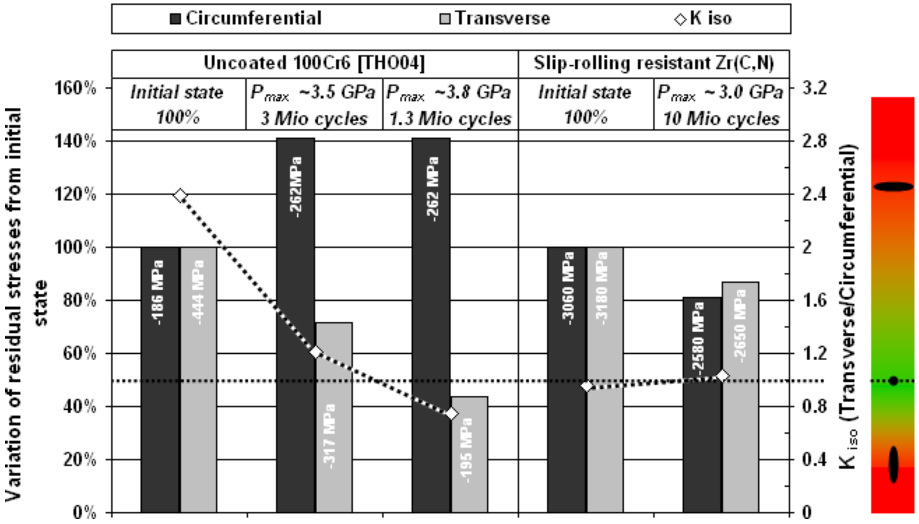

Figure 6.3: Evolution during high Hertzian stressed slip-rolling of the compressive residual stresses for an uncoated 100Cr6 system (pure rolling, left) and for a bearing steel Cronidur 30 coated with a slip rolling resistant Zr(C,N) thin film (10% slip, right)

Introducing K_{iso} as a parameter of isotropy, defined as the ratio between the transverse and the circumferential residual stresses, makes evident that:

- in the case of the uncoated system described in [THO04], K_{iso} tends to decrease around 1 at the failure (when macropitting appears),

- in the case of the undamaged Zr(C,N) coating subjected to 10 millions cycles under similar Hertzian contact stresses, K_{iso} remains stable around 1 in spite of the decrease of the residual stresses.

In a same manner, comparing the initial state of residual stresses of the poor slip-rolling resistant coatings with the initial state of the highest slip-rolling resistant suggests that the initial K_{iso} affects the slip rolling resistance of the coating (*Fig. 6.4*). A starting isotropic state (i.e. K_{iso} around 1) is much favourable for the slip-rolling resistance of the surface.

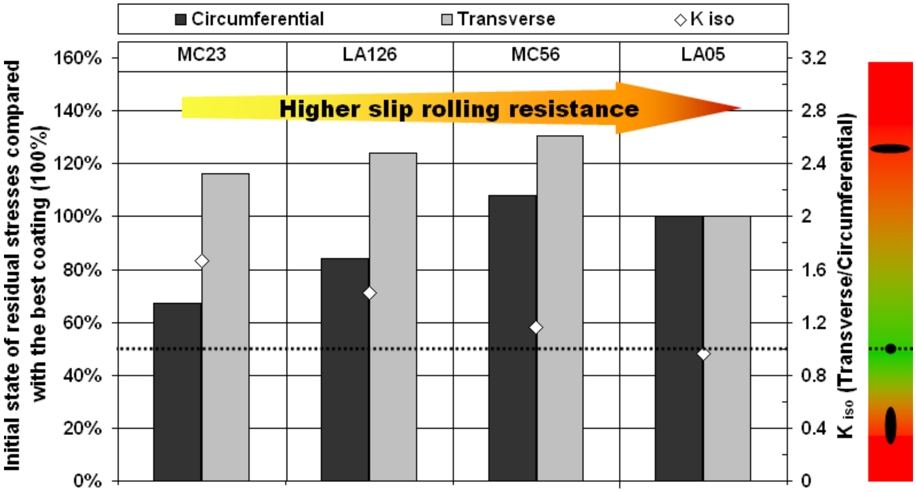

Figure 6.4: Comparison of the initial residual stress state of the Zr(C,N) coatings (best coating standardized at 100%)

6.3 Microstructure

The coatings do not basically differ if only characterized by common techniques as scratch test, nanoindentation or colorimetry, with a slight difference concerning the residual stresses. Therefore, besides the surface residual stress state, coating build-up and microstructure (actually rather nanostructure) may be the critical and main factors in designing a slip-rolling resistant coating.

The coatings of both samples show polycrystalline, columnar growth and consist of a mixture of cubic Zr(C,N) and orthorhombic $Zr_3(C,N)_4$. Both phases co-exist. Zr(C,N) is the most stable phase of the ZrN-ZrC system, which forms substitutional solid solutions whereas Zr_3N_4 is a metastable phase formed at increasing N_2 partial pressure.

The use of EDX in TEM permits to observe a diffusion zone at the substrate/coating interface of about 50 nm wide. Zr ion implantation in the steel substrate due to GD-cleaning, diffusion of Fe towards the interlayer or Zr diffusion towards the substrate may cause the formation of this thin metallurgical interface. Its presence in both high and poor slip rolling resistant coatings cannot explain the difference of slip-rolling resistance.

Nanolayering may improve the slip-rolling resistance by favouring the conservation of residual stresses at the surface i.e. in the coating and hindering crack initiation at the same time. Multilayers cause disruptions of the crystal growth between the layers. It is regularly reported for coated systems stressed under sliding that multilayer coatings perform better than monolithic coatings since they complicate the path of crack propagation through crack splitting [STU09]. Additionally, the nanolayering can create local variations of the residual stresses within the coating at the nanometre scale. However periodically arranged multilayer coatings may also fail, for example, here the graded ZrC_g coating tested was not performing well with regard to the results of the best Zr(C,N) coating. The slip-rolling resistant Zr(C,N) coating displays also a multilayer build-up, but interestingly without "micro" periodicity, i.e. periodicity all along the thickness of the coating. Only a "nano" periodicity is existent and induced by packages formed of periodically alternate nanolayers. This "random organisation" can have an impact on the crack growth too. Stresses leading to the formation of a crack and having a given energetic potential may occur during the tribological stress involving its propagation. If the multilayering is periodically arranged at a constant wavelength and if the crack could already cross the bilayer pattern, it can be supposed that its propagation cannot be stopped on the long term in the case of a repetition of the initiating stress. However if the layers are arranged in periodical packages randomly distributed all along the coating thickness, crack propagation could be stopped or could be slower since the structural arrangement of the coating "constantly" changes all along its thickness. The achievement of slip-rolling tests on Zr(C,N) coatings with process-controlled nanolayering is already under way. First tests show similar results as those accomplished with the best coating presented here. It cannot already be concluded that nanolayering is the major factor ensuring a better slip-rolling resistance but proof is made it participate in it.

The grain size may also play a significant role in the deformation mechanisms of coating materials. The plastic deformation of micro or mesograin (>100 nm) material is based on dislocation slip via slip systems; while for nanograin (<100 nm) material, it was proposed that the dominant deformation mechanisms of thin crystalline films may involve the grain rotation and grain boundary slide [LEY04] since the Hall-Petch hardening mechanisms are expected to be inoperative under a grain size of 20 nm [HUA05]. With insertion of nanolayers in the coating for example formed by a second phase of the material (non-isostructural multilayers), may increase the hindering effect by the occurrence of different dislocation slip systems [YAS99]. The high slip-rolling Zr(C,N) coating contains nanograins under 20 nm and a multilayer structure with multilayers enclosing an orthorhombic $Zr_3(C,N)_4$ phase. The combination of these microstructural features contributes most likely to the slip-rolling resistance.

Hence, diffusion of deposition material in the substrate material is necessary but not sufficient by itself to ensure a certain slip-rolling resistance. The interface should also remain clean in the first phase of the deposition and the process-related interlayer (here made in Zr) must be very thin to reduce the risk of contamination or defect presences. Moreover, unperiodic nanostructuring of the coating by nanolayering is highly beneficial to the slip-rolling resistance and may stabilize an isotropic residual stress state of the nanocrystalline coating.

Because of the presence of droplets on the surface and of the bad consequences of the mechanical polishing on the slip-rolling resistance, it cannot be excluded that these surface defects take part in the initiation of the coating rupture. Supported by the SEM observations, the decrease of the slip-rolling resistance due to mechanical polishing and the conservation of the isotropic equilibrium of residual stresses in the high slip-rolling coating, it is supposed that the droplets are sheared and not detached or extracted from the high slip-rolling resistant coating. The nanolayer structure coupled with the stability of the isotropic residual stresses may produce a “pliers like effect”. This would favour the embedding through homogeneous constriction instead of the total ejection of the droplet through dislodging because of the isotropic change and reduction of residual stresses, displacing the “pliers effect” (i.e. directionless) towards a “vice effect” (unidirectional). The ejection of the droplets would let a cavity wide from a few micrometers where the lubricant could penetrate through wetting, capillarity flow and seepage by the contact pressure alike in fluid-assisted crack growth [LAI09] (if the lubricant remains not too viscous since viscosity increases with pressure…). The lubricant trapped and pressurized would stress the walls of the cavity and the interface by hydraulic pressure provoking the build-up of cracks or flaking.

Moreover, for all the coatings investigated, amorphous DLC or nanocrystalline Zr(C,N), the beginning of flaking starts near surface defects (comparison of light microscopy photographs of the coated sample prior to and after test) and grows in the same direction as the rotation direction of the coated disc. It means a small spall forms and if it has a critical geometry and size, flaking progress when it enters in the contact, i.e. when the edge of the “microdepression” or indent is under tension because of the slower upper disc which tends to brake the lower coated one (see Fig. 6.5). If a droplet is ejected, the coating loses its residual stress state at this location, since there is no more material, and the edges forming the hole are no more stressed. Compressive stresses are not a problem, i.e. at the exit of the contact, since they were constantly under residual compression before the formation of the hole. It seems that edges cannot resist tension.

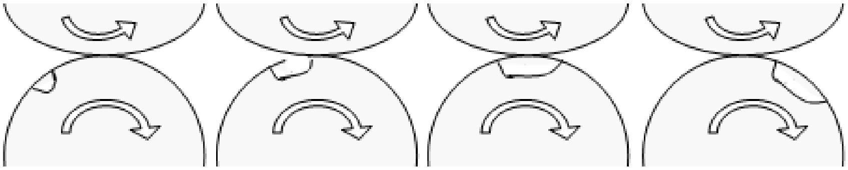

Figure 6.5: Flaking progression at a surface defect on the coating during slip- rolling

6.4 Oxygen in the coating and at the interface

The phase diagram of the Zr-O system shows that already at low temperatures zirconium can absorb up to 10 at.-% of oxygen [LID97]. In different phases of alpha Zr even up to ~28.5 at-% oxygen can be solubilised (*Fig. 6.6*).

Moreover, it is well established that the properties of Zr favours the spontaneous formation of an (natural or native) oxide film because of the high natural affinity of Zr with oxygen in air (formation enthalpy ΔG_{RT} $Zr+O_2 \rightarrow ZrO_2 = -1093$ kJ/mol [TRI94]) alike the formation of a passive layer on Al or Ti, conferring its great resistance to corrosion in alkaline or acid solutions. Therefore metallic zirconium is always covered by a protective oxide film of ZrO_2 [POU66, BON70, AIZ69] and the characteristics of this layer depends strongly on the formation conditions. This oxide layer thickness can reach several nanometres and thus until several hundred nanometres. So the surface of the Zr-target is always in an oxidised state during substrate loading or inasmuch as it is not placed and cleaned under vacuum.

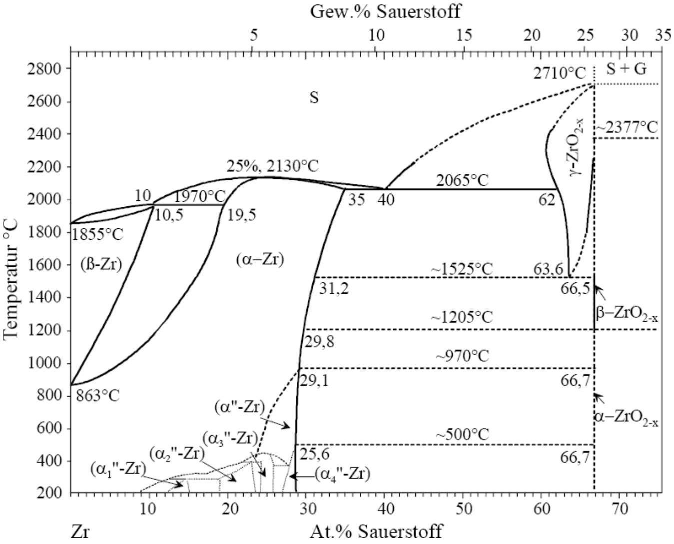

Figure 6.6: Zr – O phase diagram [MAS86]

That is why the Zr target should be free of its oxide skin before:

- starting the GD cleaning,
- the Zr cleaning of the substrates under high polarization and
- the deposition of the coating.

Furthermore oxygen incorporation may also originate from water layer which forms on the cathode surface. This common supposition is often put forward, more particularly in pulsed deposition also working under high vacuum [SAN00]. For the deposition of the poor slip-rolling Zr(C,N) coating, a different configuration was used with more Zr-targets in the deposition chamber, increasing the total content of oxygen, bonded in oxide form on the Zr-targets. These are possible sources for the higher oxygen content at the substrate/coating interface on the poor slip rolling resistant coating.

Furthermore, the Cronidur 30 steel is a stainless steel which means easily passivable. During heating of the substrates in the deposition chamber, desorption of water from the walls take place, favouring the presence of the passivation skin on the substrates. At the start of the Zr-cleaning stage, Zr ions peen on the surface of the substrates placed under high polarization. Chromium oxide Cr_2O_3 and iron oxide Fe_2O_3, constituting the protective oxide layer, have oxide formation lines situated much higher in the Ellingham diagram as the ZrO_2. Therefore it is thermodynamically possible to form ZrO_2 on the substrate surface by reaction of the sputtered Zr-particles with the oxides forming the passivated layer of the Cronidur 30. If the kinetic energy of the Zr ions is high enough, they “derust” the substrate surface (GD-etching) without forming a layer. However a very thin Zr interlayer was found in all the samples, which is unintentionally formed indeed, perhaps due to a too high Zr flow which saturates the substrate surface. An insufficient kinetic energy could be excluded since a diffusion zone of Zr in the substrate was found, zone possibly formed by ion implantation due to the high initial bias. Because of the high reactivity of zirconium with oxygen compared to nitrogen [OHR92], the “Zr interface” should be as thin as possible to avoid the formation of ZrO_2 and also because the probability of presence of any critical defects is higher in a thick interlayer than in a thin one.

To compete with residual O_2 present in the deposition chamber, it may be interesting to introduce a small amount of Nitrogen in Argon during the first process step. Only a small amount of N_2 would induce an immediate high N/O ratio in the plasma and hinder the formation of ZrO_2. Moreover, in [VAZ04] a preferential resputtering of oxygen due to a lower bond strength of Zr-O compared to Zr-N is proposed to explain oxygen loss under increasing ion bombardment (i.e. high bias) in reactive rf magnetron sputtering deposition of ZrN_xO_y thin films in mixed atmospheres composed of Ar, N_2 and O_2. In any case a high N/O ratio is needed since reactive sputtering of metallic zirconium in N_2-O_2 atmosphere with a nitrogen content of 80 % already produces pure films of monoclinic ZrO_2 [MAT04] and 3 sscm of O_2 in a mixture of Ar (10.4 sccm) and N_2 (17.5 sccm) formed ZrO_2 nanograins during ion plating deposition of a $ZrN_{0.74}O_{0.19}$ [HUA07]. But adding oxygen during the deposition phase could permit to tune the nanolayer formation too, since formation of poorly crystallized oxygen-doped orthorhombic, Zr_3N_4-type structures is often reported with the possibility of coexistence of different phases since the increase of oxygen fraction induces the formation of new structural arrangements [MOU06, FER06]. Raman spectrometry or resistivity measurements could detect those since first order Raman scattering is forbidden in the sodium-chloride-type structure for an ideal “perfect” crystal [MOU06] and Zr_3N_4 is more insulating than ZrN.

Then as far as possible, the cleaning of the Zr-target should be undertaken with substrates protected from the particles flow extracted from the target at the ignition of the arc or perhaps with a filter or “polarized waste absorber” (i.e. a part in the chamber with a higher potential than the substrate polarization which would capture impurities coming from the Zr-target during its cleaning). To prepare ZrN films, very careful control of the gas flow rates is needed since the final properties will depend much on the atomic ratios, and oxygen exhibits a stronger reactivity than nitrogen with transition metal like Ti or Zr [MAR01].

6.5 Formation of the nanolayers and of Zr_3N_4

It can be thought that one single active Zr-target (or a single Zr target “wall”) induces a possibility of a gradient of the Zr particles flow in the deposition chamber because of a shadowing effect engendered by the substrates themselves on the carrousel combined with an increasing distance to the target during the rotation. As consequence a variation of the N/Zr ratio during the growth of the coating can result. It is highly plausible since in [PIC99] a model for growth mechanism of over-stoechiometric nitrides is proposed and based on the analysis of the Zr and N flows during Dual Ion Beam Sputtering (DIBS). Here is highlighted competition between sputtering effect due to increase of ion bombardment energy, diffusion and implantation. As the WDX analyses display an average N/Zr ratio near 1.2, a slight slide in direction of an atmosphere richer in nitrogen or a higher N flow than the Zr flow could provoke the formation of a Zr_3N_4 phase (theoretic N/Zr ratio = 1.33), and thus in an alternating manner. In this way the formation of multilayers, observed with TEM, could be favoured, only due to the motion of the samples in the chamber during deposition. The irregular distribution of the multilayers packages could result of an inconstant rotation speed of the samples during coating deposition. Effectively in Multi-arc deposition of Ti-Zr-N coatings, it was demonstrated in [WAN06] that architecture (and therefore mechanical properties) can be tailored as a result of rotation speed only.

6.6 Way towards surface functionalization for environment-friendly lubricants?

Alike for titanium, by water or steam oxidation, zirconium forms zirconia and hydrides on its surface. The possibility of formation of hydroxides or pseudo-hydroxides on TiO_2 was also proved by molecular dynamics calculations [LIN96]. It is believed that ZrO_2 (and also Al_2O_3 or MgO) may possess such abilities too. The formation of hydroxylated Zr species on ZrO_2 was verified and it was advanced hydroxide formation was responsible of the dramatic reduction of friction and wear with the increase of air humidity from 5% RH to 50% RH and 90% RH [BAS00] because zirconium hydroxide has a layer structure which promote lower friction and wear [SHI00]. The formation of $Zr(OH)_4$ on ZrO_2 was also experimentally assessed during sliding in steam at 400°C [KLE04].

The ZrCN coating seems also to form oxides on its surface during the slip-rolling test, as surface analysis by EDX shows a great amount of oxygen in the tribological track. Then the possible Zr(C,N) -> ZrO_2 -> $Zr(OH)_4$ transformation steps on the coating surface may represent a way towards functionalization of the coating surface trough triboreactions. Moreover it is well known that lubricants suffer under degradation due to acidification (increase of TAN, Total Acid Number) and increasing water content absorbed from the surrounding environment through condensation for example (hydrolysis risk of synthetic oils). Due to its high corrosion resistance, the coating could also “compensate” this deterioration of the lubricant without risk for the base material.

It is known that organophosphonates display strong interactions with titanium but also many other transition metals (such as niobium, tantalum, zirconium, as well as aluminium). In [ZOU06] it was shown that PEG-ylated compounds carrying phosphonate groups, known for their affinity toward titanium oxide surfaces, were formed in stable monolayers on TiO_2 (*Fig. 6.7*). If these layers are thermal resistant, this make conceivable the development and the use of new lubricants based on polyglycols which could functionalize the coating during the tribological loading and then opening the way towards lubrication without use of harmful additives, since the coating resists in unadditivated and non-polar paraffinic oil.

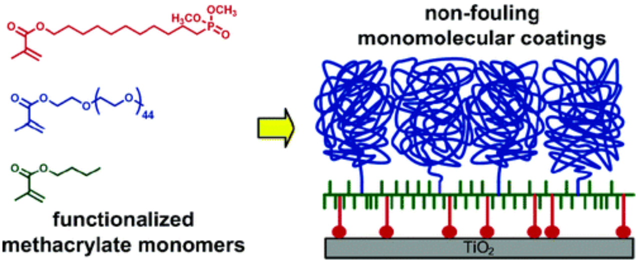

Figure 6.7: Functionalization of a TiO_2 surface with PEG chains [ZOU08]

7 Conclusion and outlook

This work firstly demonstrates that coatings are able to increase the load carrying capacity of steel used as substrate, namely the Zr(C,N) coating on Cronidur 30, and thus allowing an increase of the carried normal force of more than a factor 2 in the range of 10 millions cycles in mixed/boundary lubrication. The Zr(C,N) coating is also able to sustain a working temperature of motor oil in the range of 120°C without dehydrogenation on long-term, in contrast to DLC coatings. Furthermore, Zr(C,N) coatings can offer a friction reduction of 20% in mixed/boundary lubrication compared to uncoated steel/steel contact stressed under a twice lower normal force, without the additional development of new lubricants. This can be advantageous since competitive pure DLC coatings may require a metal doping or a lubricant customization because they are mostly reported to be inert and hence do not react well with conventionally additives used for motor oil formulation.

Mechanical polishing of coatings after deposition was ineffective since a catastrophic decrease of the slip-rolling resistance was revealed. Certainly it removes droplets and smoothens the surface but it creates defects and it is supposed that it influences badly the residual stresses at the surface. However, a potential towards the resistance of the Zr(C,N) coating at higher Hertzian contact pressures P_{max} = 3.5 GPa is conceivable making downsizing of highly loaded components to come into reach. Actually, the next step should be the use of a rough surface with oriented machining scores before coating deposition in spite of an ideal superpolished surface. It would be more representative of the surface texture typically generated in mass production of gears. Such a decisive step requires not only a slip-rolling resistant coating but also a coating insensitive to surface defects generated before (for example, grinding scores) during (for example, droplets) and after deposition (i.e. indents). In the same time, start-stop tests under high Hertzian contact pressures are needed since the lubrication is the most minimal in such cases.

New results concerning the understanding of the slip rolling resistance of thin film coatings based on a nanocrystalline microstructure could be achieved. The superiority of multilayer based coatings is known for sliding operations but few research results concern (slip) rolling, especially in the mixed/boundary regime. Contrary to amorphous coatings (for example DLC coatings), the crystalline state of the Zr(C,N) coatings investigated here makes them accessible to and more suitable for actual microstructural characterisation techniques, permitting a better approach of the parameters influencing the resistance of the coatings operating in rolling motion combined with slip and high Hertzian contact pressures. For example, changes in the residual stresses of amorphous DLC coatings cannot be investigated by XRD and their determination after testing under slip-rolling is impossible with the beam-bending technique since its principle of measurement requires plane coated samples.

Taking care on coating build-up and residual stresses is also highlighted. Coating build-up, microstructure and residual stresses may be the major parameters driving the slip-rolling resistance. Since the single difference in the deposition of the Zr(C,N) coatings was the use of a machine equipped with one single or two zirconium targets, the “constellation” of the deposition parameters should therefore not only contain the parameters traditionally taken into account like gas pressure (or gas flow), temperature, substrate polarization or current but also the motion of the substrate in the deposition chamber during the deposition and the number of the targets as well as their relative position to the substrate. Indeed it is assumed that those two parameters allow the formation of a nanolayered coating when other parameters are preserved constant. Additionally it also highlights the problem of process upscaling in the technology transfer of coating deposition, particularly for the final purpose of high demanding applications. Microstructural features summed up in *Table 7.1* suggest that diffusion of deposition material in the substrate material is necessary but not sufficient by itself to ensure a certain slip-rolling resistance. The interface should also remain clean in the first phase of the deposition and the process-related interlayer (here made in Zr) must be very thin to reduce the risk of contamination or defect presences. Moreover, unperiodic nanostructuring of the coating by nanolayering is highly beneficial to the slip-rolling resistance and may stabilize an isotropic residual stress state throughout the nanocrystalline coating.

Table 7.1: Summary of the main microstructural differences stated between high and poor slip rolling resistant coatings.

Slip rolling resistance > 10^7 cycles	**Slip rolling resistance < 5 . 10^5 cycles**
Multilayer structure	Monolithic structure
Coatings with nanolayers under 5 nm	No nanolayers
Nanolayers arranged in packets	-
Unperiodic distribution of ordered packets along the depth	-
Small size of nanocrystallite	Nanocrystallites of bigger size
Thin transition between substrate and coating of about 50 nm	“Thicker” transition between substrate and coating of about 160 nm
Clean interface	Interface with high oxygen content
Low oxygen content and well distributed	Oxygen in the coating but with high concentration at the interface between substrate and coating
“Isotropic” compressive residual stresses	“Anisotropic” compressive residual stresses
Stability of the compressive residual stresses up to 200°C	Modification of the compressive residual stresses with the increase of the temperature

In addition to the increase of the load carrying capacity, first criterion to be fulfilled (necessary condition), coatings should allow a wear reduction of the whole system (not only of the coated surface) or/and a global friction reduction. These both considerations should be used as secondary criteria (sufficient condition) to define the protective function and the frictional function. The testing conditions chosen here are extreme and permit a clear differentiation of the thin film coatings, that, as shown, other traditional coating characterization methods cannot offer for the moment, although new nanoindentation technique like QSCM may establish small differences.

Moreover, a need in standardization of testing method for coatings subjected to (slip)-rolling motion and high Hertzian stresses is well-founded as it is almost impossible to compare tribological results in the literature if they are obtained under different conditions, contact geometry and lubrication regime being of importance (without bringing up the deposition technique of the coating including additional parameters). With the constant improvement of the coating performances, it would be interesting to develop a norm with coated discs (that have the advantage to be cost-saving). It could mix long time test at a constant Hertzian pressure and step-load test with a specified steel substrate at a given finishing (such as in the ISO 14635-1) and in unadditivated oil. The chosen steel should be able to withstand different deposition methods. Considerations on improvements of load carrying capacity, wear and friction would constitute the fundaments to evaluate the efficiency of coatings.

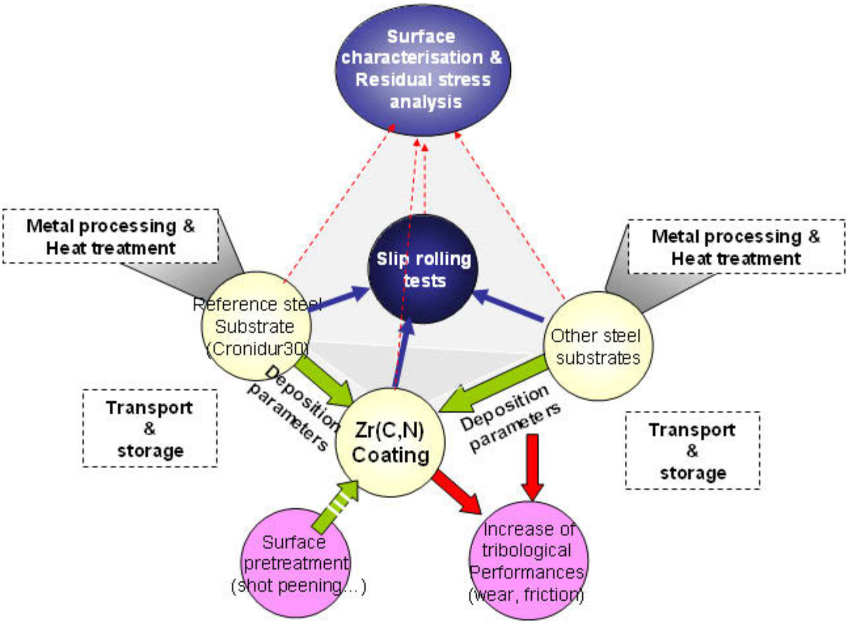

Figure 7.1: Perspective of possible future work on Zr(C,N) coatings

For an enhanced understanding and designing of coatings adapted to applications working with slip-rolling, the whole background of the substrate must be known, from its production to its forming and finishing (*Fig. 7.1*). The whole supply chain must be understood, under control and stable to allow technologic transfers. To surpass the tribological results presented, i.e. to reach even higher Hertzian contact pressures, it would be necessary to choose special steels to avoid the failure of the substrate and to permit a higher load carrying capacity of the “coating/substrate” system under such extreme conditions.

8 References

[ABA08] Abadias G.: *Stress and preferred orientation in nitride-based PVD coatings*, Surface & Coatings Technology 202 (2008), pp. 2223–2235

[AHL08] Ahlroos T., Ronkainen H., Helle A., Parikka R., Virta J., Varjus S.: *Improvement of micropitting performance of power transmission gears*, Proceedings of the 3rd Nordic Symposium on Tribology, Nordtrib2008 (2008).

[AHM01] Ahmed R., Hadfield M.: *Influence of coating thickness and contact stress on the fatigue failure of HVOF coatings*, Proceedings of the International Thermal Spray Conference, Singapore (2001), pp. 1009–1015.

[AIZ69] Aizullin F. F., Mazurenko N. D.: Issled. Electrokhim., Magnetokhim. Metod. Anal. 2 (1969), p. 136.

[ALE93] Alexandre N., Desmaison-Brut M., Valin F., Boncoeur M.: *Mechanical properties of hot isostatically pressed zirconium nitride materials*, Journal of Marterials Science (1993), pp. 2385-2390.

[ALL00] Allenbach C. P.: *MOCVD and tribological properties of thin zirconium carbonitride films*, Dissertation ETH No. 13832, Zurich 2000.

[AMA05] Amaro R.I., Martins R.C., Seabra J.O., Renevier N.M., Teer D.G.: *Molybdenum disulphide/titanium low friction coating for gears application*, Tribology International, 38 (2005), pp. 423-434.

[AND81] Andrievskii R. A.: *Current state of investigations concerning the properties of transition metal nitrides*, Translated from Poroshkovaya Metallurgiya 3 (219), (1981), pp. 77–87.

[ARI06] Arias D.F., Arango Y.C., Devia A.: *Study of TiN and ZrN thin films grown by cathodic arc technique*, Applied Surface Science 253 (2006), pp. 1683–1690.

[BAD98] Bader M., Spies H. -J., Höck K., Broszeit E., Schröder H. -J.: *Properties of duplex treated (gas-nitriding and PVD -TiN, -*Cr_2N*) low alloy steel*, Surface and Coatings Technology 98 1-3 (1998), pp. 891-896.

[BAL05] Balaceanu M., Braic M., Braic V., Pavelescu G.: *Properties of arc plasma deposited TiCN/ZrCN superlattice coatings*, Surface & Coatings Technology 200 (2005), pp. 1084– 1087.

[BAR07] Baragetti S.: *Fatigue resistance of steel and titanium PVD coated spur gears*, International Journal of Fatigue 29 (2007), pp. 1893–1903.

[BAS00] Basu B., Vitchev R. G., Vleugels J., Celis J. P., Van der Biest O.: *Influence of humidity on the fretting wear of self- mated tetragonal zirconia ceramics*, Acta materialia 48 (2000), pp. 2461-2471.

[BAT99] Batchelor A. W., Lam L.N., Chandrasekaran M.: *Materials degradation and its control by surface engineering*, Imperial College Press, London (2002).

[BAU96] Baur W.H., Lerch M.: *On deciding between space groups Pnam and Pna21 for the crystal structure of* Zr_3N_4, Zeitung für anorgische und allgemeine Chemie 622 (1996), pp. 1729-30.

[BEN02] Benia H, Guemmaz M, Schmerber G, Mosser A, Parlebas J.-C.: *Investigations on non-stoechiometric zirconium nitrides*, Applied Surface Science 200 (2002), pp. 231-238.

[BIE05] Bielawski M., Seo D.: *Residual stress development in UMS TiN coatings*, Surface & Coatings Technology 200 (2005), pp. 1476–1482.

[BIN95] Binder S., Lengauer W., Ettmayer P., Bauer J., Debuigne J., Bohn M.: *Phase equilibria in the systems Ti-C-N, Zr-C-N and Hf-C-N*, Journal of Alloys and Compounds 217 (1995), pp. 128-136.

[BIT63] Bittner H., Goretzki H., Benesovsky F., Nowotny H., *Über einige Monocarbid--Mononitrid-Systeme und deren magnetische Eigenschaften,* Monatshefte für Chemie 94 (1963), p. 518.

[BON70] Bondareva T. P., Novakovskii V. M., Zashch. Metal 6 (1970), p. 207.

[BOO97] Booser E. R.: *Tribology Data Handbook*, CRC Press, Boca Raton (1997).

[CAL08] Callaghan, R. (2008-02-21): *Zirconium and Hafnium Statistics and Information*, US Geological Survey, http://minerals.usgs.gov/minerals/pubs/commodity/zirconium/. Retrieved on 2008-02-24.

[CAV05] Carvalho P., Vaz F., Rebouta L., Cunha L., Tavares C.J., Moura C., Alves E., Cavaleiro A., Goudeau Ph., Le Bourhis E., Rivière J.P., Pierson J.F., Banakh O., *Structural, electrical, optical, and mechanical characterizations of decorative* ZrO_xN_y *thin films*, Journal of Applied Physics 98 (2005), 023715 pp. 1-8.

[CHA90] Chang T. P., Cheng H. S., Sproul W. D.: *The influence of coating thickness on lubricated rolling contact fatigue life*, Surface Coatings Technology 43-44 (1990), pp. 699-708.

[CHA91] Chang T. P., Cheng H. S., Chiou W. A., Sproul W. D.: *A comparison of fatigue failure morphology between titanium-nitride-coated and uncoated lubricated rollers*, Tribology Transactions 34 (1991), pp. 408-416.

[CHE02] Chen Y.-H., Polonsky I.A., Chung Y.-W., Keer L. M., *Tribological properties and rolling-contact-fatigue lives of TiN/SiNx multilayer coatings*, Surface and Coatings Technology 154 (2002), pp. 152–161.

[CHE05] Chen C.-S., Liu C.-P., *Diffusion barrier properties of amorphous ZrCN films for copper metallization*, Journal of Non-Crystalline Solids 351 (2005), pp. 3725–3729.

[CHE90] Cheng H. S., Chang T. P., Sproul W. D.: *A morphological study of Contact fatigue of TiN Coated Rollers,* in Proc. 16th Leeds/Lyon Conf. on Tribology, 1989, Tribology Series 17, Elsevier, Amsterdam, 1990, p. 81.

[CHH05] Chhowalla M., Emrah Unalan H.: *Thin films of hard cubic* Zr_3N_4 *stabilized by stress*, Nature Materials 4 (2005), pp. 317-322

[CHR75] Christensen A. N.: *A Neutron Diffraction Investigation on Single Crystals of Titanium Carbide, Titanium Nitride, and Zirconium Nitride,* Acta Chemica Scandinavica A29 (1975), pp. 563-568.

[CHR77] Christensen A. N., Fregerslev S.: *Preparation, Composition and Solid State Investigations of TiN, ZrN, NbN and Compounds from the Pseudobinary Systems NbN-NbC, NbN-TiC and NbN-TiN***,** Acta Chemica Scandinavica A31(1977), pp. 861-868.

[CUN06] Cunha L., Vaz F., Moura C., Rebouta L., Carvalho P., Alves E., Cavaleiro A., Goudeau Ph., Rivière J.P.: *Structural evolution in* ZrN_xO_y *thin films as a* *function of temperature*, Surface & Coatings Technology 200 (2006), pp. 2917– 2922

[CZI03] Czichos H., Habig K.-H.: *Tribologie-Handbuch,* 2nd edition, Vieweg Verlag, Wiesbaden (2003)

[DEM89] Desmaison-Brut M., Themelin L., Valin F., Boncoeur M.: *Mechanical Properties of Hot-Isostatic-Pressed Titanium Nitride*, Euro-Ceramics 3 (1989) pp. 258-262.

[DIL84] Dill J.F., Gardos M.N., Hintermann H.E., Boving H.J.: *Rolling Contact Fatigue Evaluation of Hardcoated Bearing steels*, ASCE Publication (1984), pp. 230–240.

[DOW77] Dowson D., Higginson G. R.: *Elasto-hydrodynamic Lubrication*, Pergamon Press, Oxford (1977).

[DZI07] Dzivenko D. A., Zerr A., Bulatov V. K., Miehe G., Li J., Thybusch B., Brötz J., Fueß H., Brey G., Riedel R.: *High-Pressure Multianvil Synthesis and Structure Refinement of Oxygen-Bearing Cubic Zirconium(IV) Nitride*, Advanced Materials 19 (2007), pp. 1869–1873.

[DZI09] Dzivenko D. A.: *High-pressure synthesis, structure and properties of cubic zirconium(IV)- and hafnium(IV) nitrides*, Dissertation Darmstadt (2009).

[ENE03] Energietechnik Essen Datenblatt 01.12.03, http://www.energietechnik-essen.de/downloads/datenblatt_cronidur_2009.pdf, latest time consulted in november 2009.

[ERD88] Erdemir A., Hochman R. F.: *Surface metallurgical and tribological characteristics of TiN-coated bearing steels*, Surface and Coatings Technology 36 3-4 (1988), pp. 755-763.

[ERD88-2] Erdernir A., Hochman R. F., in R. F. Hochman, H. Legg and K. O. Legg (eds.), Proc. Conf. Ion Implantation and Plasma Assisted Processes for Industrial Applications, ASM, Metals Park, OH, 1988, p. 43.

[ERD92] Erdemir A.: *Rolling-contact fatigue and wear resistance of hard coatings on bearing steel substrates*, Surface and Coatings Technology, 54/55[1992) 482-489

[ERD99] Erdemir A.: *Rolling-contact fatigue resistance of hard coatings on bearing steels*, paper presented at the H. S. Cheng Tribology Symposium in conjunction with the 1999 Joint Tnbology Conference of the ASME/STLE, Kissimmee, FL, Oct. 10-14, 1999.

[ESP05] Espinosa I.: *Comparativa entre diferents recobriments decoratius obtinguts per PVD en base Ni i el Cr electrolític*, Universitat Politècnica de Catalunya (2005).

[EVA05] Evans, Ryan D. and Howe, Jane Y., Bentley, James, Doll, Gary L., Glass, Jeffrey T.: *Influence of deposition parameters on the composition and structure of reactively sputtered nanocomposite TaC/a-C:H thin films*, Journal of Materials Research 20 - 9 (2005), pp. 2583 -2596.

[FER06] Ferreira S.C., Ariza E., Rocha L.A., Gomes J.R., Carvalho P., Vaz F., Fernandes A.C., Rebouta L., Cunha L., Alves E., Goudeau Ph., Rivière J.P., *Tribocorrosion behaviour of ZrOxNy thin films for decorative applications*, Surface & Coatings Technology 200 (2006), pp. 6634–6639

[FIL91] Fillit R. Y., Perry A. J., Strandberg C., *X-Ray Elastic Constants, Stress Profiling And Composition Of Physically Vapor Deposited ZrN Films*, Thin Solid Films 197 (1991), pp. 47- 55.

[FRA08] Fragiel A., Staia M.H., Muñoz-Saldaña J., Puchi-Cabrera E.S., Cortes-Escobedo C., Cota L.: *Influence of the* N_2 *partial pressure on the mechanical properties and tribological behavior of zirconium nitride deposited by reactive magnetron sputtering*, Surface & Coatings Technology 202 (2008), pp. 3653–3660.

[FRI97] Friedrich C., Berg G., Broszeit E., Berger C.: *Datensammlung zu Hartstoffeigenschaften*, Materialwissenschaft und Werkstofftechnik 28 (1997), pp. 59-76.

[GAL09] Gallardo E.A., Lewis R.: *Coating and treatment solutions for rolling/sliding component contacts*, Wear 267 (2009), pp. 1009–1021.

[GEN99] Gennadievich V. G., Berns H.: *High nitrogen steels: structure, properties, manufacture, applications*, Springer Verlag, Berlin (1999).

[GOL07] Gold P.W., Loos J., Plogmann M., Ermüdungslebensdauer PVD-beschichteter Wälzlager, Proceeding GfT Tagung 2007 Band II.

[GOR98] Gorokhovsky V.I., Deepak G. B.: *Principles and application of vacuum arc plasma-assisted surface engineering technologies*, International workshop on surface engineering and coatings NAL, Bangalore, India June 25-30 1998, pp. 381-393.

[GU06] Gu J.-D., Chen P.-L.: *Investigation of the corrosion resistance of ZrCN hard coatings fabricated by advanced controlled arc plasma deposition*, Surface & Coatings Technology 200 (2006), pp. 3341 – 3346

[HAD95] Hadfield M., Stolarski T.: *The effect of the test machine on the failure mode in lubricated rollling contact of silicon nitrides*, Tribology International 28 - 6 (1995), pp. 377-382.

[HAM81] Hamrock B.J. & Dowson D.: *Ball Bearing Lubrication, The Elastohydrodynamics of Elliptical Contacts*, John Wiley & Sons, New York (1981).

[HEI08] Heinrich S., Schirmer S., Hirsch D., Gerlach J.W., Manova D., Assmann W., Mändl S.: *Comparison of ZrN and TiN formed by plasma based ion implantation & deposition*, Surface & Coatings Technology 202 (2008), pp. 2310–2313.

[HER81] Hertz H.: *Über die Berührung fester elastischer Körper*, Journal für die reine und angewandte Mathematik 92 (1881), pp. 156-171.

[HOL01] Hollstein F., Kitta D., Louda P., Pacal F., Meinhardt J.: *Investigation of low-reflective ZrCN PVD-arc coatings for application on medical tools for minimally invasive surgery*, Surface and Coatings Technology 142-144 (2001), pp. 1063-1068.

[HUA05] Huang J.H., Yang H.-C., Guo X.-J., Yu G.-P.: *Effect of film thickness on the structure and properties of nanocrystalline ZrN thin films produced by ion plating*, Surface & Coatings Technology 195 (2005), pp. 204– 213.

[HUA07] Huang J.-H., Chang K.-H., Yu G.-P., *Synthesis and characterization of nanocrystalline* ZrN_xO_y *thin films on Si by ion plating*, Surface & Coatings Technology 201 (2007), pp. 6404–6413.

[HUD06] Hudson L.K., Eastoe J., Dowding P.J.: *Nanotechnology in action: Overbased nanodetergents as lubricant oil additives*, Advances in Colloid and Interface Science 123–126 (2006), pp. 425–431.

[IKE88] Ikeda S., Yagi T., Ishizawa N., Mizutani N., Kato M., *A New Face-Centered Cubic Phase in the ZrO_2-ZrN System*, Journal of Solid State Chemistry 73 - 1, (1988), pp. 52-56.

[JOH87] Johnson K.L.: *Contact Mechanics*, p. 306-311, Cambridge Univ. Press (1987).

[JUZ64] Juza R., Gabel A., Rabenau H., Klose W.: *Über ein blaues Zirkonnitrid*, Zeitschrift für Anorganische und Allgemeine Chemie 329 (1964), pp. 136.

[KAO07] Kao W.H.: *Optimized a-C coatings by doping with zirconium for tribological properties and machining performance*, Diamond & Related Materials 16 (2007), pp. 1896–1904.

[KAO08] Kao W.H.: *High-speed drilling performance of coated microdrills with Zr-C:H:Nx% coatings*, Wear 267 (2008), pp. 1068-1074.

[KAT86] Katsov K. B., Zhitomirskii V. N., Khrunik R. A.: *Contact Fatigue Of High-Speed Steel With Wear-Resistant Nitride Coatings In A Corrosive Medium*, Fiziko-Khimicheskaya Mekhanika Materialov 22-5 (1986), pp. 100-101.

[KIE70] Kieffer R., Nowotny H., Ettmayer P., Freudhofmeier M.: *Über die Beständigkeit von Übergangsmetallcarbiden gegen Stickstoff bis zu 300 at*, Monatshefte für Chemie 101 – 1 (1970), pp. 65-82.

[KIE72] Kieffer R., Nowotny H., Ettmayer P., Dufek G.: Miscibility of the Nitrides and Carbides of Transition Metals, Metall Technik 26-27 (1972), pp. 701-708.

[KIM98] Kim T. H., Olver A. V.: *Stress history in rolling–sliding contact of rough surfaces*, Tribology International 31 -12 (1998), pp. 727–736.

[KIN94] King, R.B.: *Encyclopedia of inorganic chemistry*, John Wiley & Sons Ltd., New York (1994).

[KLE04] Kleemann J., Woydt M.: *Dry friction and wear rates as under liquid lubrication of ceramic/carbon couples up to 450°C*, Industrial Lubrication and Tribology 56-1 (2004), pp. 38–51.

[KLE08] Kleemola J., Lehtovaara A.: *Evaluation of gear contact along the line of action using a twin-disc test device*, Proceedings of the 3th Nordic Symposium on Tribology, NORDTRIB2008 (2008).

[KRA03] Krantz T. L., Cooper C. V., Townsend D. P., Hansen B. D.: *Increased surface fatigue lives of spur gears by application of a coating*, NASA/TM—2003-212463, Proceedings of ASME 2003 Design Engineering Technical Conference and Computers and Information in Engineering Conference, Chicago, Illinois USA, September 2-6, 2003.

[KRÖ58] Kröner E.: *Berechnung der elastischen Konstanten des Vielkristalls aus den Konstanten des Einkristalls*, Zeitschrift für Physik 151 - 4 (1958), pp. 504–518.

[KUM06] Kumagai M., Jinbo Y., Yakabe F.: *Improvement of Rolling Contact Fatigue by DLC Coating*, Journal of The Surface Finishing Society of Japan 57-6 (2006), pp. 428-433.

[KUM07] Kumagai M., Jimbo Y. and Yakabe F.: *Surface strengthening method*, US 2007/0009662.

[KUM08] Y. Fumiya, Jinbo Y., Kumagai M., Horiuchi T., Kuwahara H., Ochia S.: *Excellent durability of DLC film on carburized steel (JISSCr420) under a stress of 3.0 GPa*, Journal of Physics: Conference Series 100 (2008) 082049.

[LAI09] Lai J., Ionannides S., Wang J.: *Lubricant hydraulic Effect on surface-breaking cracks in rolling sliding contact*, World Tribology Congress 2009, Kyto, Japan September 6-11, 2009, p. 384.

[LAM05] Lamni R*.: Propriétés physiques et chimiques des couches minces de ZrN, Zr-Al-N et Zr-Cr-N déposées par pulvérisation magnétron réactive*, PhD thesis EPFL N° 3238 (2005).

[LEM09] LeMaster R., Boggs B., Bunn J., Hubbard C., Watkins T.: *Grinding Induced Changes in Residual Stresses of Carburized Gears*, Geartechnology 26 – 2 (2009), p. 42-49.

[LER96] Lerch M., Wrba J.: *Formation of rock salt-type Zr(N,O,C) phases by carbothermal nitridation of zirconia*, Journal of Materials Science Letters 15 - 5 (1996), pp. 378-380.

[LER96] Lerch M., Fuglein E., Wrba J.: Synthesis, crystal structure, and high temperature behavior of Zr_3N_4, Zeitschrift für Anorganische und Allgemeine Chemie 622 (1996), pp. 367-372.

[LER97] Lerch M.: *Neue Anionendefizit-Materialien auf der Basis von ZrO_2: Synthese, Charakterisierung und Eigenschaften von ternären und quaternären Nitridoxiden des Zirconiums*, Habilitationsschrift, Würzburg (1997).

[LEY04] Leyland A., Matthews A.: *Design criteria for wear-resistant nanostructured and glassy-metal coatings*, Surface and Coatings Technology 177 –178 (2004), pp. 317–324.

[LID97] Lide David R.: *Handbook of chemistry and physics – 78th edition*, CRC Press, Boca Raton (1997).

[LIN96] Lindan, P. J. D., Harrison N. M., Holender J. M., Gillan M. J.: *First-principles molecular dynamics simulation of water dissociation on TiO_2*, Chemical Physics Letters 261 (1996), pp. 246-252.

[LIU07] Liu S.J., Hua D.Y.: *Wear Behaviour of W-DLC Coating Under Reciprocating Sliding Motion*, ASTM D02 Symposium on Wear and Friction Test Methods for Coatings and Surface Treatments, 21. June 2007, Miami Beach (FL), USA

[LIU09] Liu G., Li J., Chen K., Zhou H., Pereira C., Ferreira J., *Polycrystalline $ZrN_{1-x}C_x$ Layers with (111) Preferred Orientation Prepared by the Carbothermal Nitridation of ZrO_2 Ceramics*, Crystal Growth Design, 2009, 9 (1), pp. 562-568

[MAL06] Malmkvist A.: *Method development for slip measurement on valve train*, Volvo D12. PhD thesis, Chalmers University of Technology (2006).

[MAN08] Manier C.-A., Spaltmann D., Woydt M., in *Tribology of Diamond-like Carbon Films: Fundamentals and Applications*, ed. by C. Donnet and A. Erdemir, Springer, New-York (2008).

[MAR01] Martin, N.; Banakh, O.; Santo, A.M.E.; Springer, S.; Sanjinés, R.; Takadoum, J.; Lévy, F.: *Correlation between processing and properties of TiO_xN_y thin films sputter deposited by the reactive gas pulsing technique*, Applied Surface Science 185 1-2 (2001), pp. 123-133.

[MAR08] Martin J. M., Ohmae N.: *Nanolubricants*, Tribology Series, Wiley (2008).

[MARt08] Martins R., Amaro R. and Seabra J.: *Influence of low friction coatings on the scuffing load capacity and efficiency of gears*, Tribology International, 41 - 4 (2008), pp. 234-243.

[MAS86] Massalski T. S., Murray J. L., Bennett L., Baker H.: *Binary Alloy Phase Diagrams*, American Society of Metals (Metals Park, Ohio 1986).

[MAS91] Massalski T.B. (ed.), *Binary Alloys Phase Diagrams*, ASM International, Metals Park OH (1991).

[MAT04] Mathur S., Altmayer J., Shen H.: *Nanostructured* ZrO_2 *and Zr-C-N Coatings from Chemical Vapor Deposition of Metal-Organic Precursors*, Zeitschrift für Anorganische und Allgemeine Chemie 630 (2004), pp. 2042 2048

[MAT99] Matzke Hj., Rondinella V.V., in: D.L. Beke (Ed.), *Diffusion in Carbides, Nitrides, Hydrides and Borides*, Landolt-Bfrnstein Numerical Data and Functional Relationship in Science and Technology, vol. 33, Springer, Berlin, (1999).

[MAY01] Mayrhofer P.H., Tischler G., Mitterer C.: *Microstructure and mechanical_thermal properties of Cr-N coatings deposited by reactive unbalanced magnetron sputtering*, Surface and Coatings Technology 142-144 (2001), pp. 78-84.

[MOR02] Morstein M.,. Willmott P.R, Spillmann H., Döbeli M.: *From nitride to carbide: control of zirconium-based hard materials film growth and their characterization*, Applied Physics A 75 (2002), pp. 647–654.

[MOU06] Moura C., Carvalho P., Vaz F., Cunha L., Alves E.: *Raman spectra and structural analysis in ZrOxNy thin films*, Thin Solid Films 515 (2006), pp. 1132–1137

[NAJ06] Najmana M., Kasraia M., Bancrofta G. M., Davidson R., *Combination of ashless antiwear additives with metallic detergents: interactions with neutral and overbased calcium sulfonates*, Tribology International 39 (2006), pp. 342–355.

[NEL98] Nelias D., Dumont M.-L., Champiot F., Girondin D., Lormand G., Vincent A., Fougères R and Flamand L.: *Influences des inclusions, de l'état de surface et des conditions de fonctionnement sur la fatigue des aciers M50 et 100Cr6 dans les contacts ponctuels lubrifiés*, 17èmes journée de Printemps, Fatigue de contact, Société Française de Métallurgie et de Matériaux, Senlis, 27-28 Mai 1998, p. 10(1)-10(12).

[NEL99] Nelias D.: *Contribution à l'étude des roulements. Modélisation globale des roulements et avaries superficielles dans les contact EHD pour des surfaces réelles ou indentées*, Dossier d'habilitation à diriger des recherches, INSA-Lyon/Université Claude Bernard - Lyon I, HDR 99 008 (1999).

[NN22] N.N., *Abnützungsmaschine für Metalle*, Zeitschrift des VDI 66 – 15 (1922), pp. 377-378.

[OHR92] Ohring M.: *The Materials Science of Thin Films*, Academic Press, San Diego, 1992.

[OIL05] Oila A., Bull S.J.: *Assessment of the factors influencing micropitting in rolling/sliding contacts*, Wear 258 (2005), pp. 1510–1524.

[PIC99] Pichon L., Girardeau T., Straboni A., Lignou F., Guérin P., Perrière J.: *Zirconium nitrides deposited by dual ion beam sputtering: physical properties and growth modelling*, Applied Surface Science 150 (1999), pp. 115–124.

[POL97] Po|onsky I.A., Chang T.P., Keer L.M., Sproul W.D.: *An analysis of the effect of hard coatings on near-surface rolling contact fatigue initiation induced by surface roughness,* Wear 208 (1997), pp. 204-219.

[POL98] Polonsky I.A., Chang T.P., Keer L.M., Sproul W.D.: *A study of rolling contact fatigue of bearing steel coated with physical vapor deposition TiN films: coating response to cyclic contact stress and physical mechanisms underlying coating effect on the fatigue life*, Wear 215 (1998), pp. 191–204.

[POU66] Pourbaix M.: *Atlas of Electrochemical Equilibria in Aqueous Solutions*, Pergamon Press, London (1966).

[PRE98] Predel B.: *Phase equilibra, crystallographic and thermodynamic data of binary alloys*, Bd. IV/5. Springer Verlag, Berlin (1998).

[PRIC98] Prices of 1998, *Metal Prices in the United States through 1998*, http://minerals.usgs.gov/minerals/pubs/metal_prices/US Geological Survey.

[ROS68] Rosa C.J., Hagel W.C.: *A Film-Thickness Determination of Nitrogen Diffusion in Zirconium Nitride*, Journal of the Electrochemical Society 115 - 5 (1968) pp. 467-470.

[RUS07] Russias J., Cardinal S., Esnouf C., Fantozzi G., Bienvenu K.: *Hot pressed titanium nitride obtained from SHS starting powders: Influence of a pre-sintering heat-treatment of the starting powders on the densification process*, Journal of the European Ceramic Society 27 - 1 (2007), pp. 327-335.

[SAB74] Sablev L.P., et al. United States Patent 3,793,179 February 19, 1974 Apparatus For Metal Evaporation Coating.

[SAN00] Sanders D.M., Anders A.: *Review of cathodic arc deposition technology at the start of the millenium*, Surface and Coatings Technology 133 - 134 (2000), pp. 78-90.

[SAR06] Sarioglu C.: *The effect of anisotropy on residual stress values and modification of Serruys approach to residual stress calculations for coatings such as TiN, ZrN and HfN*, Surface & Coatings Technology 201 (2006), pp. 707–717.

[SCH06] Schmidt R., Klingenberg G., Woydt M.: *New lubrication concepts for environmental friendly machines*, BAM Research Report Nr. 277, Bundesanstalt für Materialforschung und -prüfung, Wirtschaftsverlag NW, Verlag für neue Wissenschaft GmbH, (2006).

[SCH85] Schwarz K., Williams A.R., Cuomo J.J., Harper J. H. E., Hentzell H.T.G.: *Zirconium nitride – a new material for Josephson junctions*, Physical Review B 32 (12) (1985), pp. 8312-8316.

[SCO78] Scott D.: *The assessment of wear-resistant coatings for arduous conditions of rolling contact*, Wear 48 – 2 (1978), pp. 283-290.

[SEI72] Seitzinger K., Richter M.: *Grenzen und Möglichkeiten der FZG-Zahnrad-Verspannungs-Prüfmaschine, insbesondere zur Prüfung von Hypoidgetriebeölen - Teil 2: Variationen des FZG-A/8,3/90-Tests und ihre Auswirkungen auf die Schadenskraftstufe eines Getriebeöles*, Schmiertechnick und Tribologie 19-1 (1972), pp.22-29, pp. 58-60, pp. 128-130, pp. 145-148

[SHI00] Shi S.: *The way to zirconia*, Materials Interaction 13 -11 (2000), pp. 66-69.

[SHI03] Shigley J., Mischke C. R., Budynas R. G.: *Mechanical Engineering Design 7th edition*, McGraw-Hill Science, (2003).

[SMI00] Graham C. Smith: *Surface analytical science and automotive lubrication*, Journal of Physics D: Applied Physics 33 (2000) R187–R197

[SNA71] Snaper, A. A., US Patent 3,625,848 (1971), 3,836,451 (1974)

[SPA04] Spaltmann D., Löhr M., Binkowski S., Woydt M.: *Einfluss der Topographie von DLC-Schichten auf deren Verhalten unter geschmierter Wälzbeanspruchung*, Tribologie und Schmierungstechnik 51 - 6 (2004), pp. 18-26.

[SPA08] Spaltmann D., Manier C.-A., Theiler G., Proß E., Ziegele H., Kursawe S., Woydt M.: *Überrollbeständige Dünnschichten unter geschmierter Wälzreibung bis 3.500 MPa*, Tribologie und Schmierungstechnik 55 - 4 (2008), pp. 22-27.

[STE02] Stewart S., Ahmed R.: *Rolling contact fatigue of surface coatings—a review*, Wear 253 (2002), pp. 1132–1144.

[STU09] Stueber M., Holleck H., Leiste H., Seemann K., Ulrich S., Ziebert C.: *Concepts for the design of advanced nanoscale PVD multilayer protective thin films*, Journal of Alloys and Compounds 483 (2009), pp. 321–333.

[THO04] Thoquenne G.: *Prévision des durées de vie en fatigue des roulements*, PhD thesis, Ecole Polythechnique, 2004.

[THO86] Thornton J.A.: *The microstructure of sputter-deposited coatings*, Journal of Vacuum Science & Technology A: Vacuum, Surfaces, and Films 4 - 6 (1986), pp. 3059 -3065.

[THO93] Thom R., Moore L., Sproul W. D., Chang T. P.: *Rolling contact fatigue tests of reactively sputtered nitride coatings of Ti, Zr, Hf, Cr, Mo, Ti-Al, Ti-Zr and Ti-Al-V on 440C stainless steel substrates*, Surface and Coatings Technology 62 (1993), pp. 423-427.

[TRI94] Tricot R.: Zirconium et hafnium, Technique de l'ingénieur, Traité Matériaux Métalliques M2360 (1994).

[VAZ04] Vaz F., Carvalho P., Cunha L., Rebouta L., Moura C., Alves E., Ramos A.R., Cavaleiro A., Goudeau Ph., Rivière J.P.: *Property change in* ZrN_xO_y *thin films: effect of the oxygen fraction and bias voltage*, Thin Solid Films 469–470 (2004), pp. 11–17.

[VDI05] VDI-guideline 2840, *Carbon films, basic knowledge, film types and properties*, ICS 25.220.99, Beuth Verlag GmbH, 10772 Berlin (2005).

[VEP03] Veprek S., Mukherjee S., Karvankova P., Männling H.-D., He J.L., Moto K., Prochazka J., Argon A.S.: *Hertzian analysis of the self-consistency and reliability of the indentation hardness measurements on superhard nanocomposite coatings*, Thin Solid Films 436 (2003), pp. 220–231.

[VIL98] Ville F., Pollution solide des lubrifiants, indentation et fatigue des surfaces, PhD Thesis, INSA-Lyon, 1998.

[VIZ08] Vizcaíno P., Banchik A.D., Abriata J.P.: *Synchrotron X-ray diffraction evidences of the amorphization/dissolution of the second phase particles (SPPs) in neutron irradiated Zircaloy-4*, Materials Letters 62 (2008), pp. 491–493.

[WAN06] Wang I.Y., He J.L., Chen K.C., Davison A.: *Nano-multilayer Ti–Zr–N coating by a central configured multi-arc coating process*, Surface & Coatings Technology 201 (2006), pp. 4174–4179.

[WEI92] Wei R., Wilbur P.J., Kustas F.M.: *A rolling contact fatigue study of hard carbon coated M-50 steel*, STLE/ASME Tribology Conference Saint Louis MO, Journal of tribology 114 - 2 (1992), pp. 298–302.

[WER98] Wern H., Johannes R., Walz H.: *Dependence of the X-Ray Elastic Constants on the Diffraction Plane*, Physica status solidi. B. 206 (1998), pp. 545 – 557.

[WIN09] Winkelmann L., El-Saeed O., Bell M.: *The Effect of Superfinishing on Gear Micropitting*, Geartechnology 26 - 2 (2009), pp. 60-65.

[WOH00] Wöhle J., Pfohl C., Rie K.-T., Gebauer-Teichmann A., Kim S.K., *Deposition of TiCN and ZrCN layers on light metals by PACVD method using radio frequency and pulsed-DC Plasma*, Surface and Coatings Technology 131, (2000), pp. 127-130.

[YAO05] Yao S.H., Su Y.L., Kao W.H., Cheng K.W.: *Wear behavior of DC unbalanced magnetron sputter deposited ZrCN films*, Materials Letters 59 (2005), pp. 3230 – 3233.

[YAS99] Yashar P. C., Sproul W. D.: *Nanometer scale multilayered hard coatings*, Vacuum 55 (1999), pp. 179-190.

[YON05] Yonekra D., Chittenden R.J., Dearnley P. A.: *Wear mechanisms of steel roller bearings protected by thin, hard and low friction coatings*, Wear 259 (2005), 779-788.

[ZER03] Zerr, A., Miehe, G., Riedel, R.: *Synthesis of cubic zirconium and hafnium nitride having Th3P4 structure*, Nature Materials 2 (2003), 185–189.

[ZHI06] Zhiguo Z., Tianwei L., Jun X., Xinlu D., Chuang D.: *N-rich Zr–N films deposited by unbalanced magnetron sputtering enhanced with a highly reactive MW-ECR plasma*, Surface & Coatings Technology 200 (2006) 4918 – 4922.

[ZHA04] Zhang Q., Seki M., Ohue Y., Yoshida A., Murakami M., Sato M., Konishi M.: *Study on surface durability of Powder-Forged Roller with case Hardening*, JSME International Journal, Series C, vol. 47, No.3, (2004).

[ZOU06] Zoulalian V, Monge S, Zürcher S, Textor M, Robin JJ, Tosatti S.: *Functionalization of titanium oxide surfaces by means of poly(alkyl-phosphonates)*, J. Phys. Chem. B, 110 (51), 2006, pp. 25603–25605.

List of tables and figures

Tables

Figures